AD-A095 919 HENRY KRUMB SCHOOL OF MINES NEW YORK ALDRIDGE LAB OF--ETC F/G 8/11
ELASTIC AND VISCOELASTIC WAVE SCATTERING AND DIFFRACTION.(U)
JAN 81 J T KUO, Y TENG, K CHEN, C E SHEPHERD F49620-77-C-0130

UNCLASSIFIED AFOSR-TR-81-0107 NL

1 of 5

AD A
095919

AFOSR-TR- 81-0107

LEVEL

ELASTIC AND VISCOELASTIC WAVE SCATTERING AND DIFFRACTION

John T. Kuo

Yu-chiung Teng, Kun-hua Chen, and Charles E. Shepherd

Aldridge Laboratory of Applied Geophysics
Henry Krumb School of Mines
Columbia University in the City of New York
New York, New York 10027

Contract No. F49620-77-0130

FINAL REPORT

Period Covered: September 1, 1977 through August 30, 1980

This document has been approved for public release and sale; its distribution is unlimited.

Contract Monitor: William Best
Directorate of Physics

Prepared for

AIR FORCE OFFICE OF SCIENTIFIC RESEARCH
BOLLING AIR FORCE BASE
WASHINGTON, D.C. 20332

January 1981

UNCLASSIFIED

SECURITY CLASSIFICATION OF THIS PAGE (When Data Entered)

REPORT DOCUMENTATION PAGE		READ INSTRUCTIONS BEFORE COMPLETING FORM
1. REPORT NUMBER AFOSR-TR- 81-0107	2. GOVT ACCESSION NO. AD-A095 919	3. RECIPIENT'S CATALOG NUMBER
4. TITLE (and Subtitle) ELASTIC AND VISCOELASTIC WAVE SCATTERING AND DIFFRACTION		5. TYPE OF REPORT & PERIOD COVERED 1 Sep 77 - 30 Aug 80 Final
		6. PERFORMING ORG. REPORT NUMBER
7. AUTHOR(s) John T Kuo		8. CONTRACT OR GRANT NUMBER(s) F49620-77-C-0130
9. PERFORMING ORGANIZATION NAME AND ADDRESS Henry Krumb School of Mines Columbia University New York, NY 10027		10. PROGRAM ELEMENT, PROJECT, TASK AREA & WORK UNIT NUMBERS 61102F 2309/A1
11. CONTROLLING OFFICE NAME AND ADDRESS AFOSR/NP Bolling AFB Wash DC 20332		12. REPORT DATE Jan 1981
		13. NUMBER OF PAGES 211
14. MONITORING AGENCY NAME & ADDRESS(if different from Controlling Office)		15. SECURITY CLASS. (of this report) unclassified
		15a. DECLASSIFICATION DOWNGRADING SCHEDULE

16. DISTRIBUTION STATEMENT (of this Report)

Approved for public release; distribution unlimited.

17. DISTRIBUTION STATEMENT (of the abstract entered in Block 20, if different from Report)

18. SUPPLEMENTARY NOTES

19. KEY WORDS (Continue on reverse side if necessary and identify by block number)

20. ABSTRACT (Continue on reverse side if necessary and identify by block number)

The main objective of this research was to study the problem of two- and three dimensional wave scattering and diffraction in elastodynamics and viscoelastodynamics. Presently available analytical techniques for solving wave propagation problems are useful only for simple cases. In practice, the presence of inhomogeneities and irregular boundary conditions defies analytical solutions. One of the best numberical techniques suitable for solving wave propagation in a complex geological medium, such as the problem of the ground response to seismic

DD FORM 1473

UNCLASSIFIED

disturbances in alluvial valleys, is the method of combining the finite element method (FEM) in space and the finite differences method (FDM) in time. The advantages of using the finite element method in space are: (1) allowing for almost any type of static, dynamic, and thermal loading to be applied. (2) relatively easy to apply boundary conditions. (3)its flexibility in modeling irregular geology and topography. (4) its distribution of errors, which are averaged over the elements throughout the domain in question.

ELASTIC AND VISCOELASTIC WAVE SCATTERING AND DIFFRACTION

John T. Kuo

Yu-chiung Teng, Kun-hua Chen, Charles E. Shepherd

Aldridge Laboratory of Applied Geophysics
Henry Krumb School of Mines
Columbia University in the City of New York
New York, New York 10027

Contract No. F49620-77-C-0130

FINAL REP[redacted]RT

Period Covered: 1 Sep[redacted]977 [redacted] Aug[redacted]80

This document has been approved for public release and sale; its distribution is unlimited.

Contract Monitor: William Best
Directorate of Physics

Prepared for

AIR FORCE OFFICE OF SCIENTIFIC RESEARCH
BOLLING AIR FORCE BASE
WASHINGTON, D.C. 20332

Jan[redacted]81

TABLE OF CONTENTS

PREFACE

Contract F 49620-77-0130 of the Air Force Office of Scientific Research, beginning September 1, 1977, was specifically directed toward solving problems of elastic and viscoelastic wave scattering and diffraction with applications to the silo and its related problems.

The Contract has been successfully executed at the Aldridge Laboratory of Applied Geophysics. This Final Report reflects the accomplishments of the Contract, including doctoral dissertations to be published and unpublished papers.

I am grateful to Mr. William Best of the Air Force Office of Scientific Research for monitoring the contract, and Drs. Ker Thomson, Gerry Cabaniss, and Frank Crowley for their interest in the project. I wish to acknowledge Ms. Linda Ripps, who typed this report most patiently.

John T. Kuo

January 5, 1981

Columbia University

New York, New York 10027

GENERAL INTRODUCTION

Under the Air Force Contract, AF-49620-77-C-0130, "Elastic and Viscoelastic Wave Scattering and Diffractions," the main objective of the research was to study the problem of two- and three-dimensional wave scattering and diffraction in elastodynamics and viscoelastodynamics. Presently available analytical techniques for solving wave propagation problems are useful only for simple cases. In practice, the presence of inhomogeneities and irregular boundary conditions defies analytical solutions. One of the best numerical techniques suitable for solving wave propagation in a complex geological medium, such as the problem of the ground response to seismic disturbances in alluvial valleys, is the method of combining the finite element method (FEM) in space and the finite differences method (FDM) in time. The advantages of using the finite element method in space are:

(1) allowing for almost any type of static, dynamic, and thermal loading to be applied.

(2) relatively easy to apply boundary conditions.

(3) its flexibility in modeling irregular geology and topography.

(4) its distribution of errors, which are averaged over the elements throughout the domain in question.

The advantage of using the explicit finite differences method in time integration is that solutions so obtained are generally conditionally stable, and fast convergent to yield solutions which are only simple products and vector additions.

However, the physical insight to the scattering and diffraction phenomena only can be gained through analytical approaches or physical modeling studies; the interpretation of the numerical solutions must base on the fundamental understanding of the scattering and diffraction phenomena. Therefore, our approaches to solving the complex scattering and diffraction problems have been oriented toward:

(1) to solve practical problems by numerical methods.

(2) to gain insight to the numerical solutions to practical problems by analytical and physical modeling studies.

As for the numerical methods, we emphasize the research on the finite element formulation and computer programming. We have completed the finite element algorithm for transient elastic and viscoelastic wave scattering and diffraction problems in two and three dimensions and, as a by-product, the finite element elastostatic algorithm for static and quasistatic loading problems.

So far as the effect of damping on the elastic wave propogation is concerned, the computer codes for the two- and three-dimensional Rayleigh type of damping have been written and successfully tested. However, these original computer codes have followed the conventional "block-by-block" format that require an enormously large in-core storage and a large amount of computing time for solving geologically practical problems.

Therefore, we have also been working on the areas of:

(1) overcome the practical difficulties of using large in-core storage.

(2) sparse matrix without calculating zero-matrix elements to save the computing time.

(3) the basic problem of convergence and stability to obtain a good solution without taking more computing time than actually required.

(4) the undesirable reflections from the artificial boundaries.

The finite element algorithm for elastic waves has been successfully applied to solve the problem of the transient seismic response of an elastic whole-space, an elastic half-space, and a layered elastic half-space due to a finite cylindrical cavity source.

Only by a considerable reduction of in-core storage and saving of computing time would it be possible to perform an extensive parameter-study of more realistic geological problems as shown in Figure 1.

In the area of analytical studies, we have been exploring one of the most attractive analytical methods, i.e. the high-order perturbation method. The existence of two different types of elastic waves, viz. compressional and shear waves in elastodynamic boundary value problems, has frustrated many investigators to solve more realistic problems. In the perturbation method, we are able to replace the two different wave numbers for P-wave and S-wave by their root-mean-square (RMS) values so that there will be only one single wave number involved. The previous RMS perturbation solutions developed by Pao and Thau (1967) are only up to the order of two. We have now extended the method to the higher-order solutions, through the general recurrence formulas. Moreover, we have applied the newly developed perturbation method to solve one of the long-standing elastodynamic wedge problems and obtained very encouraging results. In order to

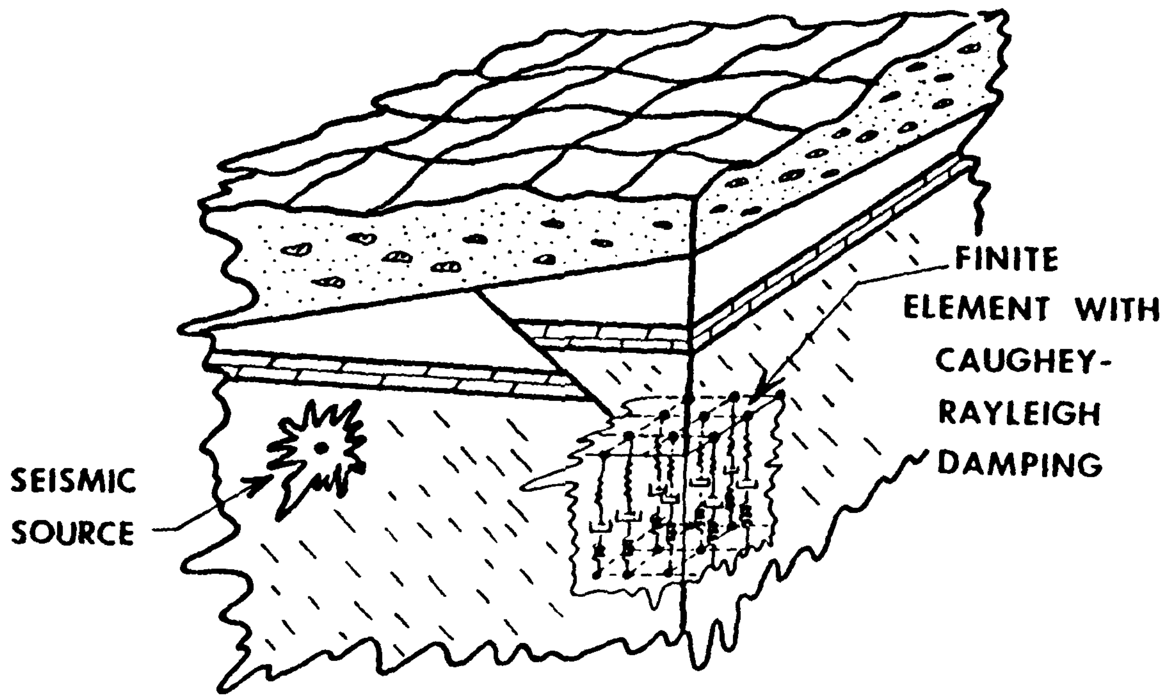

FIGURE 1. 3-D FINITE ELEMENT SEISMIC MODELING MORE REALISTIC GEOLOGICAL STRUCTURES

gain further insight to wave scattering and diffraction problems, three-dimensional physical model experiments have been performed at the Aldridge Laboratory of Applied Geophysics to study the acoustic-elastic wave scattering and diffraction by a vertical elastic cylinder immersed in a fluid due to a transient acoustic point source.

Physical insight into these problems, both analytically and experimentally, has been invaluable in interpretation of the finite element results.

I. FINITE ELEMENT FORMULATION AND COMPUTER PROGRAMS FOR ELASTIC AND VISCOELASTIC WAVE SCATTERING AND DIFFRACTION PROBLEMS

ABSTRACT

The three-dimensional finite element for both elastic and viscoelastic wave scattering and diffraction, based on the principle of virtual work,has now been completed for solving transient elasto- and viscoelasto-dynamic problems, as well as elasto- and viscoelasto-static problems. Computer programs for the finite element formulation are developed and tested.

The conventional "block-by-block" format used in the computer programs has been improved in order to save the in-core storage and computer time. Stability condition and convergence criteria of the finite element in space and the finite differences in time have been examined. The computer programs developed under the Contract are now ready and have been submitted to AFGL for their use.

FINITE ELEMENT FORMULATION

Based on the principle of virtual work, we have now completed the three-dimensional finite element formulation for viscoelastic wave scattering and diffraction to complement that for elastic wave scattering and diffraction due to a transient seismic disturbance, as reported in the Final Report of an earlier contract AFOSR-76-2968, "Numerical and Analytical Solutions to Elastodynamic Problems". The general procedure for using the finite element method in solving elastodynamic problems in continuum mechanics includes idealization of the problem, space discretization of finite elements, and formulation of the set of simultaneous equations to be solved. For viscoelastic waves, the equations of motion for elastodynamics must include a term to account for energy dissipation. Usually this mechanism takes the form of viscous damping, which is linearly proportional to velocity. Hence, the equations of motion for viscoelastodynamics are:

$$[m]\{\ddot{u}\} + [c]\{\dot{u}\} + [k]\{u\} = \{f(t)\} \tag{1}$$

where $\{u\}$, $\{\dot{u}\}$, $\{\ddot{u}\}$ are the displacement, velocity and acceleration vectors of the finite element assemblage, and

$[m]$ = the assembled mass matrix.

$[c]$ = the viscous damping matrix.

$[k]$ = the assembled structural stiffness matrix.

$\{f(t)\}$ = the external time-dependent vector load vector.

It is obvious that equation (1) reduces to the equations of motion for elastodynamics as $[C] = 0$. Equation (1) states that, in principle, static equilibrium at time t, which includes the effects of inertia force, elastic force and damping force, is reached. While in static analysis, one simply neglects the inertia and damping effects in equation (1).

The free vibration equilibrium equation for the undamped system is well-known as follows:

(2) $$[m]\{\ddot{u}\} + [k]\{u\} = 0$$

Assume that

(3) $$\{u\} = \{\phi\}\,T(t)$$

where

(4) $$T(t) = A \sin \omega t + B \cos \omega t$$

$\{\phi\}$ = time dependent shape vector, and

A and B = arbitrary constants. Differentiating equation (3) twice with respect to time t, we have

(5) $$\{\ddot{u}\} = \{\phi\}\,\ddot{T}(t) = -\,\omega^2 \{\phi\}\,T(t)$$

Equation (2) yields

$$(6) \qquad ([k] - \omega^2 [m]) \{\phi\} = 0$$

In order to have a non-trivial solution to this equation, the following condition must be satisfied

$$(7) \qquad \left| [k] - \omega^2 [m] \right| = p(\omega^2) = 0$$

This leads to the classical eigenvalue problem. The solution to this equation is $\omega=\omega_n$, $n=1,2,3......$, N in which N is the number of the modes. ω_n are the natural angular frequencies of the system. The shape vector function $\{\phi\}$ can be obtained by solving equation (6) for each value of ω, giving

$$(8) \qquad [k] \{\phi_n\} = \omega_n^2 [m] \{\phi_n\}$$

for the n-th mode of vibration.

Superposition of the response for all modes gives

$$(9) \qquad \{u\} = \sum_{n=1}^{N} \{\phi_n\} \{T_n(t)\} = [\Phi] \{T(t)\}$$

where the n-th column in $[\Phi]$ contains the shape vector $\{\phi_n\}$

Substituting equation (9) into (1), we have

$$(10) \qquad [m] [\Phi] \{\ddot{T}\} + [c] [\Phi] \{\dot{T}\} + [k] [\Phi] \{T\} = \{f(t)\}$$

Premultiplying equation (10) by $[\Phi]^T$, we have

$$(11) \qquad [\Phi]^T [m] [\Phi] \{\ddot{T}\} + [\Phi]^T [c] [\Phi] \{\dot{T}\} + [\Phi]^T [k] [\Phi] = [\Phi]^T \{f(t)\} = \{F(t)\}$$

The Orthogonality conditions are:

$$(12) \qquad \left.\begin{array}{l} \{\phi_m\}^T [m] \{\phi_n\} = 0 \\ \{\phi_m\}^T [k] \{\phi_n\} = 0 \end{array}\right. \qquad \text{if } m \neq n$$

Caughey (1960) pointed out that:

a) Equation (11) will be decoupled if, and only if, $[\Phi]^T[c] [\Phi]$ is diagonal,

b) if $[\Phi]^T[c][\Phi]$ is diagonal, the damped system will have normal modes, which are identical with those for the undamped system, and

c) if a damping matrix $[C]=[\Phi]^T[c][\Phi]$ has the form

$$(13) \qquad [C] = [M] \sum_{b=0}^{N-1} a_b \left([M]^{-1} [K]\right)^b$$

the damped system will have classical normal modes.

Now, if the damping matrix also satisfies

$$(14) \qquad \{\phi_m\}^T [c] \{\phi_n\} = 0 \qquad \text{for } m \neq n$$

and equation (11) becomes

$$(15) \qquad M_n \ddot{T}_n + C_n \dot{T}_n + K_n T_n = q_n(t)$$

where

(16)
$$M_n = \{\phi_n\}^T [m]\{\phi_n\}$$
$$C_n = \{\phi_n\}^T [c]\{\phi_n\}$$
$$K_n = \{\phi_n\}^T [k]\{\phi_n\}$$

Since M_n, C_n, K_n are scalars, equation (1) is decoupled to N linear equations. Each of these equations represents the equation of motion of a single-degree-of-freedom system. The damping constant can be so chosen that

(17)
$$C_n = 2\ \lambda_n\ \omega_n\ m_n$$

(18)
$$\omega_n = \surd(K_n/M_n)$$

where λ_n= the damping ratio for the n-th mode.

ω_n= the natural angular frequency for the n-th mode. Then, the damping ratio in each mode, λ_n can be related to the natural angular frequency of that mode by

(19)
$$\lambda_n = \frac{1}{2} \sum_{b=0}^{N-1} a_b\ \omega_n^{2b-1}$$

In equation (13), if N=2,

(20)
$$[C] = a_o\ [M] + a_1\ [K]$$

This form was first proposed by Rayleigh. Equation (19) becomes

$$\lambda_n = \frac{1}{2}\left(\frac{a_o}{\omega_n} + a_1\,\omega_n\right) \tag{21}$$

Therefore, Rayleigh damping can be considered as a special case of Caughey damping. The constants a_0 and a_1 can be determined by any two arbitrary conditions. If these two conditions are so chosen that the damping ratios are specified for the first two modes, then

$$a_o = \frac{2(\omega_2\lambda_1 - \omega_1\lambda_2)}{\left(\omega_2/\omega_1 - \omega_1/\omega_2\right)} \tag{22}$$

$$a_1 = \frac{2\left(\lambda_2/\omega_1 - \lambda_1/\omega_2\right)}{\left(\omega_2/\omega_1 - \lambda_1/\omega_2\right)} \tag{23}$$

The procedure described above involves the calculation of the frequencies for the first two modes.

Another procedure for determining the values of a_0 and a_1 is to specify the damping ratio at the frequency for which the damping is a minimum, usually the fundamental frequency of the system. Then we have

$$a_o = \omega_1\,\lambda_1 \tag{24}$$

$$a_1 = \lambda_1/\omega_1 \tag{25}$$

Solving the eigenvalue of the equation

$$(7) \qquad \left| [k] - \omega^2 [m] \right| = p(\omega^2) = 0$$

is equvalent to calculating the roots of the polynomial $p(\omega^2)$, which has the order equal to the order of [k] and [m] that are usually a very large number. Therefore, an iteration solution method has to be used. The time integration scheme with damping effect then is

$$(26) \qquad \{u(t+\Delta t)\} = \{u(t)\} + \{\dot{u}(t)\}\Delta t$$

$$(27) \qquad \{\dot{u}(t+\Delta t)\} = \{\dot{u}(t)\} - [M]^{-1} [K] \{u(t+\Delta t)\}\Delta t - [M]^{-1}[C]\{\dot{u}(t)\}\Delta t + [M]^{-1} \{F(t)\} \Delta t$$

TEST

Based on the foregoing formulation, we have developed the computer programs. As an initial test of our three-dimensional program, we have studied the problem of wave propagation in a viscoelastic rectangular bar with one end of the bar fixed. The free end of the bar is subjected to a uniform external force load. The simulated forcing function is that of the sinusoidal type, using a four time-step of increasing (or decreasing) time. The maximum of the magnitude for the forcing function for the test case is 10^{10} dynes. In this test problem, we used only 20 hexahedron elements. Use of symmetry is made to reduce the size of the problem and the boundary displacements are prescribed in a manner shown in Figure 2. The elastic constants used are: Poisson's ratio = 0.25, Young's Modulus = 4.5×10^{10} dynes/cm^2. The dynamic damping behavior of unconsolidated earth materials primarily depend on the parameter of damping ratio λ_n, which must be determined by in-situ experimental measurements. On the basis of spectral studies of the damping behavior of unconsolidated earth materials, the U.S. Atomic Energy Commission Regulatory Guide, Directorate of Regulatory Standards indicates that the reasonable values of parameter λ_n are approximately in the range of 0.005 to 0.1. Figures 3 and 4 show the displacement-component responses on the surface of the bar, the observation point is located at the nodal point of 71 as shown in Figure 2, for the three cases:

(i) Response without damping.

(ii) Response with a damping ratio $\lambda_1 = 0.02$.

(iii) Response with a damping ratio $\lambda_1 = 0.05$.

The responses of U_x and U_y are exactly the same due to symmetry. In Figures 3 and 4, the magnitudes of U_x (or U_y) and U_z are drastically reduced for both the cases of $\lambda = 0.05$ and $= 0.02$. In this particular example, there is a slight phase change in U_x (or U_y) component, while the phase change in the U_z component is apparent.

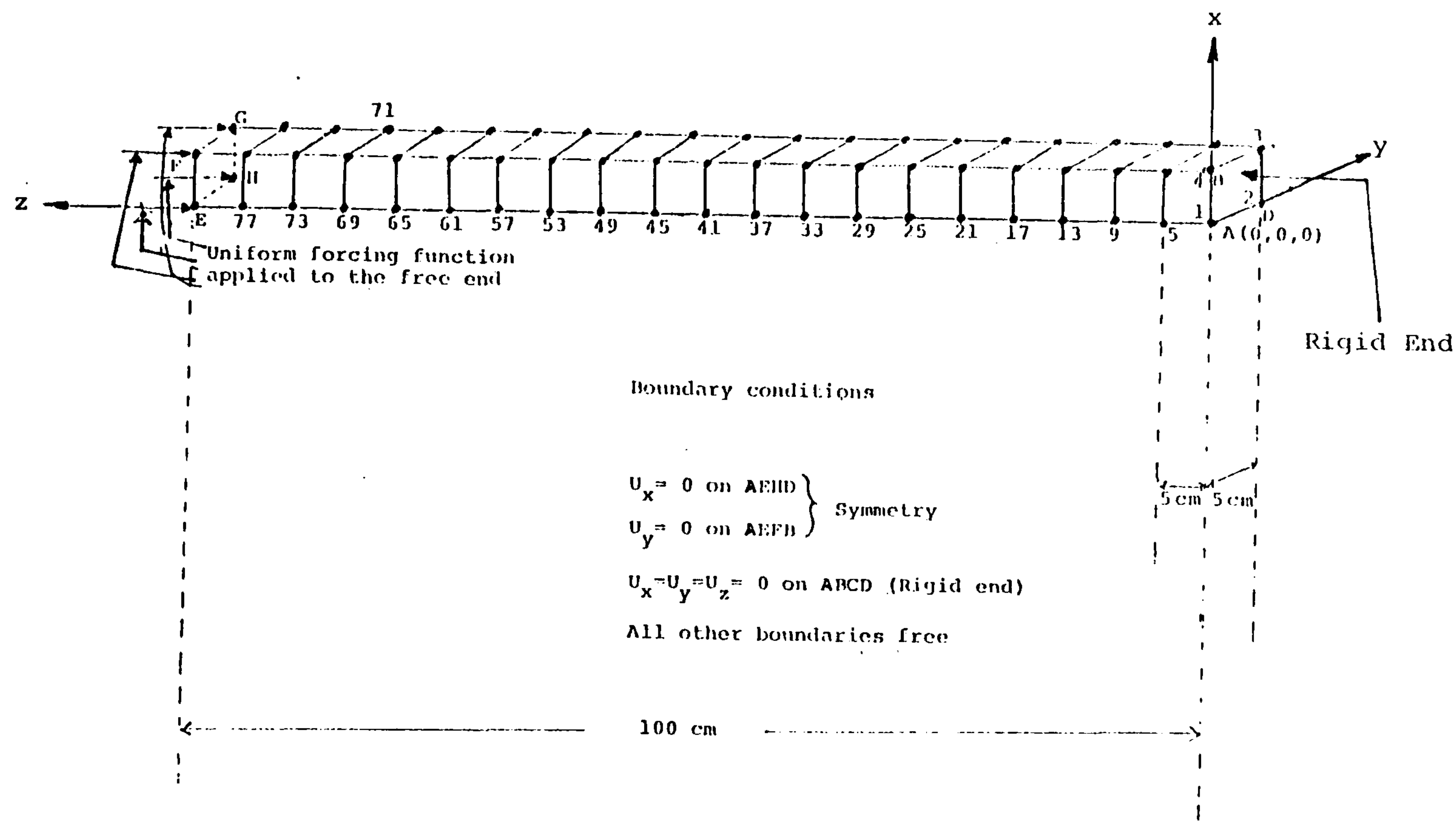

Figure 2. An Elastic (or Viscoelastic) Bar Subjected to a Uniform External Loading.

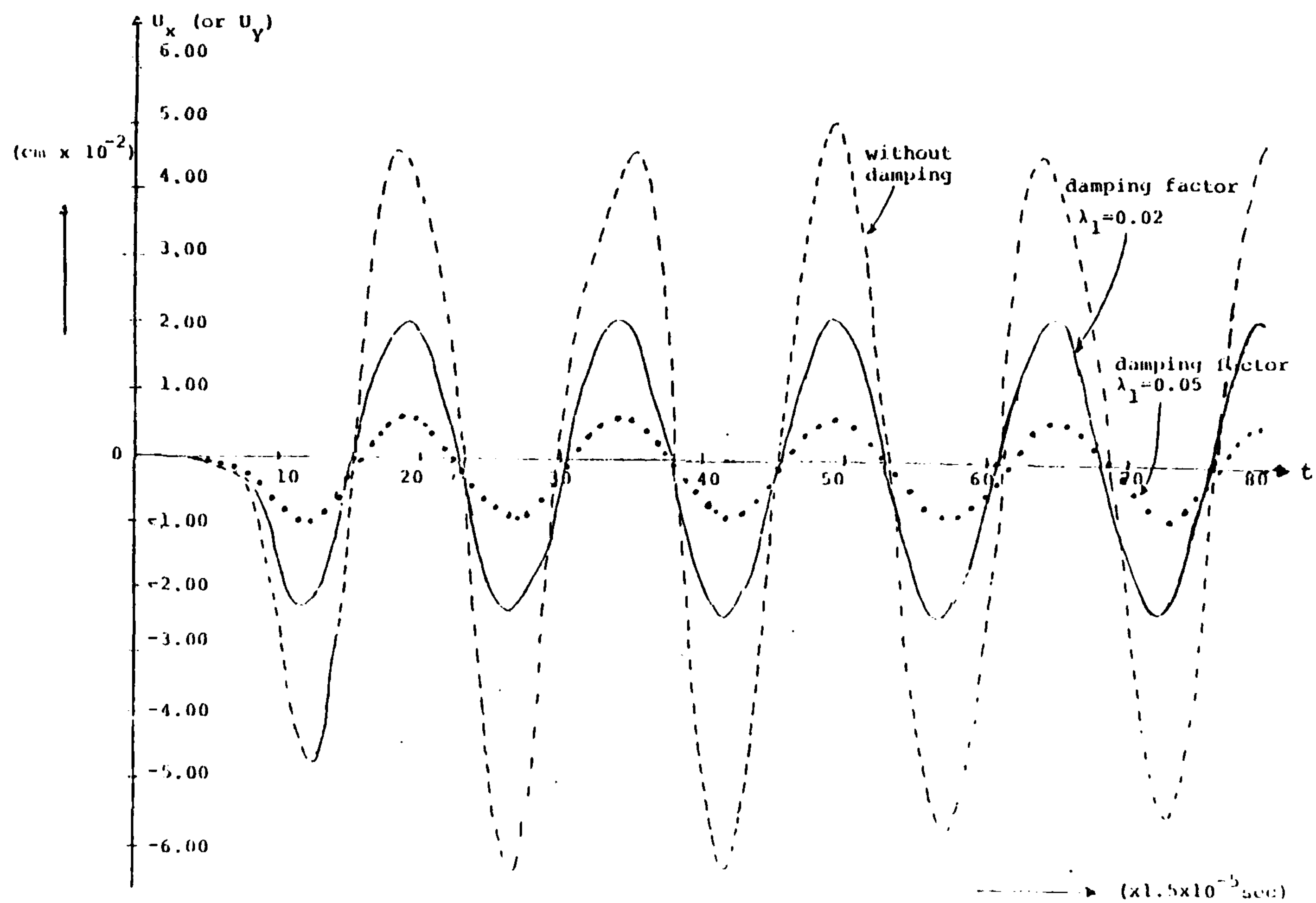

Figure 3. Comparison of Wave Propagations of an Elastic Bar and a Viscoelastic Bar.

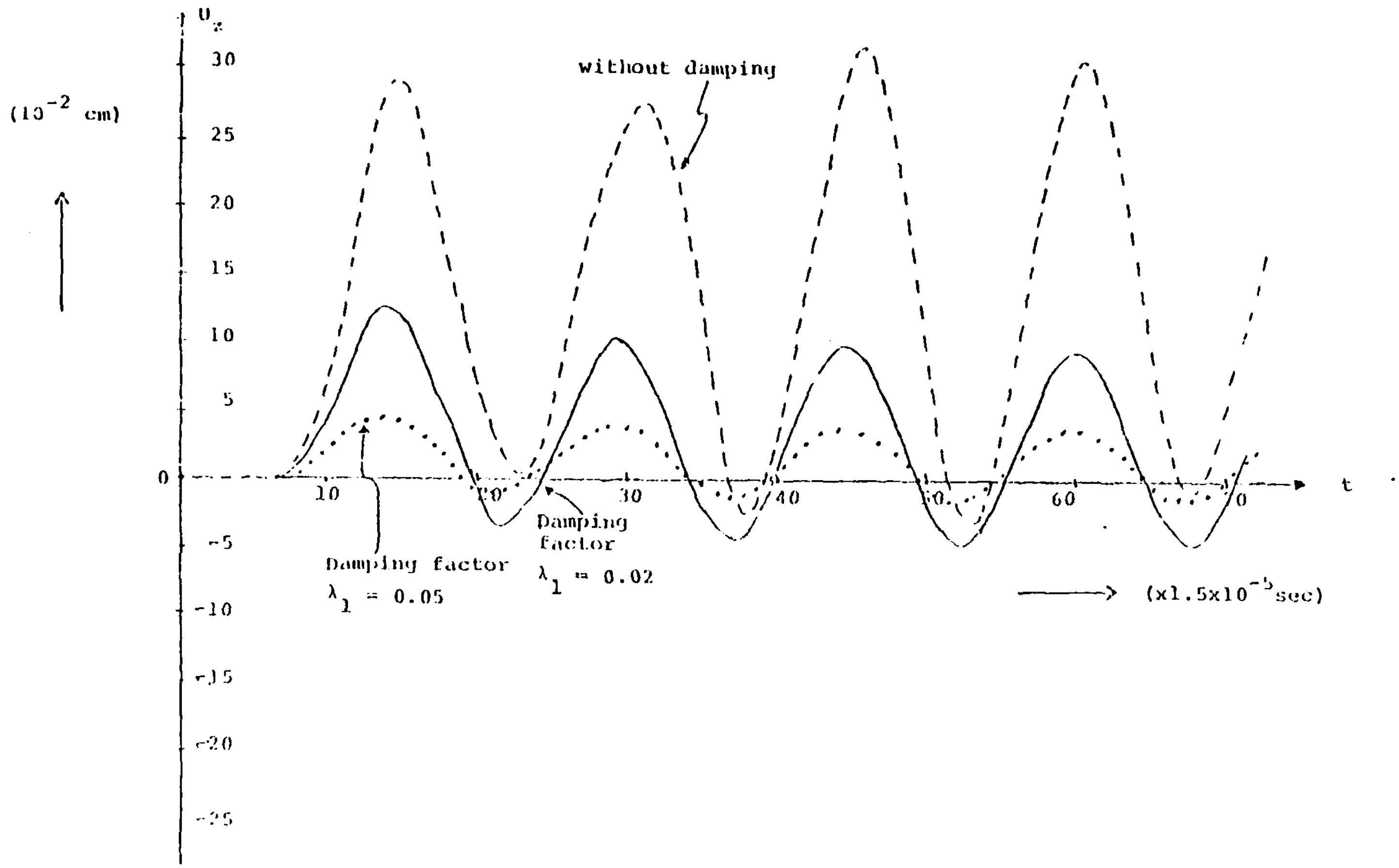

Figure 4. Comparison of Wave Propagations of an Elastic Bar and a Viscoelastic Bar.

MODIFYING ELASTODYSTATIC AND ELASTODYNAMIC FINITE ELEMENT COMPUTER PROGRAMS FOR REDUCING THE IN-CORE STORAGE

As we mentioned before, our original finite element computer programs have been developed in the conventional "block-by-block" format so that a large in-core storage for the global stiffness matrix was required and a large amount of computing time was also required. If we use the "block-by-block" format, it is a formidable task to handle even a small practical problem of a more realistic geological structure by the present art of the largest digital computers now available.

In the past year, we have substantially modified our three-dimensional elastodynamic and elastostatic computer programs for solving more realistic geological problems. We have overcome many serious difficulties of the finite element method for both elastodynamic and elastostatic problems.

(A) Elastodynamics

The final form of the finite element formulation of the equations of motion in elastodynamics is

$$[M]\{\ddot{u}\} + [K]\{u\} = \{F(t)\} \tag{28}$$

A Gaussian elimination algorithm is generally used to solve a discrete system of equations. However, matrices [K] and [M] must be in-core stored in the calculation that creates stringent limitation on the total number of equations to be solved.

Because the matrix [K] is usually sparse, a special ordering of the nodal points can produce a matrix [K], which is tightly banded about the main diagonal. In our original version of the Aldridge Finite Element Algorithm (AFEA), we used the conventional "block-by-block" format with the number of equations per block known, the stiffness matrix is assembled in one block at a time and is stored on the scratch disk. This "block-by-block" computer program requires (2B, B) words in-core for [K], where B is the half-band width. For example, for a three-dimensional 50x50x50 element structure, we would have to solve some 397,953 simultaneous equations for the assembly stiffness matrix with a half-band width of B=7959, and an in-core storage of 2x7959x7959x4=506,766 kilobytes. The banded and blocked character of [K] is as shown in Figure 5. The assembly mass matrix of the structure is formulated by lumping the weighted element masses at the nodal points of the elements. The mass of an element is weighted-distributed to the nodal points. In the present modified version of AFEA, taking the advantage of using the lumped mass matrix, and the finite differences time integration, we thus avoid the conventional Gaussian elimination algorithm. Instead, we solve the following equations,

$$(29) \qquad \{u(t+\Delta t)\}_N = \{\dot{u}(t)\}_N + (\{u(t)\}\Delta t)_N$$

$$(30) \qquad \{\dot{u}(t+\Delta t)\}_N = \{\dot{u}(t)\}_N + ([M]^{-1}[K]\{u(t+\Delta t)\})_N + ([M]^{-1} \{F(t)\} \Delta t)_N$$

where N = the total number of equations.

We operate only on the product $\left([M]^{-1} [K] \{u(t+\Delta t)\} \right)_N$.

Thus, we need only "N" words in-core, no matter how large the half-band width B may be. Figure 6 shows a comparison of the in-core storage for the global stiffness matrix required between the original and present modified versions of AFEA.

Additionally, the present modified AFEA codes save accounting time, since only the non-zero matrix elements in [K] are calculated. The blocked matrix [K] is sparse. The larger is the half-band width B, the more sparse the blocked [K] matrix will be. In the three-dimensional case, the maximum non-zero elements in each row are 81 for hexahedron elements. In two-dimensional case, the maximum non-zero elements in each row are 18 for quadrilateral elements. In other words, there are (7959-81) zero matrix elements in each row for the 50x50x50 element-structure. Therefore, in using the present modified AFEA, the computing time can be reduced for solving larger element-structures without the increasing I/O time. Table I gives the comparison of the accounting time for the original and present modified versions of AFEA in solving both two-dimensional and three-dimensional elastodynamic problems on an IBM 360/91.

As our first example, in using the modified three-dimensional elastodynamic program of AFEA, we studied the classic Lamb's problem, i.e., the problem of a homogeneous, isotropic, elastic half-space, subjected to an external vertical force on the free surface, which is assumed to be a bell-shaped function. In this test problem, we used 12 hexahedron elements in each dimension (Figure 7). Use of

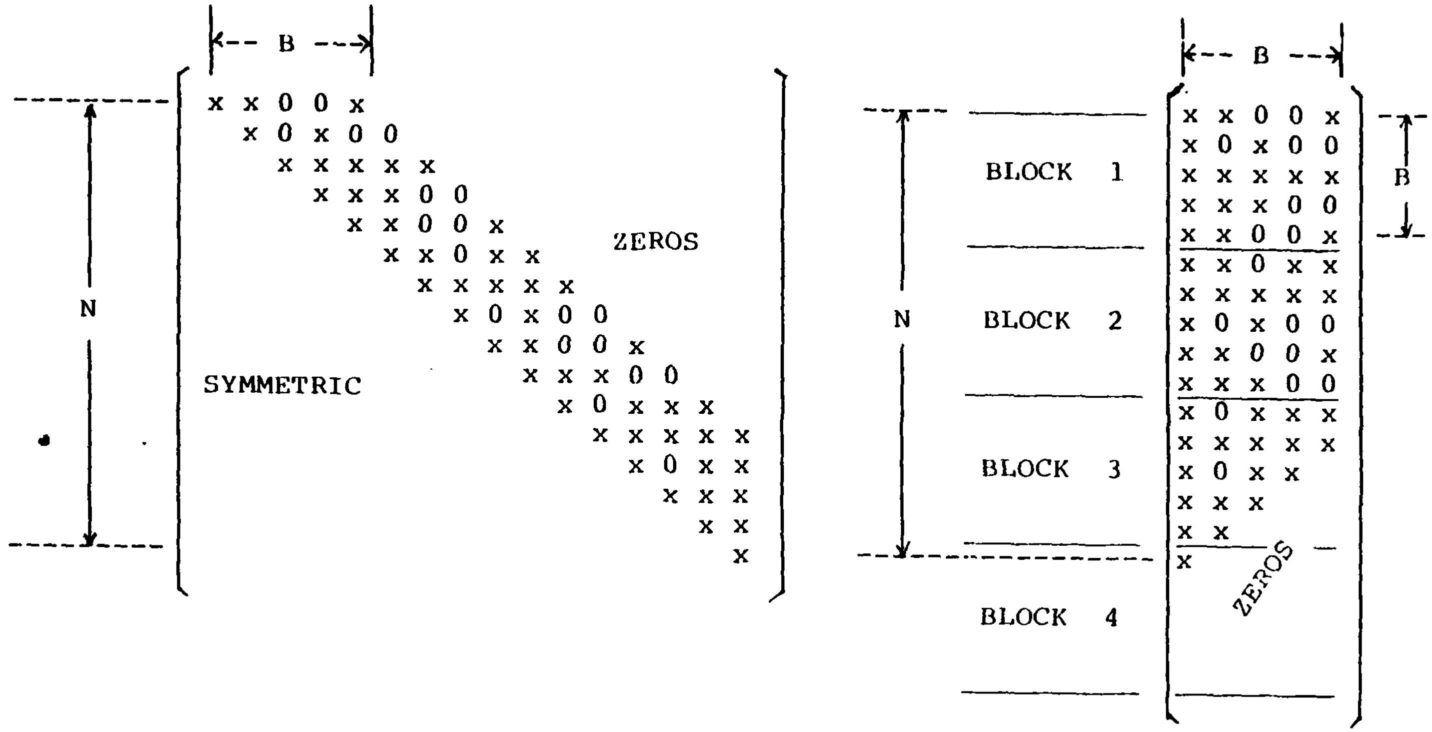

ACTUAL STRUCTURE OF
STIFFNESS MATRIX

BLOCK-STORAGE STRUCTURE
OF STIFFNESS MATRIX

x = Nonzero element

0 = Zero element

B = Half-bandwidth

N = Total numbers of equations

FIGURE 5. Storage of Stiffness Matrix.

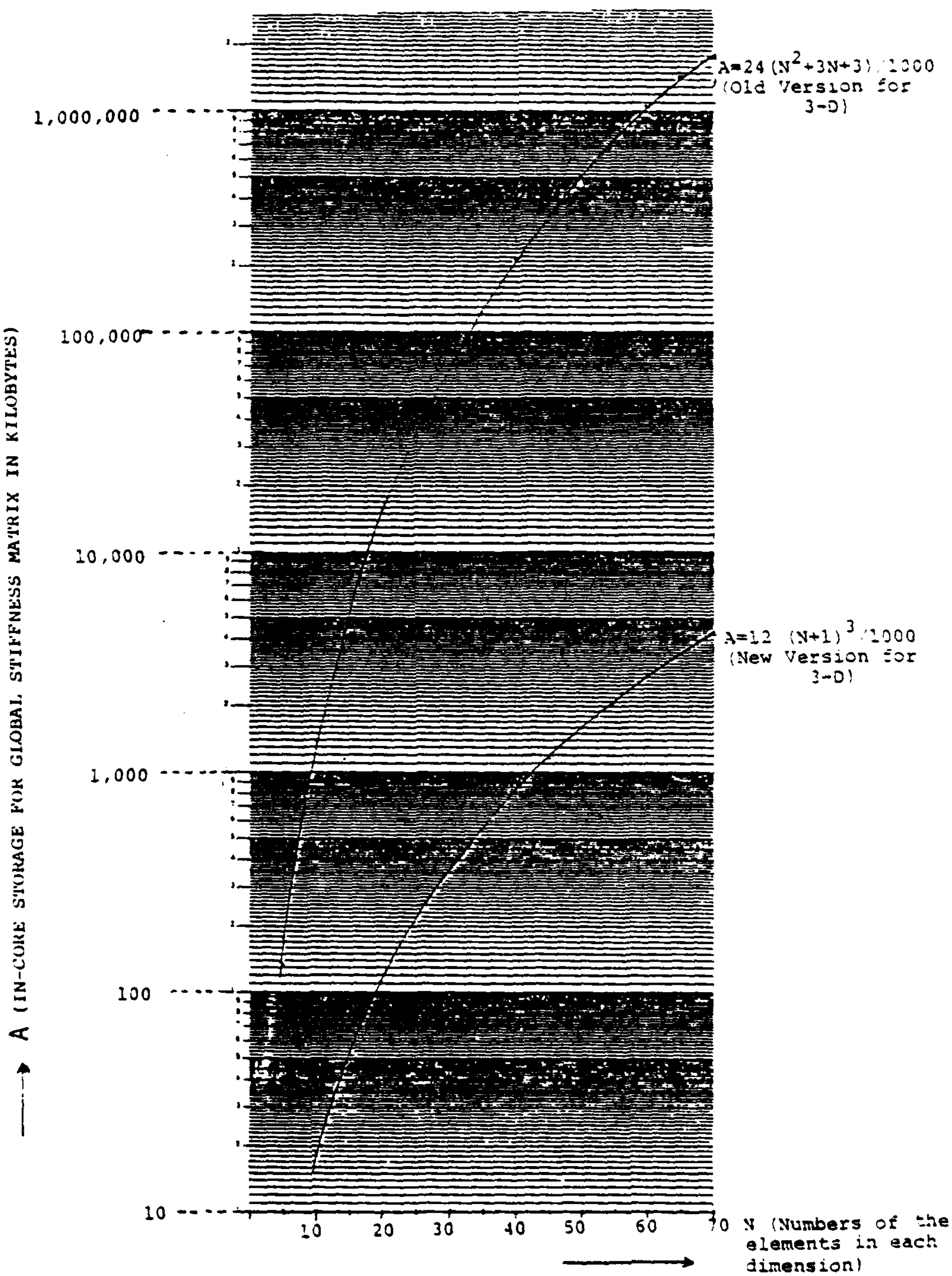

Figure 6. Comparison of the Original and the Modified Versions for In-core Storage (Global Stiffness Matrix).

	THREE-DIMENSION		TWO-DIMENSION	
	PRESENT MODIFIED VERSION	BLOCK-BY-BLOCK VERSION	PRESENT MODIFIED VERSION	BLOCK-BY-BLOCK VERSION
ELEMENTS USED	20	20	280	280
NUMBERS OF EQUATION	252	252	315	315
TIME STEPS CALCULATED	15	15	100	100
ACCOUNTING TIME	34.6 sec	36.84 sec	175.89 sec	195.16 sec

TABLE I. Comparison of the Accounting Time for the Original and Present Modified Versions of AFEA.

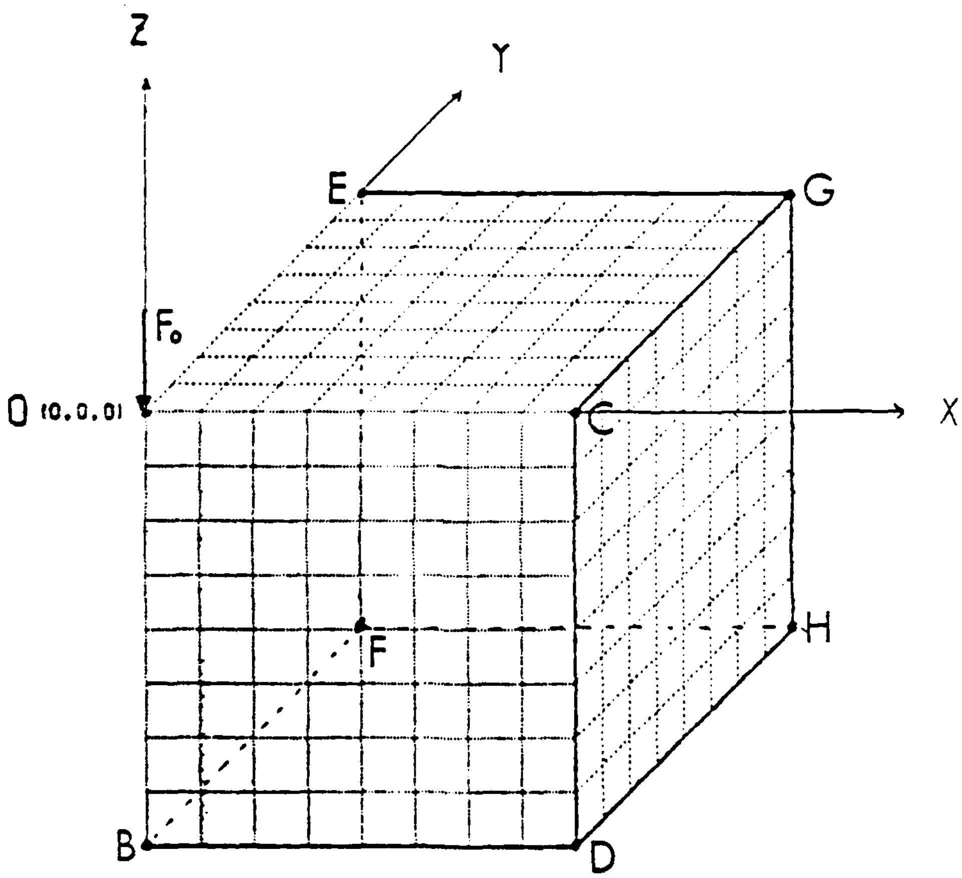

Figure 7. Finite Element Mesh for Lamb's Problem.

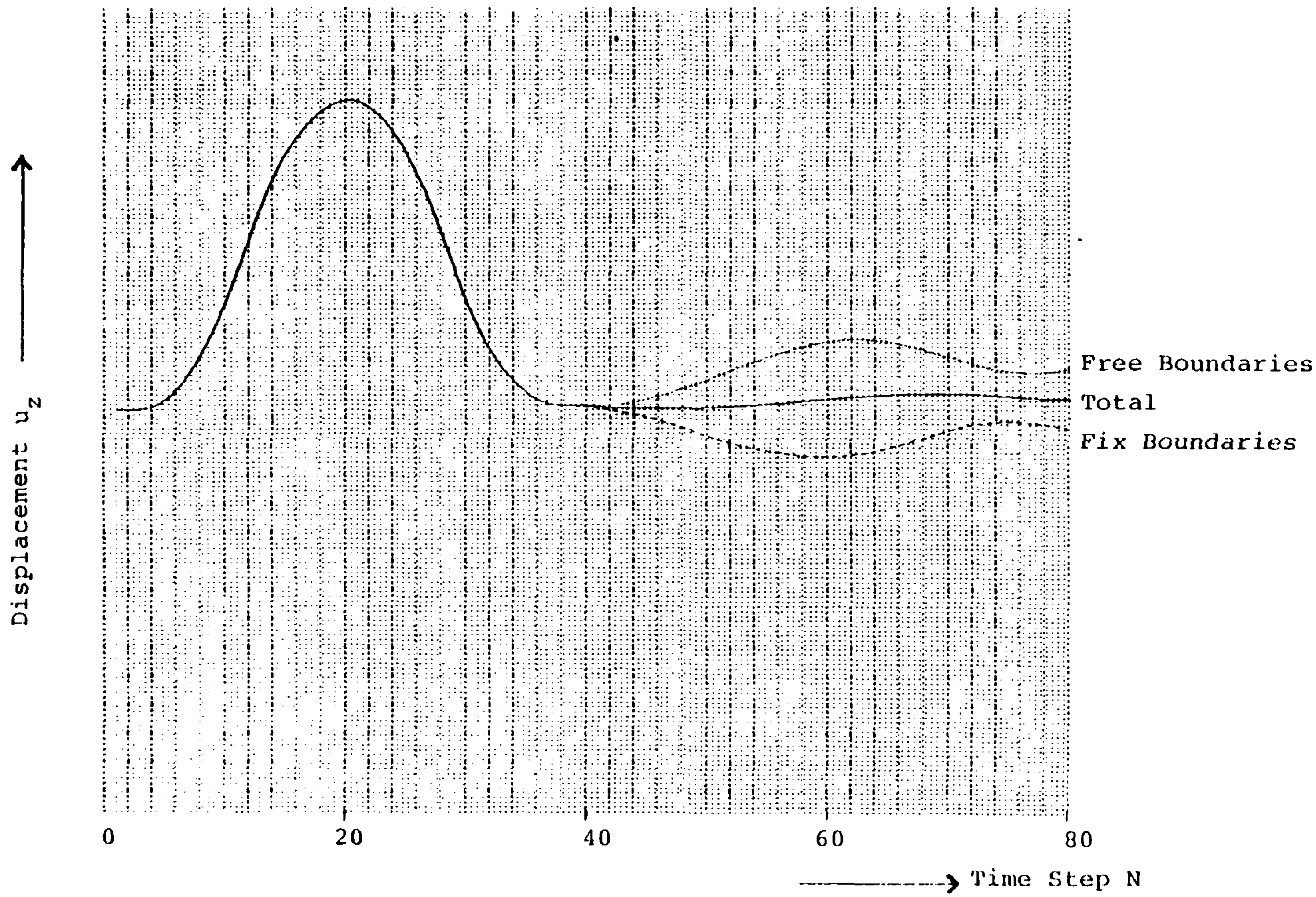

Figure 8. Superimposing the Solutions of the Free and Fix Boundary Problems for Finite Element Mesh 12x12x12

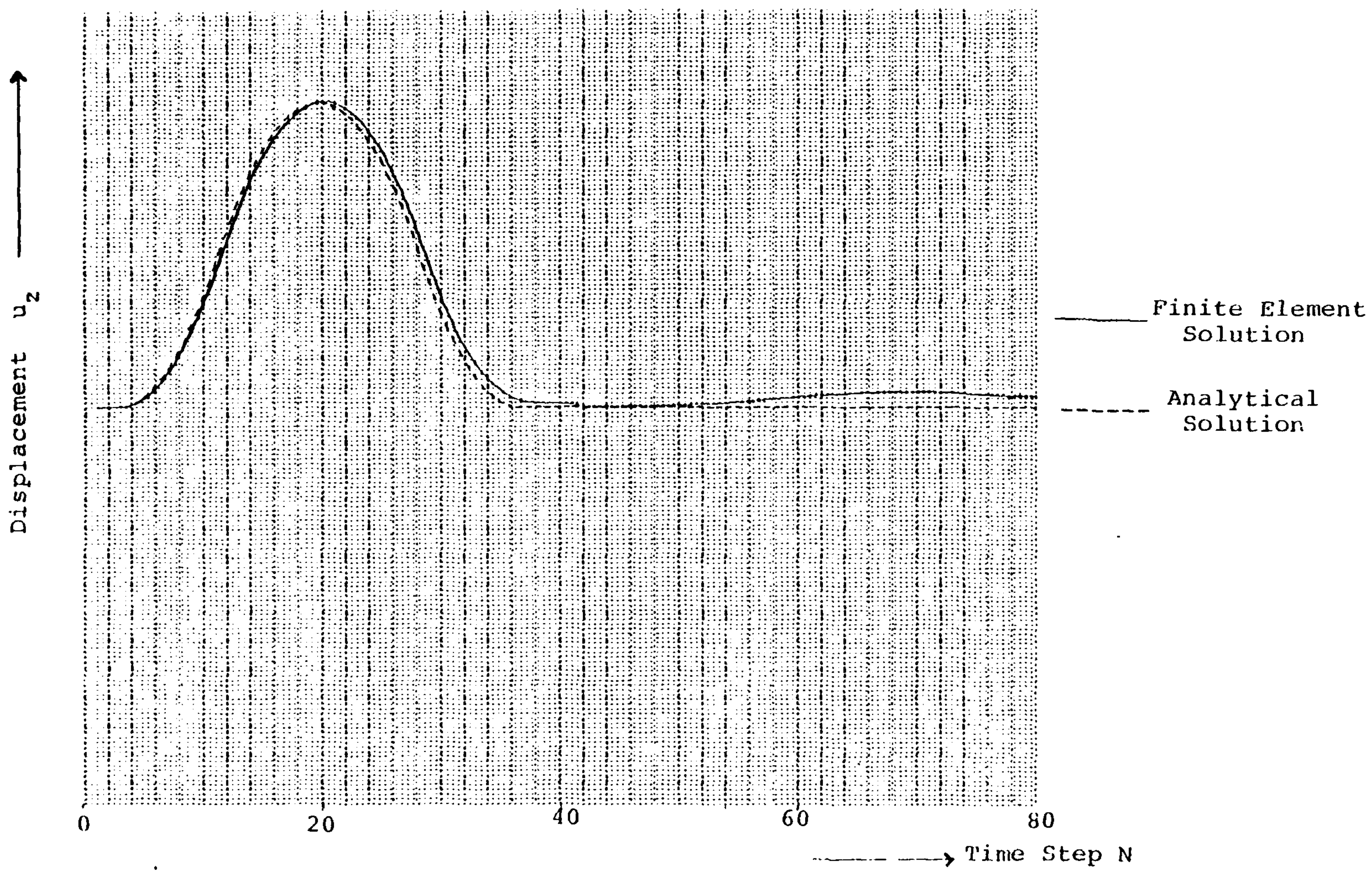

Figure 9. Comparison of the Finite Element and the Analytical Solutions. (Finite Element Mesh : 12x12x12)

symmetry is made to reduce the size of the problem. The symmetric boundary conditions in Figure 7 are:

$$U_x = 0 \text{ on OBDC}$$

$$U_y = 0 \text{ on OBFE}$$

In addition we used Smith's technique (1974) to eliminate the single boundary reflections by superimposing the solutions of free-artificial-boundaries and rigid-artificial-boundaries problems. Although the technique fails, when multi-reflections occur at the same boundary, and has the disadvantage of requiring 2^n solutions for the n number of non-reflecting boundaries, we prefer this method at present because it offers the advantages of perfect elimination, i.e. independent of both incident angle and frequency. The Smith's technique is particularly advantageous for three-dimensional finite element problems since the number of elements required is reduced by 8. Figure 8 shows the superposition of the solutions of the free and boundary problems. Figure 9 shows the comparison of the finite element and the analytical solutions. The test results are highly accurate with the displacement component being within about 2 % of the analytical value.

(B) Elastostatic Case

For the elastostatic case, a conventional Gaussian elimination is needed. In the new version of AFEA, we developed a small band solver that can be used with tape-storage to solve a large system of linear equations. Instead of requiring the in-core storage of (2B, B) words for [K] in the orginal version, the required in-core storage now for [K] reduces to (2 x NF, B) words where NF is the numbers of degree freedom, that is, an in-core storage of (6, B) words for the three-dimensional case and of (4, B) words for the two-dimensional case. Figure 10 gives a comparison of the in-core storage for the global stiffness matrix required in the original and new modified versions. It is expected that the large number of calls to tape requires a large amount of I/O time.

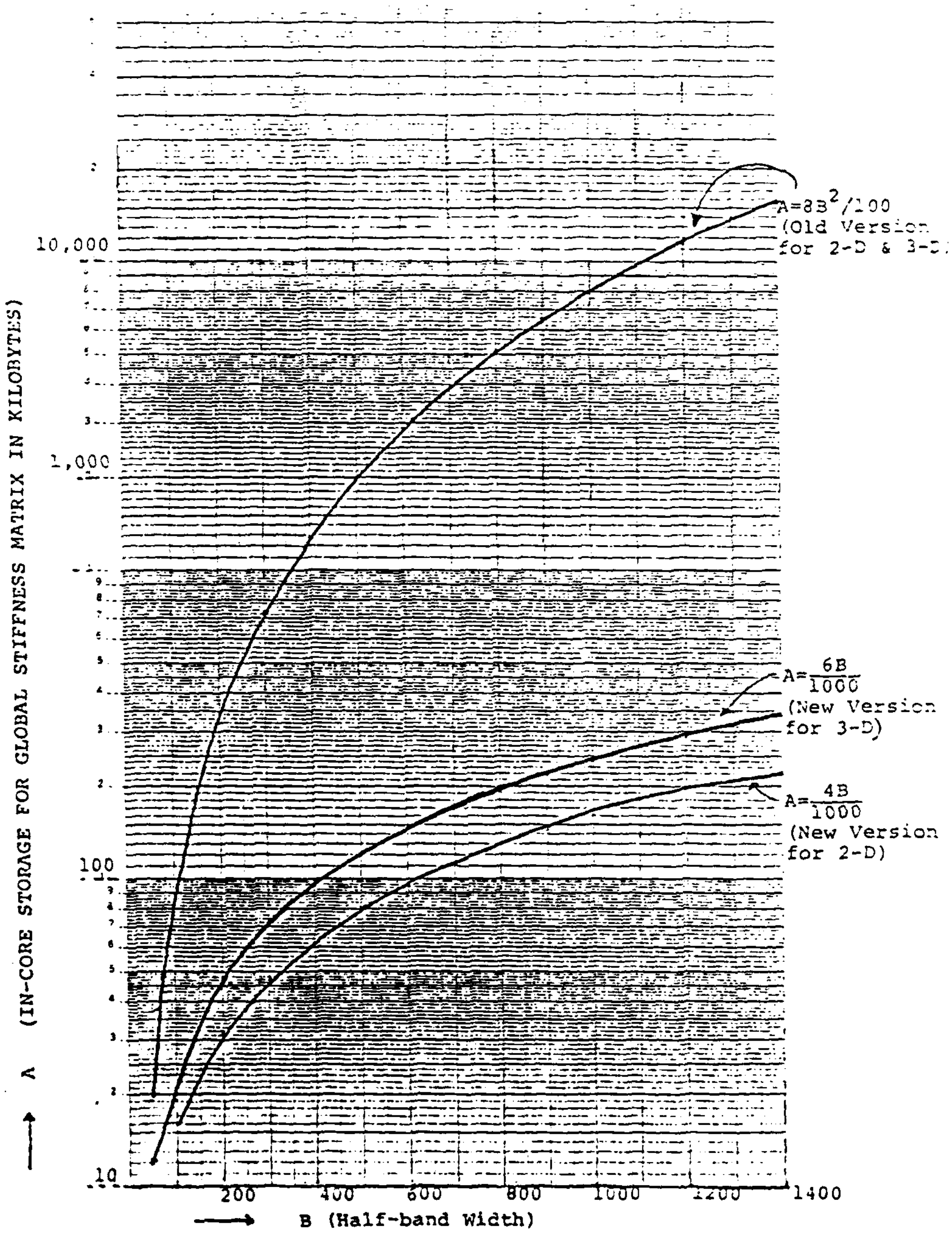

Figure 10. Comparison of the Original and the Modified Versions for In-core Storage (Global Stiffness Matrix).

STABILITY CONDITION AND CONVERGENCE CRITERIA OF THE FINITE ELEMENT IN SPACE AND THE FINITE DIFFERENCES IN TIME

Ever since the finite element method emerged in various branches of engineering and physics, many investigators have attempted to establish the convergence criteria and the stability condition techniques for the FEM in space and the FDM in time.

Based on the principle of virtual work, the FEM involves the whole region of interest, which is discretized into a finite number of subregions. The accuracy of the analysis depends mainly on the number of elements used, and on the nature of the assumed displacement functions with the elements. The accuracy of analysis can be increased by using more elements in the representation of the structure provided that the elements satisfy certain convergence criteria, that is, the elements must be complete and compatible.

Whether a specific element is complete and compatible depends on the formulation that must be studied individually. The aim in the numerical integration of the finite element system equilibrium is to evaluate a good approximation to the actual dynamic response of the structure under consideration. The choosing time step must correspond to the smallest period in the system which could mean very small time steps.

In the AFEA, i.e., finite element in space and finite differences in time, we found that the elements of 4CST (four constant strain triangles) for two-dimensional cases and 5CST (five constant strain tetrahedra) for three-dimensional cases in space integration are complete and compatible, and central differences of time steps in time integration are adequate. It follows that the element size Δx, Δy, or Δz in comparison with the wavelength of wave propagation plays a crucial role in convergence. As in time integration, the number of operations required is directly proportional to the number of time steps required for the solution. The selection of an appropriate time step Δt in time integration is of great importance in obtaining a stable solution. On one hand, the finite element size and the time step must be small enough to obtain a stable solution, and, on the other hand, the element size must not be smaller than necessary, because this would mean that the computation is more costly and requires more in-core storage than actually needed. Choosing a time step smaller than necessary not only increases the cost of calculation; it also causes an inaccurate result. A common mistake is choosing a coarse grid of elements and a small time step. We have tested the convergence criteria and stability condition by using one of our computer program codes for the two-dimensional plane strain elastodynamic calculation, again the best case is that of Lamb's problem. The following forcing function is used,

$$
\begin{aligned}
F(t) &= \frac{1}{\Delta\tau^2} [H(t-\Delta\tau) - H(t-3\Delta\tau)] \\
&+ \frac{1}{\Delta\tau^2}[\Delta t^2 - 2(t-\Delta\tau)^2]\ [H(t-3\Delta\tau) - H(t-4\Delta\tau)] \qquad (31) \\
&+ \frac{1}{\Delta\tau^2}[(t-4\Delta\tau)^2]\ [H(t-4\Delta\tau+\Delta t)]
\end{aligned}
$$

in which the factor $\Delta\tau$ controls the rise of the step. We found that with various element sizes (Δx, Δy), various time steps (Δt), and various forcing function sharpness factors ($\Delta\tau$), the present finite element model requires the ratio $\xi = V_p \Delta t/\Delta s$ be greater than 1.2 and $\Delta\tau$ be greater than 10 Δt, where V_p is the compressional velocity and Δs is the smallest width of the element in the finite element assemblage. As an estimate of Δs is required, it appears that if the average period is T_n, Δs would have to be about $T_n V_p/10$. Figure 11 gives the finite element mesh of the two dimensional Lamb's problem. In Figure 11, use of symmetry is made to reduce the size of the problem. Although the grid sizes used are regular, both element size and shape may vary. Synthetic seismograms at various nodal points along the free surface have been generated with $\xi = 1.5$ and $\Delta\tau = 12\Delta t$ (Figure 12a and 12b). Figure 13 shows the diagram of the particle motion at an observation point on the free surface. The characteristic elliptic retrograde particle motion of Rayleigh wave is clearly identified.

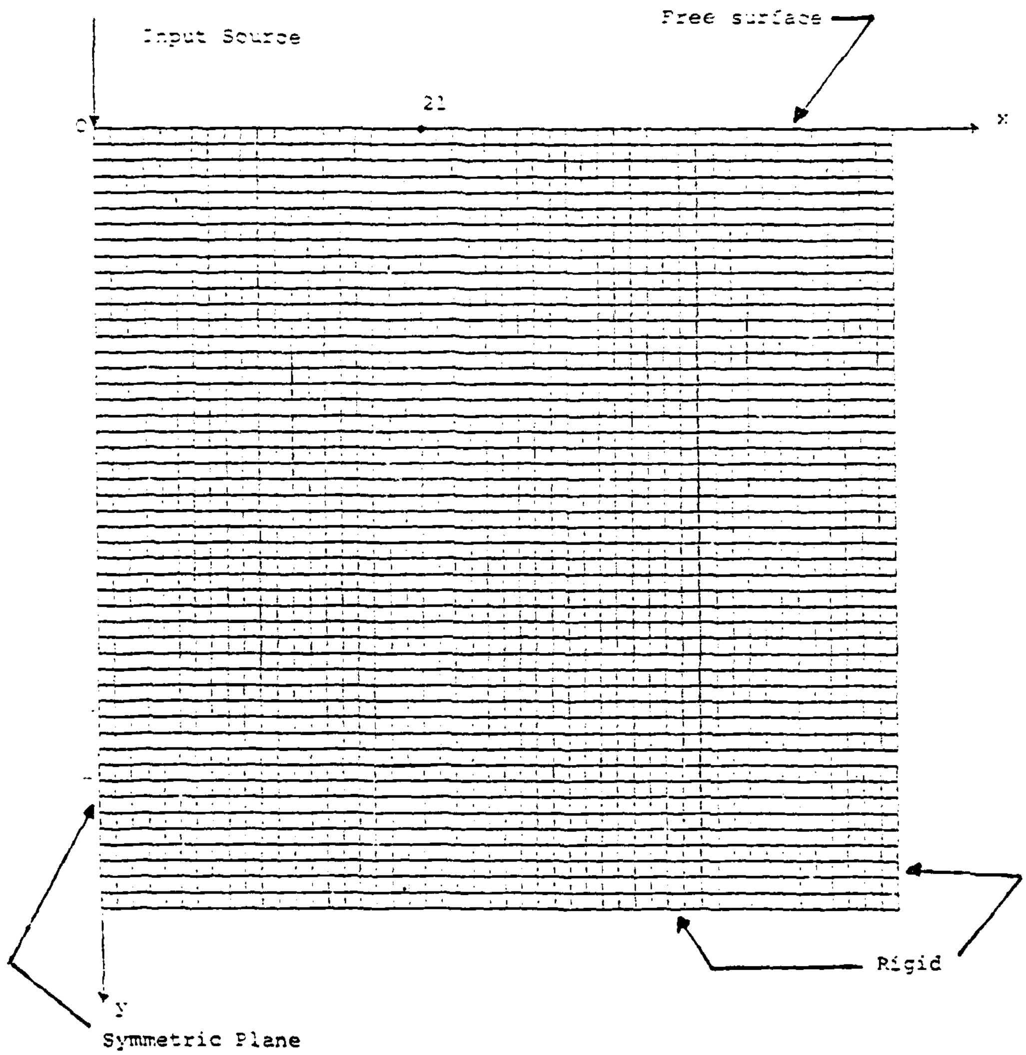

Figure 11. Finite Element Mesh for Two-dimensional Lamb's Problem.

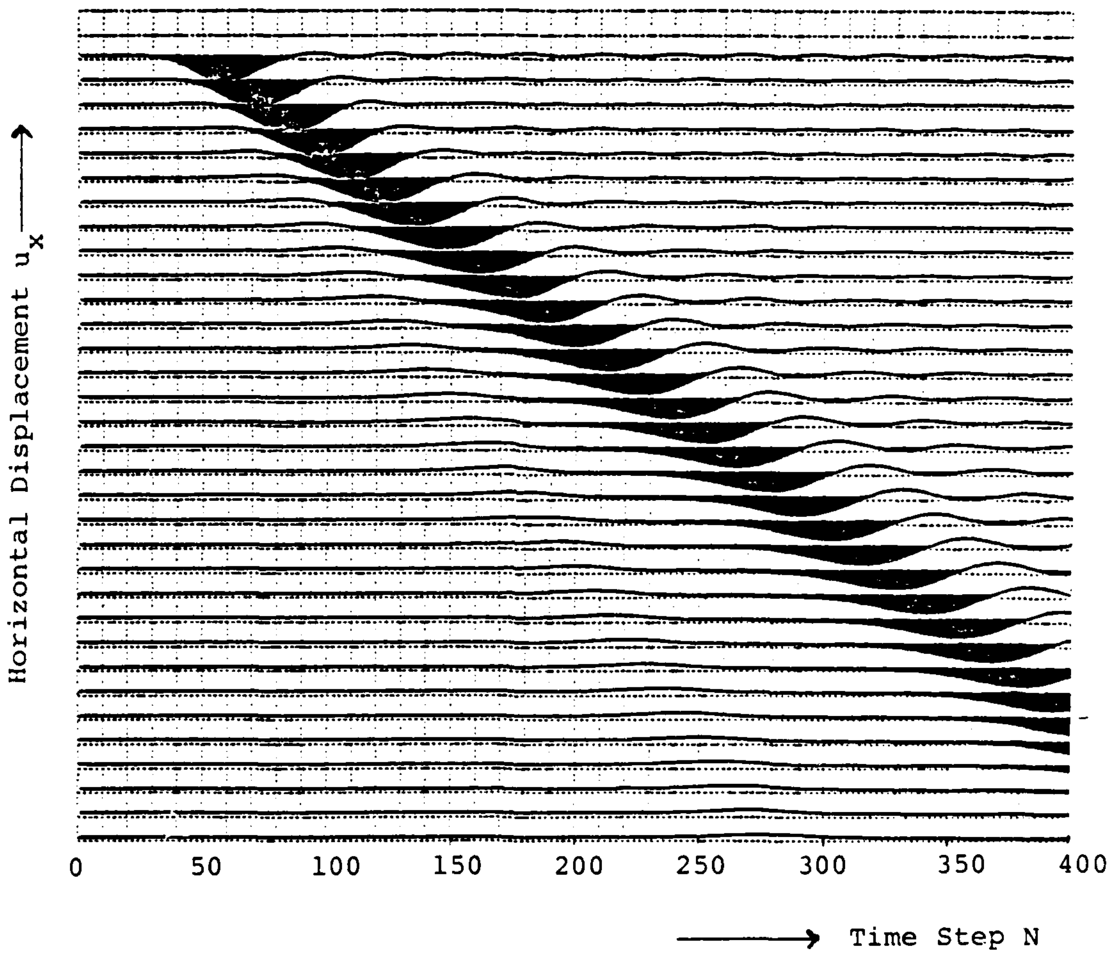

Figure 12a. Horizontal Displacement on the Free Surface.

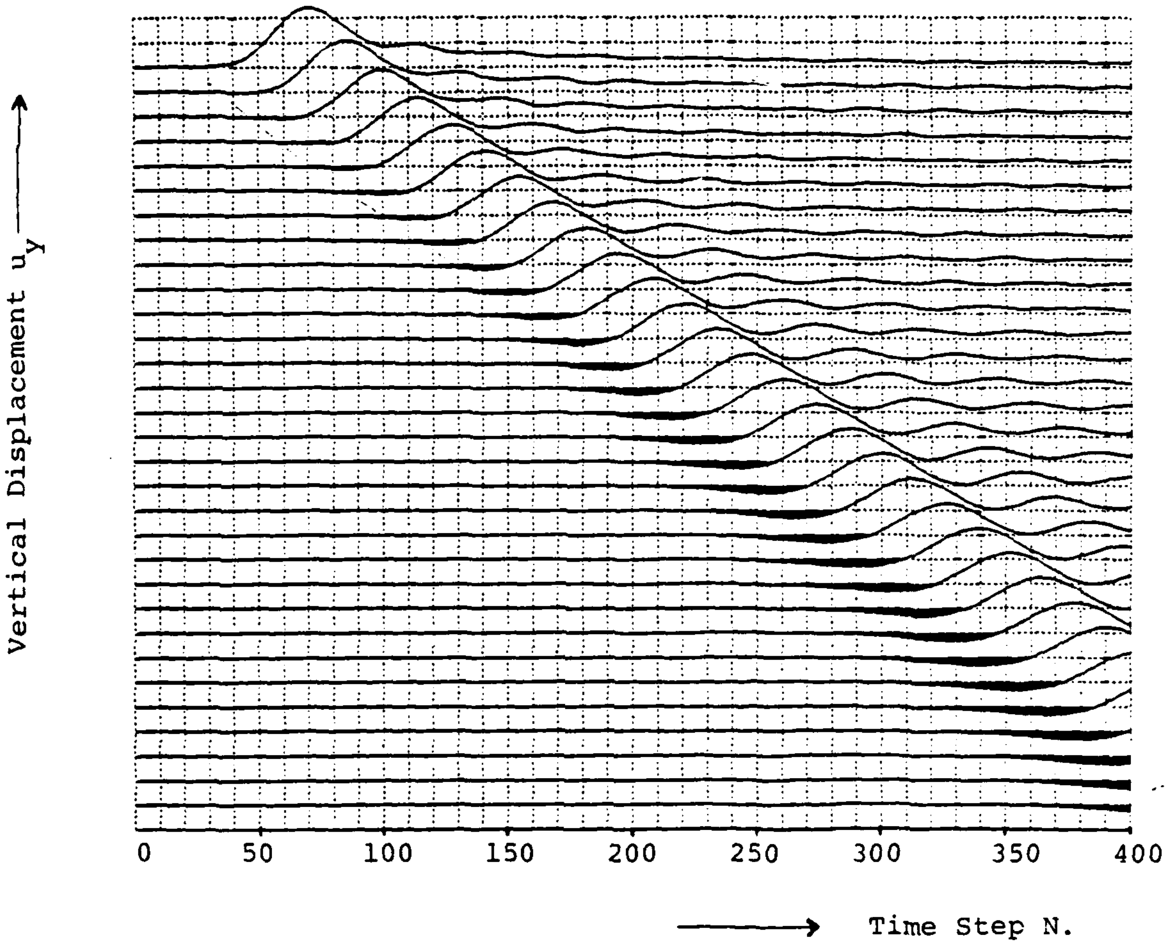

Figure 12b. Vertical Displacement on the Free Surface.

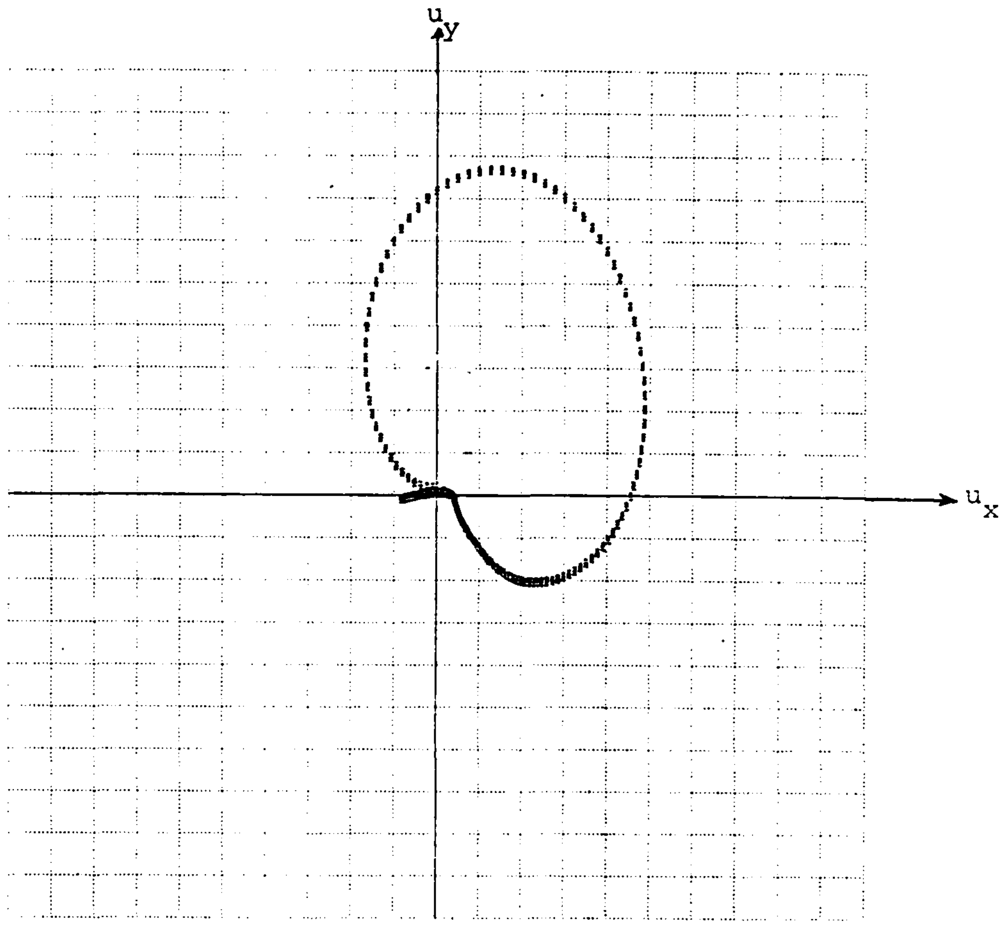

Figure 13. Diagram of Particle Motion at Observation Point 21.

REFERENCES

Caughey, T.K., "Classical Normal Modes in Damped Linear Dynamic System", J. of Appl. Mech., Vol. 27, 1960, pp. 269-271.

Kuo, J.T., Y.C. Teng, K.H. Chen, and L.F. Hwang, "Numerical and Analytical Solutions to Elastodynamic Problems", AFOSR-76-2908, Final Report.

Lord Rayleigh, "Theory of Sound", Vol. I, Dover Publications, Inc., 1945.

Smith, W., "A Non-reflecting Plane Boundary for Wave Propagation Problems", J. Comp. Phys. 15 1973, pp.492-503.

II. THE PERTURBATION METHOD APPLIED TO SOLVE ELASTODYNAMIC PROBLEMS

ABSTRACT

The root-mean-square perturbation method for solving wave scattering and diffraction introduced by Thau and Pao has been further developed to include the higher order terms. The method is particularly suited for solving, for example, the classic problem of wave propagation in a wedged medium. As an illustration, the formal solutions to the problem of SH-wave propagation in a wedged half-spce are obtained. Future numerical evaluation of the solutions is in order.

INTRODUCTION

In solving elastodynamic boundary value problems, the dual existence of two different types of elastic waves, compressional wave and shear wave, even in a homogeneous, isotropic, elastic solid body has frustrated many theoreticians to solve some practical, as yet complex problems in seismology. For example, the use of Kontorowich-Lebedev transform will yield a solution to the single scalar field problems of acoustic, SH- or electromagnetic wave propagation. However, the use of Kontorowich-Lebedev transform is no value in obtaining formal solutions in the elastic solid wedge problem of P and S wave propagation.

Thau and Pao (1967) introduced a perturbation method, in which the two different wave numbers in the two steady state wave equations are replaced by their root-mean-square (RMS) average value. All the perturbed wave equations and boundary conditions involve only the RMS value, that is, there is only one single wave number involved. The perturbation parameter, which is a small quantity, is the difference of the actual wave number and the RMS-value. They generated the perturbation solutions of the first three orders, viz. the zeroth, the first, and the second order. They also illustrated the application of this perturbation method to solve elastic wave diffraction problems. Based on their two-term perturbation solutions of the zeroth, and the first order, the results are in good agreement with the known exact near field solutions at low frequencies.

In this paper, we present the recursive formulas, which can generate any higher order solutions for this RMS-value perturbation method.

HIGH-ORDER SOLUTIONS

Thau and Pao showed that, for the steady state motion, the two Helmholtz equations for elastic waves are

$$(1) \qquad (\nabla^2 + k^2)\, w_1 = 0$$

$$(2) \qquad (\nabla^2 + k_2^2)\, w_2 = 0$$

where ∇^2 is the Laplacian operater.

$$(3) \qquad k_1 = \omega / v_1$$

$$(4) \qquad k_2 = \omega / v_2$$

ω is the frequency, v_1 and v_2 are velocities and $v_2 > v_1$. For the SH-wave problems in two media, v_1 and v_2 are the shear velocities, and w_1 and w_2 are the z-direction displacement components for the two different media, respectively. For waves in an elastic solid, v_1 is the shear wave velocity, v_2 is the compressional wave velocity, and w_1 and w_2 are the displacement potentials. For simplicity and without loss of generality, here only one component of the vector displacement potentials is considered. For example, for the plane-strain problems, the displacement vector is

$$(5) \qquad \mathbf{u} = \boldsymbol{\nabla} w_2 + \boldsymbol{\nabla} \times \hat{k}\, w_1$$

Omiting the factor exp(-iωt), we can easily find the equivalencies for the acoustic and electromagnetic waves.

Let

(6) $$k^2 = (k_1{}^2 + k_2{}^2)/2$$

(7) $$k_1{}^2 = k^2(1 + 2\varepsilon)$$

(8) $$k_2{}^2 = k^2(1 - 2\varepsilon)$$

where

(9) $$\varepsilon = \frac{k_1^2 - k_2^2}{2(k_1^2 + k_2^2)}$$

is the perturbation parameter

Assume that

(10) $$w_1 = w_1^{(o)} + \varepsilon\, w_1^{(1)} + \varepsilon^2 w_1^{(2)} + \cdots\cdots + \varepsilon^n w_1^{(n)} + \cdots\cdots$$

(11) $$w_2 = w_2^{(o)} + \varepsilon\, w_2^{(1)} + \varepsilon^2 w_2^{(2)} + \cdots\cdots + \varepsilon^n w_2^{(n)} + \cdots\cdots$$

Substituting (7), (8), (10), and (11) into (1) and (2) and equating coefficients of like powers of the n-th order wave equations, we heve:

(12) $$(\nabla^2 + k^2)\, w_1^{(n)} = -2\, k^2\, w_1^{(n-1)}$$

$$(13) \qquad (\nabla^2 + k^2) w_2^{(n)} = + 2 k^2 w_2^{(n-1)}$$

with n = 1,2,3,..........

For n = 0, the wave equations become:

$$(14) \qquad (\nabla^2 + k^2) w_1^{(o)} = 0$$

$$(15) \qquad (\nabla^2 + k^2) w_2^{(o)} = 0$$

For higher orders ($n \neq 0$), the total solutions of (12) and (13) include two parts:

$$(16) \qquad w_1^{(n)} = w_{1c}^{(n)} + w_{1p}^{(n)}$$

$$(17) \qquad w_2^{(n)} = w_{2c}^{(n)} + w_{2p}^{(n)}$$

where $w_{1c}^{(n)}$ and $w_{2c}^{(n)}$ are the complementary solutions, which satisfy the homogeneous equations

$$(18) \qquad (\nabla^2 + k^2) w_{1c}^{(n)} = 0$$

$$(19) \qquad (\nabla^2 + k^2) w_{2c}^{(n)} = 0$$

$w_{1p}^{(n)}$ and $w_{2p}^{(n)}$ are the particular solutions, which can be obtained from the lower order solutions and satisfy the following inhomogeneous equations:

$$(\nabla^2 + k^2)\, w_{1p}^{(n)} = -2k^2 w_1^{(n-1)} \tag{20}$$

$$(\nabla^2 + k^2)\, w_{2p}^{(n)} = -2k^2 w_2^{(n-1)} \tag{21}$$

The particular solutions for the first, the second, and the third orders are:

$$w_{1p}^{(1)} = \underset{\sim}{r} \cdot \underset{\sim}{\nabla} w_1^{(o)} \tag{22}$$

$$w_{2p}^{(1)} = -\underset{\sim}{r} \cdot \underset{\sim}{\nabla} w_2^{(o)} \tag{23}$$

$$w_{1p}^{(2)} = \underset{\sim}{r} \cdot \underset{\sim}{\nabla} w_1^{(1)} - w_{1p}^{(1)} + \frac{1}{2} k^2 r^2 w_1^{(o)} \tag{24}$$

$$w_{2p}^{(2)} = -\underset{\sim}{r} \cdot \underset{\sim}{\nabla} w_2^{(1)} + w_{2p}^{(1)} + \frac{1}{2} k^2 r^2 w_2^{(o)} \tag{25}$$

$$w_{1p}^{(3)} = \frac{1}{3}\{\underset{\sim}{r} \cdot \underset{\sim}{\nabla}[2w_1^{(2)} + w_{1c}^{(2)} + w_{1c}^{(1)}] - 4w_{1p}^{(2)} + \tfrac{1}{2} k^2 r^2 w_1^{(1)}\} \tag{26}$$

$$w_{2p}^{(3)} = -\frac{1}{3}\{\underset{\sim}{r} \cdot \underset{\sim}{\nabla}[2w_2^{(2)} + w_{2c}^{(2)} - w_{2c}^{(1)}] + 4w_{2p}^{(2)} + \tfrac{1}{2} k^2 r^2 w_2^{(1)}\} \tag{27}$$

The n-th order particular solutions are:

(28) $$w_{1p}^{(n)} = \frac{1}{a_1}\{(\underset{\sim}{r}\cdot\underset{\sim}{\nabla})\ [(n-1)w_1^{(n-1)} + a_2 w_{1c}^{(n-1)} + b_2 w_{1c}^{(n-2)}]$$
$$-[(2n-3)+b_2]\ w_{1p}^{(n-1)} + \tfrac{1}{2} k^2 r^2 w_1^{(n-2)}$$
$$+ (-1)^n\ [I_1 + I_2 + \cdots\cdots + I_{n-1} + I_n]\}$$

(29) $$w_{2p}^{(n)} = \frac{1}{a_1}\{-(\underset{\sim}{r}\cdot\underset{\sim}{\nabla})\ [(n-1)w_2^{(n-1)} + a_2 w_{2c}^{(n-1)} - b_2 w_{2c}^{(n-2)}]$$
$$+ [(2n-3)+b_2]w_{2p}^{(n-1)} + \tfrac{1}{2} k^2 r^2 w_2^{(n-2)}$$
$$+ [I_1 - I_2 + \cdots\cdots\cdots + (-1)^{n-1} I_{n-1} + (-1)^n I_n]\}$$

where

(30) $$a_1 = \sum_{m=1}^{n-1}(m)\ ,\ a_2 = \sum_{m=1}^{n-2}(m)\ ,\ a_3 = \sum_{m=1}^{n-3}(m)\ ,\ a_4 = \sum_{m=1}^{n-4}(m)$$

(31) $$b_1 = \sum_{m=1}^{n-2}(2m-1)\ ,\quad b_2 = \sum_{m=1}^{n-3}(2m-1)\ ,\quad b_3 = \sum_{m=1}^{n-4}(2m-1)$$

(32) $$I_1 = (\underset{\sim}{r}\cdot\underset{\sim}{\nabla})(\underset{\sim}{r}\cdot\underset{\sim}{\nabla}-2)[a_3 w_{1c}^{(n-2)} + b_3 w_{1c}^{(n-3)}]\ /2!$$

(33) $$I_2 = (\underset{\sim}{r}\cdot\underset{\sim}{\nabla})(\underset{\sim}{r}\cdot\underset{\sim}{\nabla}-2)(\underset{\sim}{r}\cdot\underset{\sim}{\nabla}-4)[a_4 w_{1c}^{(n-3)} + b_4 w_{1c}^{(n-4)}]/3!$$

$$(34) \quad I_{n-1} = (\underset{\sim}{r}\cdot\underset{\sim}{\nabla})(\underset{\sim}{r}\cdot\underset{\sim}{\nabla}-2)(\underset{\sim}{r}\cdot\underset{\sim}{\nabla}-4)\cdots\cdots[\underset{\sim}{r}\cdot\underset{\sim}{\nabla}-2(n-4)] \times$$

$$\times \; [3\, w_{1c}^{(3)} + 4w_{1c}^{(2)}] \; /(n-3)!$$

$$(35) \quad I_{n} = (\underset{\sim}{r}\cdot\underset{\sim}{\nabla})(\underset{\sim}{r}.\underset{\sim}{\nabla}-2)(\underset{\sim}{r}\cdot\underset{\sim}{\nabla}-4)\cdots\cdots\cdots[\underset{\sim}{r}\cdot\underset{\sim}{\nabla}-2(n-4)] \times$$

$$\times [\; w_{1c}^{(2)} + w_{1c}^{(1)}] \quad /(n-2)!$$

In obtaining the recurrence formulas (28) and (29), we used the following indentity:

$$(36) \quad (\nabla^2+k^2)[(\underset{\sim}{r}\cdot\underset{\sim}{\nabla})(\underset{\sim}{r}\cdot\underset{\sim}{\nabla}-2)(\underset{\sim}{r}\cdot\underset{\sim}{\nabla}-4)\cdots\cdots(\underset{\sim}{r}\cdot\underset{\sim}{\nabla}-2m)\; w_{ic}^{(n)}]$$

$$= -\; 2(m+1)k^2(\underset{\sim}{r}\cdot\underset{\sim}{\nabla})(\underset{\sim}{r}\cdot\underset{\sim}{\nabla}-2)\cdots\cdots[\underset{\sim}{r}\cdot\underset{\sim}{\nabla}-2(m-1)]\; w_{ic}^{(n)}$$

where $m = 0,1,2,3,\ldots\ldots\ldots\ldots, \; i = 1,2.$

It is interesting to point out that the first order particular solutions presented here are the same as those which were obtained by Thau and Pao. While, the second order solutions are different from the solutions obtained by Thau and Pao. In fact, we can easily find three different forms of the perturbation solutions for the second order particular solutions, viz.,

$$(37) \quad w_{1p}^{(2)} = -\; \underset{\sim}{r}\cdot\underset{\sim}{\nabla}[w_1^{(o)} - w_{1c}^{(1)}] \;-\; \tfrac{1}{2}\, k^2 r^2 \; w_1^{(o)}$$

$$(38) \quad w_{2p}^{(2)} = -\; \underset{\sim}{r}\cdot\underset{\sim}{\nabla}[w_2^{(o)} + w_{2c}^{(1)}] \;-\; \tfrac{1}{2}\, k^2 r^2 \; w_2^{(o)}$$

(39) $$w_{1p}^{(2)} = \underset{\sim}{r}\cdot\underset{\sim}{\nabla}\ [w_1^{(1)} - w_1^{(o)}] + \tfrac{1}{2}\ k^2 r^2\ w_1^{(o)}$$

(40) $$w_{2p}^{(2)} = \underset{\sim}{r}\cdot\underset{\sim}{\nabla}\ [w_2^{(1)} + w_2^{(o)}] + \tfrac{1}{2}\ k^2 r^2\ w_2^{(o)}$$

(41) $$w_{1p}^{(2)} = \underset{\sim}{r}\cdot\underset{\sim}{\nabla}\ [w_{1c}^{(1)} + w_{1p}^{(1)}/2]$$

(42) $$w_{2p}^{(2)} = -\ \underset{\sim}{r}\cdot\underset{\sim}{\nabla}[w_{2c}^{(1)} + w_{2p}^{(1)}/2]$$

Equations (37) and (38) are the same as those of the Thau-Pao solutions. Equations (39) and (40) are the same as the solutions presented in equations (24) and (25). The reason we obtain different forms of particular solutions is due to the fact that the following expressions exist to generate these particular solutions:

(43) $$(\nabla^2 + k^2)\,[\underset{\sim}{r}\cdot\underset{\sim}{\nabla}w_{ip}^{(1)} + k^2 r^2\ w_i^{(o)}] = 0$$

$$i = 1,\ 2.$$

However, although we can find the different forms for the particular solutions, after satisfying the prescribed boundary conditions for some specific problems, the complete solutions $w_i^{(2)} = w_{ic}^{(2)} + w_{ip}^{(2)}$ $(i = 1,2.)$ would be the same no matter which forms of equations (37) to (42) are chosen. Similarly different expression of the particular solutions for higher orders (n>2) also can be found. Therefore, here we shall designate these solutions as "Pseudo-particular solutions" instead of "particular solutions".

As for the perturbation parameter ε, equation (9) can be rewritten as

$$\varepsilon = \frac{[1 - (v_1/v_2)^2]}{2[1 + (v_1/v_2)^2]} \tag{44}$$

In an elastic solid, as Thau and Pao pointed out, the numerical value of the parameter ε is limited between 1/6 and 1/2. If the problem of SH-wave in two different welded media, or acoustic waves in two ideal fluids in contact, is considered, the numerical value of ε is 1/2, for the extreme case when $v_1 \longrightarrow 0$ or $v_2 \longrightarrow \infty$. However, there is no limit on the lower bound numerically. The smaller is the contrast between v_1 and v_2, the smaller is the numerical value of ε. For example, for the case of two shear wave velocities v_1=3.7 km/sec, v_2=4.5 km/sec, ε is 0.0966. The first few order solutions are good enough for a small quantity of ε. Therefore, obtaining the general recurrence formula, no matter how tedious the process may be, these higher order perturbation solutions promise to solve some long standing elastodynamic problems which otherwise are analytically untractable.

APPLICATION OF THE RMS-VALUE PERTURBATION METHOD TO SH-WAVES IN A SLOPING INTERFACED HALF-SPACE

The geometry of the problem in question is an elastic wedge overlying an elastic bottom as shown in Figure 1. Both media are assumed to be homogeneous and istropic solid. The inclined interface is assumed to be perfectly welded. Restricting a line source of the SH-wave type located in the wedge, we can consider the problem to be two-dimensional so that the particle motion of SH-waves is confined to the direction of z only, and the wave propagation direction is in the (r,θ) of the polar coordinate system. The overlying wedge medium (μ_1,ρ_1) is bounded by $\theta=0$ and $\theta=\alpha$; the under-lain bottom medium (μ_2,ρ_2), is bounded by $\theta=\alpha$ and $\theta=\pi$, where μ_i and ρ_i, i=1,2 are the rigidities and densities of the overlying and bottom media respectively. A line source of SH-wave is located at the (r_o,θ_o) in the overlying wedge. The displacements $W_i(r,\theta,t)$, i=1.2. satisfy the wave equations in the overlying medium and bottom medium, respectively

$$(45) \qquad \nabla^2 W_1 - \frac{1}{\beta_1^2}\frac{\partial^2 W_1}{\partial t^2} = -\frac{2\pi}{r}\,\delta(r-r_o)\,\delta(\theta-\theta_o)\,\delta(t-0^+)$$

$$(46) \qquad \nabla^2 W_2 - \frac{1}{\beta_2^2}\frac{\partial^2 W_2}{\partial t^2} = 0$$

where

$$(47) \qquad \beta_i = \sqrt{(\mu_i/\rho_i)} \quad , \qquad i = 1,2, \quad \beta_1 < \beta_2 \; .$$

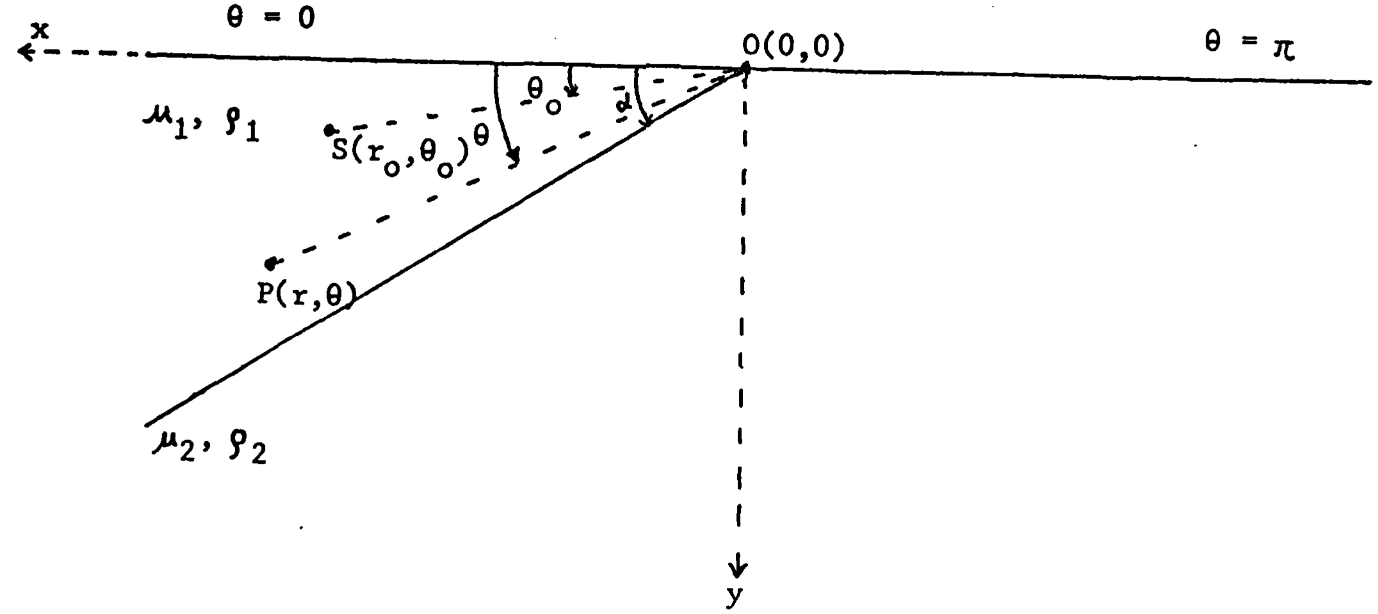

Figure 1. Geometry of the Problem of SH-waves in a Sloping Interfaced Half-Space.

The conditions to be satisfied in the traction free boundaries are sufficiently described by the vanishing of the normal components of the stress. At the perfectly welded interface between two dissimilar media, there must be continuity of the displacements and stresses.

By taking Laplace transforms of the equations (45) and (46) with respect to t, the new transformed equations are

$$(48) \qquad (\nabla^2 - h_1^2)\ w_1(r,\theta,p) = -\frac{2\pi}{r}\ \delta(r-r_o)\,\delta(\theta-\theta_o)$$

$$(49) \qquad (\nabla^2 - h_2^2)\ w_2(r,\theta,p) = 0$$

where

$$(50) \qquad w_i(r,\theta,p) = \mathcal{L}[W_i(r,\theta,t)] = \int_0^\infty W_i(r,\theta,t)\ \exp(-pt)\ dt$$

and $h_i = \rho/\beta_i \qquad i = 1,2$

Using the present RMS perturbation method, we obtained a third-order formal perturbation solutions as

$$(51) \qquad w_i = w_i^{(o)} + \varepsilon w_i^{(1)} + \varepsilon^2\ w_i^{(2)} + \varepsilon^3\ w_i^{(3)}$$

where

$$(52) \qquad \varepsilon = \frac{h_1^2 - h_2^2}{2\ (h_1^2 + h_2^2\ )} = \frac{\beta_2^2 - \beta_1^2}{2\ (\beta_1^2 + \beta_2^2\ )}$$

The Zero-order displacement components are:

$$(53) \qquad w_1^{(o)} = \frac{2\,i}{\pi^2} \int_{-\infty}^{\infty} \left[\begin{array}{l} \mathrm{ch}\, s(\pi-\theta_>+\theta_<) - \\ -\, \mathrm{sh}\, s(\pi-\theta_o)\, \mathrm{sh}\, s\theta + \\ +\, A_s^{(o)}\, \mathrm{ch}\, s\theta \end{array} \right] K_{is}(hr_o) K_{is}(hr)\, ds$$

$$(54) \qquad w_2^{(o)} = \frac{2\,i}{\pi^2} \int_{-\infty}^{\infty} E_s^{(o)}\, \mathrm{ch}\, s(\pi-\theta)\, K_{is}(hr_o) K_{is}(hr)\, ds$$

with

$$(55) \qquad A_s^{(o)} = \frac{\left[\begin{array}{l} -\, \mu_2\, \mathrm{sh}\, s(\pi-\alpha) [\mathrm{ch}\, s(\pi-\alpha+\theta_o) - \mathrm{sh}\, s(\pi-\theta_o)\, \mathrm{sh}\, s\alpha] + \\ +\, \mu_1\, \mathrm{ch}(\pi-\alpha) [\mathrm{sh}\, s(\pi-\alpha+\theta_o) + \mathrm{sh}\, s(\pi-\theta_o)\, \mathrm{ch}\, s\alpha] \end{array} \right]}{[\, \mu_2\, \mathrm{sh}\, s(\pi-\alpha)\, \mathrm{ch}\, s\alpha + \mu_1\, \mathrm{ch}\, s(\pi-\alpha)\, \mathrm{sh}\, s\alpha \,]}$$

$$(56) \qquad E_s^{(o)} = \frac{\mu_1 \left[\begin{array}{l} \mathrm{ch}\, s\alpha\, [\mathrm{sh}\, s(\pi-\alpha+\theta_o) + \mathrm{sh}\, s(\pi-\theta_o)\, \mathrm{ch}\, s\alpha] + \\ +\, \mathrm{sh}\, s\alpha\, [\mathrm{ch}\, s(\pi-\alpha+\theta_o) - \mathrm{sh}\, s(\pi-\theta_o)\, \mathrm{sh}\, s\alpha] \end{array} \right]}{[\, \mu_2\, \mathrm{sh}\, s(\pi-\alpha)\, \mathrm{ch}\, s\alpha + \mu_1\, \mathrm{ch}\, s(\pi-\alpha)\, \mathrm{sh}\, s\alpha \,]}$$

The First-order displacement components are:

$$(57) \qquad w_1^{(1)} = \frac{2\,i}{\pi^2} \int_{-\infty}^{\infty} \left[\begin{array}{l} \mathrm{ch}\, s(\pi-\theta_>+\theta_<) - \\ -\, \mathrm{sh}\, s(\pi-\theta_o)\, \mathrm{sh}\, s\theta + \\ +\, A_s^{(o)}\, \mathrm{ch}\, s\theta \end{array} \right] \times$$

$$\times \left(\begin{array}{l} \tfrac{1}{2}\, hr_o\, [K_{is+1}(hr_o) + K_{is-1}(hr)]\, K_{is}(kr) \\ \qquad -\, K_{is}(hr_o)\, r\, \dfrac{\partial K_{is}(hr)}{\partial r} \end{array} \right) ds$$

$$(58) \qquad w_2^{(1)} = \frac{2\,i}{\pi^2} \int_{-\infty}^{\infty} E_s^{(1)} \operatorname{ch} s(\pi-\theta)\; K_{is}(hr)\; ds \;+$$

$$+ \frac{2\,i}{\pi^2} \int_{-\infty}^{\infty} E_s^{(o)} \operatorname{ch} s(\pi-\theta)\; K_{is}(hr_o) \left[- r \frac{\partial K_{is}(hr)}{\partial r} \right]$$

with

$$(59) \qquad E_s^{(1)} = \tfrac{1}{2}\, hr_o \left[K_{is+1}(hr_o) + K_{is-1}(hr_o) \right] \; E_s^{(o)}$$

The Second-order displacement components are :

$$(60) \qquad w_1^{(2)} = \frac{2\,i}{\pi^2} \int_{-\infty}^{\infty} \begin{bmatrix} \operatorname{ch} s(\pi-\theta_> + \theta_<) \; - \\ - \operatorname{sh} s(\pi-\theta_o)\; \operatorname{sh} s\theta \; + \\ + \; A_s^{(o)} \operatorname{ch} s\theta \end{bmatrix} \times$$

$$\times \begin{bmatrix} \dfrac{h^2}{2}\, r\, r_o \left[K_{is-1}(hr_o) K_{is+1}(hr) + K_{is+1}(hr_o) K_{is-1}(hr) \right] \; + \\ + \; (hr/2)^2 K_{is}(hr_o) \left[K_{is+2}(hr) + K_{is-2}(hr) \right] \; + \\ + \; \dfrac{h^2\, r_o^2}{2 \cdot 2!} \left[K_{is+2}(hr_o) + K_{is-2}(hr_o) \right] K_{is}(hr) \end{bmatrix} ds$$

$$(61) \qquad w_2^{(2)} = w_{2c}^{(2)} + w_{2p}^{(2)}$$

$$(62) \qquad w_{2c}^{(2)} = \frac{2\,i}{\pi^2} \int_{-\infty}^{\infty} E_s^{(2)} \operatorname{ch} s(\pi-\theta)\; K_{is}(hr)\; ds$$

with

$$E_s^{(2)} = \{(\frac{hr_o}{2})^2[K_{is+2}(hr_o) + K_{is-2}(hr_o)] - (is)^2 K_{is}(hr_o)\} E_s^{(o)} \tag{63}$$

The Third-order displacement components are:

$$w_1^{(3)} = \frac{2i}{\pi^2}\int_{-\infty}^{\infty} \begin{bmatrix} \text{ch } s(\pi-\theta_> + \theta_<) - \\ - \text{sh } s(\pi-\theta_o) \text{ sh } s\theta + \\ + A_s^{(o)} \text{ ch } s\theta \end{bmatrix} \times \tag{64}$$

$$\times \begin{bmatrix} \frac{(hr_o)^3}{2\cdot 3!}[K_{is+3}(hr_o) + K_{is-3}(hr_o)] \; K_{is}(hr) + \\ + \frac{h^3}{2\cdot 3!} K_{is}(hr_o) \; [r^3 K_{is+3}(hr) + r^3 K_{is-3}(hr)] + \\ + \frac{h^3 r_o^2 r}{2\cdot 2!} [K_{is-2}(hr_o)K_{is+1}(hr) + K_{is+2}(hr)K_{is-1}(hr)] + \\ + \frac{h^3 r_o r^2}{2\cdot 2!} [K_{is-1}(hr_o)K_{is+2}(hr) + K_{is+2}(hr_o)K_{is-1}(kr)] \end{bmatrix} ds$$

$$w_2^{(3)} = w_{2c}^{(3)} + w_{2p}^{(3)} \tag{65}$$

$$w_{3c}^{(3)} = \frac{2\,i}{\pi^2}\int_{-\infty}^{\infty} E_s^{(3)} \text{ ch } s(\pi-\theta) \; K_{is}(hr) \; ds \tag{66}$$

$$w_{3p}^{(3)} = \frac{2\,i}{\pi^2}\int_{-\infty}^{\infty} E_s^{(o)} \text{ ch } s(\pi-\theta) \; \{J_1 + J_2 + J_3 + J_4\} \; ds \tag{67}$$

with

$$
(68) \qquad E_s^{(3)} = \left[\begin{array}{l} \frac{h^3 r_o^3}{12} \; [K_{is+3}(hr_o) + K_{is-3}(hr_o)] \; - \\ - \; (\frac{hr_o}{2})^2 \; [K_{is+2}(hr_o) - K_{is-2}(hr_o)] + \\ + \; \frac{(is)^2}{6} \; (hr_o) [\; K_{is+1}(hr_o) + K_{is-1}(hr_o)] - \\ - \; (is)^2 \; K_{is}(hr_o) \end{array} \right] E_s^{(o)}
$$

$$
(69) \qquad J_1 = \tfrac{1}{4} K_{is}(hr_o) \frac{(hr)^3}{3!} [\; K_{is+3}(hr) + K_{is-3}(hr)]
$$

$$
(70) \qquad J_2 = \frac{h^3 r_o r^2}{4} [K_{is-1}(hr\;) K_{is+2}(hr) + K_{is+1}(hr\;) K_{is-2}(hr)]
$$

$$
(71) \qquad J_3 = \frac{h^3 r_o^2 r}{4} [K_{is+2}(hr_o) K_{is-1}(hr) + K_{is-2}(hr_o) K_{is+1}(hr)]
$$

$$
(72) \qquad J_4 = (\frac{hr_o}{2})^2 [K_{is+2}(hr_o) - K_{is-2}(hr_o)] \; - \\ - \frac{(is)^2}{6} (hr_o) \; [K_{is+1}(hr_o) + K_{is-1}(hr_o)] \; + \\ + \; (is)^2 K_{is}(hr_o)
$$

FUTURE WORK

The formulation of the higher order perturbation method, as an example for solving one of the long standing wave propagation problems, i.e. the wedge problem, is completed. The follow-up will be a numerical evaluation of the formal solutions to the problem of the SH-wave propagation in a sloping interfaced half-space.

REFERENCES

Pao, Y.H. and S.A. Thau, "A Perturbation Method for Boundary Value Problems in Dynamic Elasticity, Part VI" Quart. Appl. Math. 28, 191 (1970).

Thau, S.A. and Y.H. Pao, "A Perturbation Method for Boundary Value Problems in Dynamic Elasticity", Quart. J. Appl. Math., Vol.25, 1967, pp.243-260.

III. FINITE ELEMENT SOLUTION TO TRANSIENT PROBLEMS OF A FINITE CYLINDRICAL CAVITY SOURCE

ABSTRACT

This paper presents the numerical solutions to the problem of the transient seismic response of an elastic whole-space, an elastic half-space, and a layered elastic half-space due to a finite cylindrical cavity source by means of the finite element method, based on the principle of Virtual Work.

Synthetic seismograms of both the radial and vertical displacements of the transient response of Model I - a whole-space, Model II - a half-space, and Model III - a layer half-space for a finite cylindrical cavity source embedded in the medium at several important observation points are obtained. Some of interesting features of the transient response are as follows: (1) for the observation points inside the medium, the reflected waves from the surface boundary of the half-space does not seem to have significant effect on the amplitude of the wave for the velocity of the medium assumed. For vertical displacements, the arrival of the reflected wave is identified as a step in time. For radial displacements, the arrival of the reflected wave is not easily identified, (2) the amplitudes of both vertical and radial displacements at the observation point on the surface of the half-space are much larger than these at the corresponding observation point in the medium of the whole-space, (3) the wave forms of the transient response strongly depend on the dimensions of the finite cylindrical cavity, i.e. the radius and length of the cavity, (4) the P wave traveling periodically from the top rim to the bottom rim of the cavity along the vertical interface of the cylindrical cavity and the P wave periodically oscillating in the bottom (or the top) face of the cavity with a motion of the Bessel function order zero type, and traveling through the vertical face of the cavity, to the top (or the bottom) face of the cylindrical cavity also with a motion of the Bessel function order zero type are dominant in all three models, (5) there is no vertical displacement at any point along the middle plane, whcih are symmetrical with respect to the two end faces of the cylindrical cavity, in Model I - a whole-space, (6) for Model III - a layer half-space, the long period wave is predominant, traveling periodically along the verical face of the drilling hole cavity between the rim of the contact at the layer-interface and the top rim of the cylindrical cavity, (7) the weathering (low velocity) layer acts as a low pass filter, all the high frequence arrivals are filtered out in the seismograms at the observation points located in the weathering layer, (8) the shape

of the input forcing function is well preserved on each seismogram of the vertical displacement but not on the radial displacement, (9) the beat phenomenon is observed on the radial displacement of these observation points located in the upper region of the cavity source, (10) the amplitudes of both the radial and vertical displacements are extremely large at those observation points close to the cavity in the filled drilling hole, but are attenuated rapidly as the observation moves away from the cavity, and (11) shear waves can be generated from a finite length cavity source with only normal stresses applied on the surfaces of the cavity. The arrival of the shear wave are clearly identifiable at these observation points in the region along the diagonal line of the cylindrical cavity.

1 INTRODUCTION

For the transient problem of a layered medium due to a finite cylindrical source, we must resort to numerical solutions, such as the finite element method, which provides a mean of solving a class of transient problems of elastic wave scattering and diffraction. For this reason, we have developed the finite element method to solve transient problems of elastic wave propagation in a layered medium due to a finite cylindrical source. The formulation for the finite element method based on the principle of virtual work is briefly outlined in sections 2 through 4. It should be pointed out that all the inherent logarithmic singularities are being removed analytically in the formulation. Therefore, the errors due to the singularities will not be introduced into the numerical calculation. The applicability of the method to solve practical seismic problems has also been well demonstrated through solving a series of the transient problems in an elastic half-space and a layered half-space due to a finite cylindrical cavity source as shown in section 5. The numerical results and interpretation are presented in section 6. Conclusions are presented in section 7.

2. DEVELOPMENT OF FINITE ELEMENT DISCRETIZATION BASED ON VIRTUAL DISPLACEMENT FOR SOLVING TRANSIENT PROBLEM OF A FINITE CYLINDRICAL CAVITY COMPRESSIONAL SOURCE

The Principle of Virtual Work states that for the equilibrium of an elastic, isotropic and homogeneous body, the total internal virtual work is equal to the total external virtual work for any compatible and small virtual displacements imposed onto that body (Fung, 1965).

$$\int_V \tau \delta \varepsilon^t \, dv = \int_V f^b \delta U^t dv + \int_S f^s \delta U^t ds \qquad 1)$$

For an axial-symmetrical geometrical configuration with a dynamic source excitation, we adopt the cylindrical coordinates system (r,θ,z). The quantities in 1) assume the following:

(a) The azimuthal-independent displacement field U^t and the corresponding strain ε^t are

$$U^t = [\ u_r,\ 0,\ u_z]$$

$$\varepsilon^t = [\ \varepsilon_{rr},\ \varepsilon_{\theta\theta},\ \varepsilon_{zz},\ 0,\ 0,\ \varepsilon_{rz}] \qquad 2)$$

(b) The strain-displacement and the corresponding stress, and the stress-strain relations are

$$\varepsilon_{ij} = (\ u_{i,j} + u_{j,i})/2$$

$$\tau^t = [\ \tau_{rr},\ \tau_{\theta\theta},\ \tau_{zz},\ 0,\ 0,\ \tau_{rz}]$$

$$\tau_{ij} = [\ \lambda\varepsilon_{kk}\delta_{ij} + 2\mu\varepsilon_{ij}] \qquad 3)$$

(c) f^s and f^b are the surface traction and body force, respectively.

1) may be converted to a system of ordinary differential equations by the following arguments. As the volume V may be divided into n subvolumes, or finite elements V_m, and the surface S, similarly divided into n subsurfaces S_m, m = 1,2,3,.........N, we then have

$$V = \lim_{N\to\infty} \sum_{m=1}^{N} V_m \quad , \qquad S = \lim_{N\to\infty} \sum_{m=1}^{N} S_m \qquad 4)$$

In each subvolume (or subregion) V_m, instead of determining the displacement field everywhere in V_m, we find the displacement vectors at only a discrete finite number of points in V_m, viz; nodal points, under the action of the external forces. The displacement vector at the points other than these nodal points may be determined from the displacement vectors at the nodal points through some interpolation functions. Within each element, the displacement field U^m may be expressed in the form

$$U^m = N^m \Psi^m \qquad 5)$$

and the strain-displacement relation is

$$\varepsilon^m = B^m \Psi^m \qquad 6)$$

where

N^m = a known matrix of the spatial interpolation function for the m^{th} element,

Ψ^m = the nodal displacement vector of the m^{th} element,

B^m = the matrix of the strain-displacement relations of the m^{th} element.

After applying equations 4), 5) and 6), equation 1) becomes

$$\sum_{m=1}^{N} (M^m \ddot{\Psi}^m + K^m + T^m) = 0 \qquad 7)$$

with

$$M^m = \int_{v^m} \rho (N^m)^t N^m \, dv^m \qquad 8)$$

$$K^m = \int_{v^m} (B^m)^t D^m B^m \, dv^m \qquad 9)$$

$$T^m = \int_{s^m} (N^m)^t \, (f^s)^t \, ds^m \qquad 10)$$

where M^m, K^m, D^m, T^m are the mass matrix, stiffness matrix, matrix of constitutive relation, and vector matrix of tractions applying on the surface S, respectively.

3. INTEGRATION OF THE INTERPOLATION FUNCTION N^m ON AN AXIAL-SYMMETRICAL TRIANGULAR RING ELEMENT

For the present transient problem, which possesses an axial-symmetrical geometry, we may adopt 'solid toroidal elements' for the spatial domain. Since the whole formulation is independent of θ, the integrals for the volume and surface integrations in the equations of virtual work reduce to these of plane surface integrals and line integrals.

Since the displacement field is linear, we position the element arbitrarily in the r-z plane. Constructing the element stiffness matrix, even for the simplest case of a linear displacement field, we must take into account the dependence of the strain-displacement equations on the inverse of the radius, particularly, the singularities along the axis of symmetry. Applying the proper interpolation function for space, and using the pertinent strain-displacement relationship, we obtain the kernel stiffness matrix as follows:

$$\begin{bmatrix} (1-\nu)I_4 & I_2 & (1-\nu)I_5 & 0 & 0 & \nu I_2 \\ I_2 & 2I_1 & I_3 & 0 & 0 & 2\mu I_1 \\ (1-\nu)I_5 & I_3 & (1-\nu)I_6+(1-2\nu)I_1/2 & 0 & (1-2\nu)I_1/2 & \mu I_3 \\ 0 & 0 & 0 & 0 & 0 & 0 \\ 0 & 0 & (1-2\nu)I_1/2 & 0 & (1-2\nu)I_1/2 & 0 \\ \nu I_2 & 2\mu I_1 & \mu I_3 & 0 & 0 & (1-\nu)I_1 \end{bmatrix} \tag{11}$$

in which

$$I_1 = \iint r\,dr\,dz \qquad I_4 = \iint dr\,dz/r$$

$$I_2 = \iint dr\,dz \qquad I_5 = \iint z\,dr\,dz/r$$

$$I_3 = \iint z\,dr\,dz \qquad I_6 = \iint z^2 dr\,dz/r$$

The spatial integrations I_1 through I_6 have carried out analytically so that the inherent logarithmic singularities are being removed. Otherwise, the errors due to these singularities will be introduced into the numerical calculations. The terms I_1, I_2, and I_3 yield

$$I_1 = (1/6)(r_1+r_2+r_3)[r_1(z_2-z_3)+r_2(z_3-z_1)+r_3(z_1-z_2)]$$

$$I_2 = (1/2)[r_1(z_2-z_3)+r_2(z_3-z_1)+r_3(z_1-z_2)]$$

$$I_3 = (1/6)(z_1+z_2+z_3)[r_1(z_2-z_3)+r_2(z_3-z_1)+r_3(z_1-z_2)]$$

12)

The terms I_4, I_5, and I_6 involve the variable r in the denominator of the integrand and result in considerably complicated expressions.

(i) In the case $r_1 \neq r_2 \neq r_3 \neq r_1 \neq 0$

$$I_4 = X_{12} + X_{23} + X_{31}$$

$$I_5 = Y_{12} + Y_{23} + Y_{31}$$

$$I_6 = Z_{12} + Z_{23} + Z_{31}$$

where, for i,j=1,2,3

$$X_{ij} = \frac{(r_i z_j - r_j z_i)}{r_i - r_j} \ln \frac{r_i}{r_j}$$

$$Y_{ij} = -\frac{(z_i - z_j)}{4(r_i - r_j)} [z_i(3r_j - r_i) - z_j(3r_i - r_j) \cdot$$

$$(1/2)\left(\frac{r_i z_j - r_j z_i}{r_i - r_j}\right)^2 \ln \frac{r_i}{r_j}]$$

$$Z_{ij} = (1/3)\left(\frac{r_i z_j - r_j z_i}{r_i - r_j}\right)^3 \ln \frac{r_i}{r_j} + \frac{(z_i - z_j)}{18(r_i - r_j)^2} \cdot$$

$$[z_j^2(11r_i^2 - 7r_i r_j + 2r_j^2) + 2z_i z_j(2.5r_i^2 - 11r_i r_j +$$

$$2.5r_j^2) + z_i^2(11r_j^2 - 7r_i r_j + 2r_i^2)] \qquad 13)$$

Special problems arise, when the joints are located on the axis of symmetry, as the terms with $\ln(r_i/r_j)$ and (r_i-r_j) in the denominator become infinite. In this case, we evaluate the integrals by L'Hospital's rule.

(ii) In the case $r_i \neq r_j \neq r_k \neq r_i$, and $r_i=0$

$$I_4 = [\frac{r_j(z_k-z_i)+r_k(z_i-z_j)}{r_j-r_k}] \ln\frac{r_j}{r_k}$$

$$I_5 = Y_{jk} + (1/4)[(z_i-z_j)(3z_i+z_j)+(z_k-z_i)(3z_i+z_k)] - (1/2)z_i^2 \ln\frac{r_j}{r_k}$$

$$I_6 = Z_{jk} + \frac{z_k-z_i}{18}(11z_i^2+5z_iz_k+2z_k^2) + \frac{z_i-z_j}{18}(11z_i^2+5z_iz_j+2z_j^2) - (1/3)z_i^3 \ln\frac{r_j}{r_k}$$

14)

(iii) In the case $r_i=r_k$, and $r_j \neq r_i \neq 0$

$$I_4 = [(\frac{r_j}{r_j-r_k}) \ln\frac{r_j}{r_k} - 1] (z_k-z_i)$$

$$I_5 = \frac{z_k - z_i}{2(r_i - r_k)^3}(r_j{}^2 z_k + r_j{}^2 z_i - 2r_j r_k z_j) \ \ln \frac{r_j}{r_k}$$

$$- \frac{z_k - z_i}{4(r_j - r_k)^2}[2z_j(r_k + r_j) - (3r_j - r_k)(z_k + z_i)]$$

$$I_6 = \frac{(z_k - z_i)r_j}{3(r_j - r_k)^3}[r_j{}^2(z_k{}^2 + z_i z_k + z_i{}^2) + 3r_k z_j(r_k z_j - r_j z_k -$$

$$r_j z_i)] \ \ln \frac{r_j}{r_k} + \frac{(z_k - z_i)}{18(r_j - r_k)^2}[z_j{}^2(3r_j{}^2 - 15r_j r_k -$$

$$6r_k{}^2) + z_j(z_k + z_i)(6r_j{}^2 + 15r_j r_k - 3r_k{}^2) - (z_k{}^2 + z_i{}^2 +$$

$$z_i z_k)(11r_j{}^2 - 7r_j r_k + 2r_k{}^2)] \qquad 15)$$

(iv) In the case $r_i = r_k \neq r_j$, $r_i = r_k \neq 0$, and $r_j = 0$

$$I_4 = -(z_k - z_i)$$

$$I_5 = -\frac{z_k - z_i}{4}(2z_j + z_i + z_k) \qquad 16)$$

$$I_6 = -\frac{z_k - z_i}{18}(6z_j{}^2 + 2z_k{}^2 + 2z_i{}^2 + 3z_i z_j + 3z_j z_k + 2z_i z_k)$$

(v) In the case when $r_i=r_j=0$, and $r_k=0$, it can be shown that the terms containing I_4, I_5, and I_6 do not appear in the stiffness matrix that the displacements $u_i=u_j=0$. All these integrals can be used as a basis for deriving the similar integrals of nonlinear interpolation functions.

4. TIME INTEGRATION SCHEME

After careful and critical tests and evaluation of various three-dimensional finite element formulations, it was found that the combination of lumped mass matrix representation and explicit central-differences time integration of three-dimensional finite element formulation appears to be the best in solving transient problems of elastic wave propagation. An important advantage of using a lumped mass matrix is that the matrix is diagonal, and as it will be seen later, the numerical operations for obtaining the solution to the dynamic equation of equilibrium are simplified.

The scheme of time integration for the dynamic structural problem with the equation of motion

$$M\ddot{U} + KU = F \tag{17}$$

can be considered as a subclass of the explicit methods of the form

$$U_{n+1} + \sum_{j=0}^{N} (a_j U_{n-j} + b_j K U_{n-j}) = 0 \qquad 18)$$

with $N=2$, $a_0=-2$, $a_1=1$, $b_0=\Delta t^2$, $b_1=0$.

Therefore, we obtain

$$U(t+\Delta t) = U(t) + \dot{U}(t)\Delta t$$

$$\dot{U}(t+\Delta t) = \dot{U}(t) + M^{-1}KU(t+\Delta t)\Delta t \qquad 19)$$

which is the central differences scheme. Krieg(1970) and Baylor et al(1974) have proved that the central differences scheme has the largest stability region.

5. TRANSIENT PROBLEM DUE TO A FINITE LENGTH CYLINDRICAL CAVITY IN AN ELASTIC HALF-SPACE AND LAYERED HALF-SPACE

In this dissertation, with a view to simulate conditions in the neighborhood of a drilling hole, the source chosen is a cylindrical cavity of length $\ell = 6$ feet, and radius $a = 0.5$ feet, centered at the origin of coordinate and embedded in an infinite medium, Figure 1.

For comparison, we simulate the second model with the half-space, the surface of the half-space is located at 25 feet above the top end of the cylindrical cavity, as shown in Figure 2. The half-space medium is characterized by the elastic constants E, σ, ρ as medium 2 given in Table 1.

In seismic prospecting, a layer occurs at the surface of the earth which is unconsolidated, and often heterogeneous with low wave velocity, so called "weathering layer". The thickness of the weathering layer may vary from almost zero to several hundred feet; however, the most common thickness is from about 25 feet to 100 feet. For our computation, we simulate the weathering layer with a thickness of 20 feet. The cylindrical cavity is embedded 5 feet below the weathering layer, including the case of a filled drilling hole. The geometrical setting is shown in Figure 3. The medium of the weathering layer and the filled drilling hole are characterized by the elastic constants E_1, σ_1, ρ_1 and E_3, σ_3, ρ_3, respectively, as given in Table 1. The finite element meshes are formed according to the dimensions as described above and shown in Figure 4,5 Model I has 687 nodal points and 1268

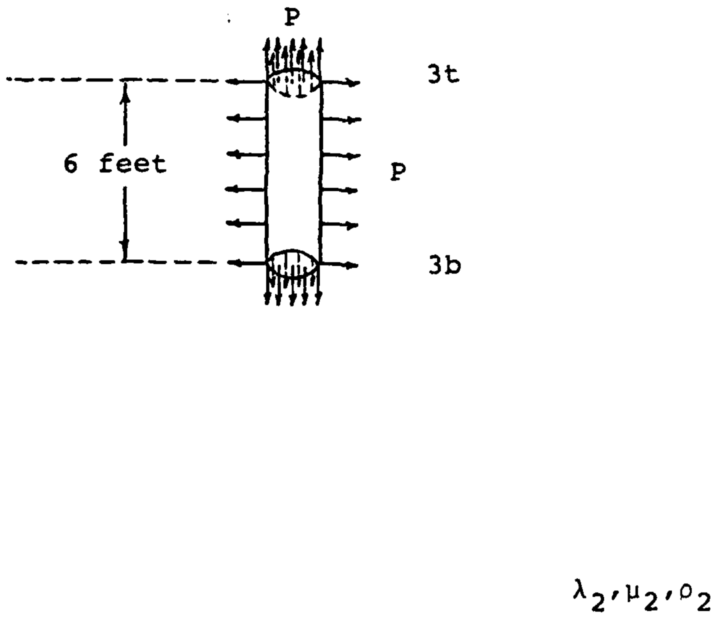

Figure 1. The Geometry of Model I - the Whole-space.

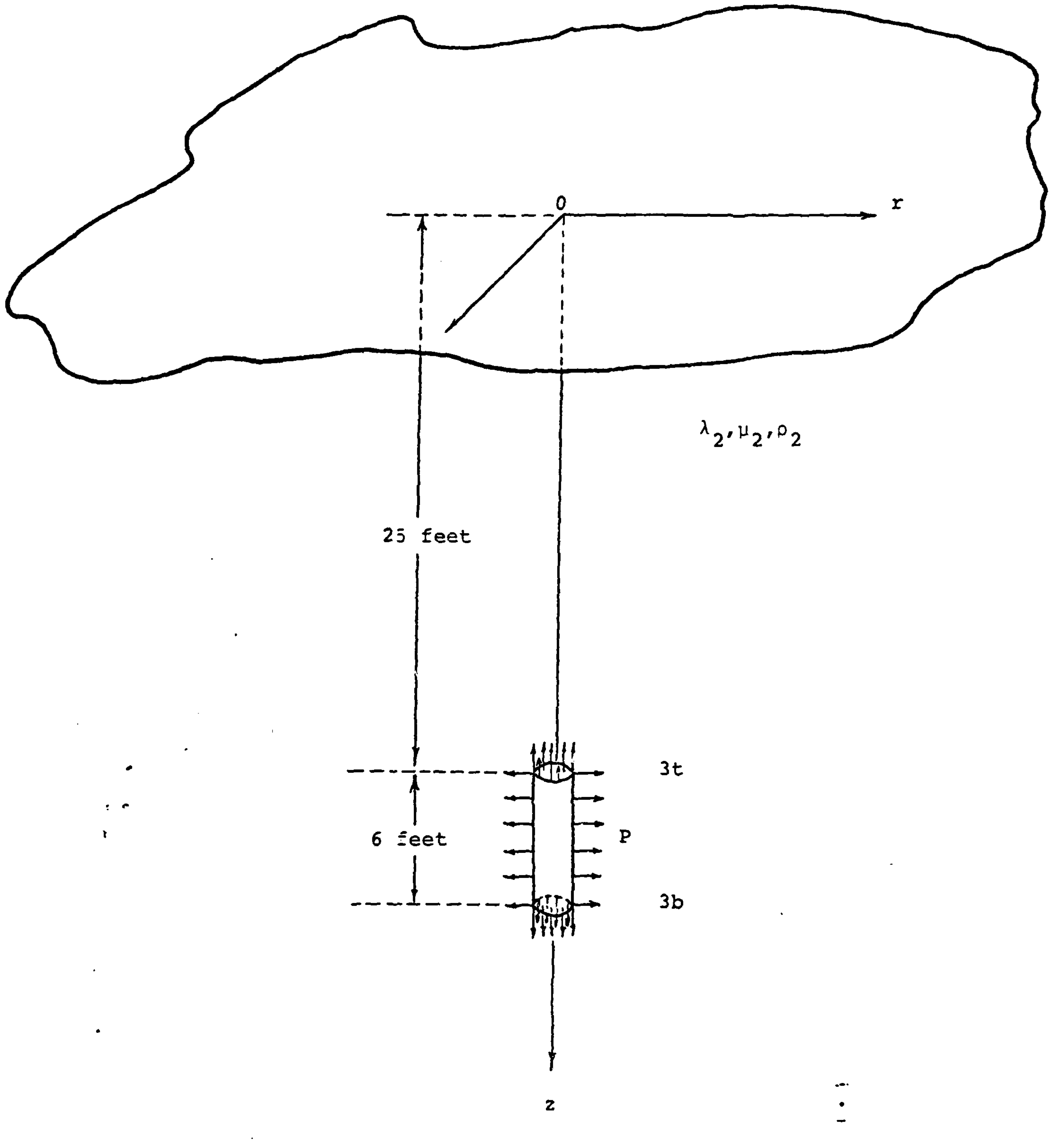

Figure 2. The Geometry of Model II - the Half-space.

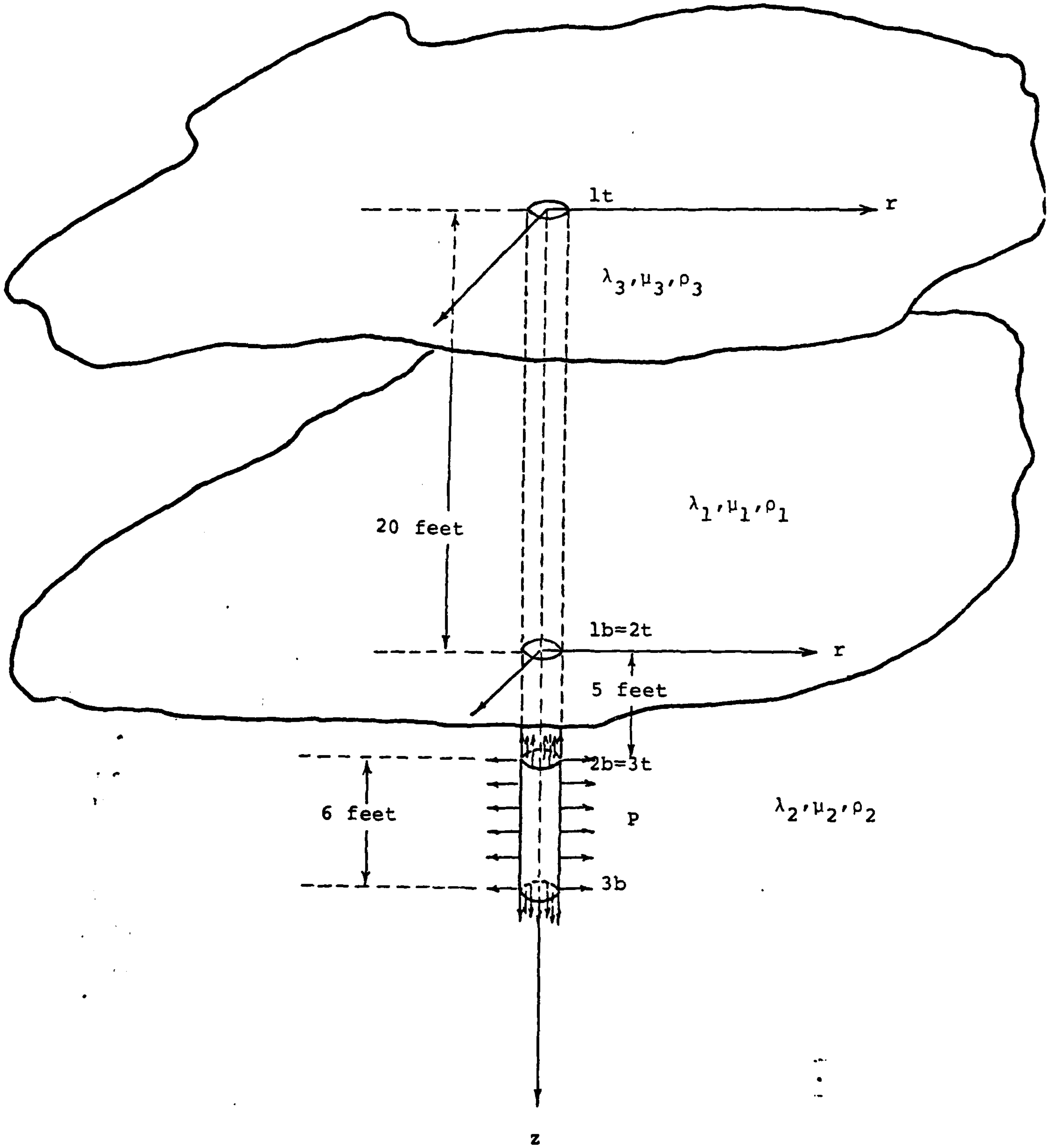

Figure 3. The Geometry of Model III - the Layered Half-space.

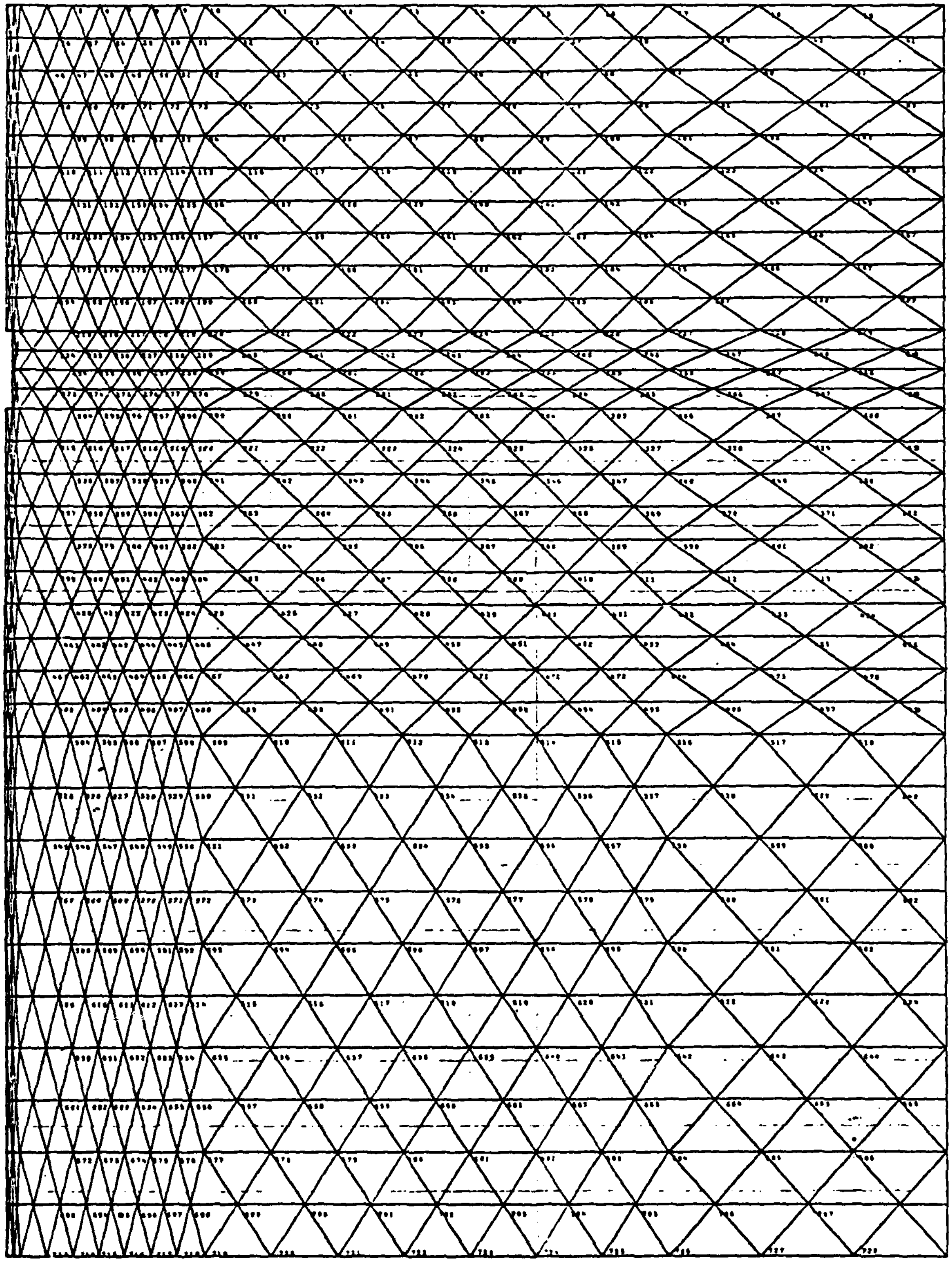

Figure 4. The Finite Element Mesh.

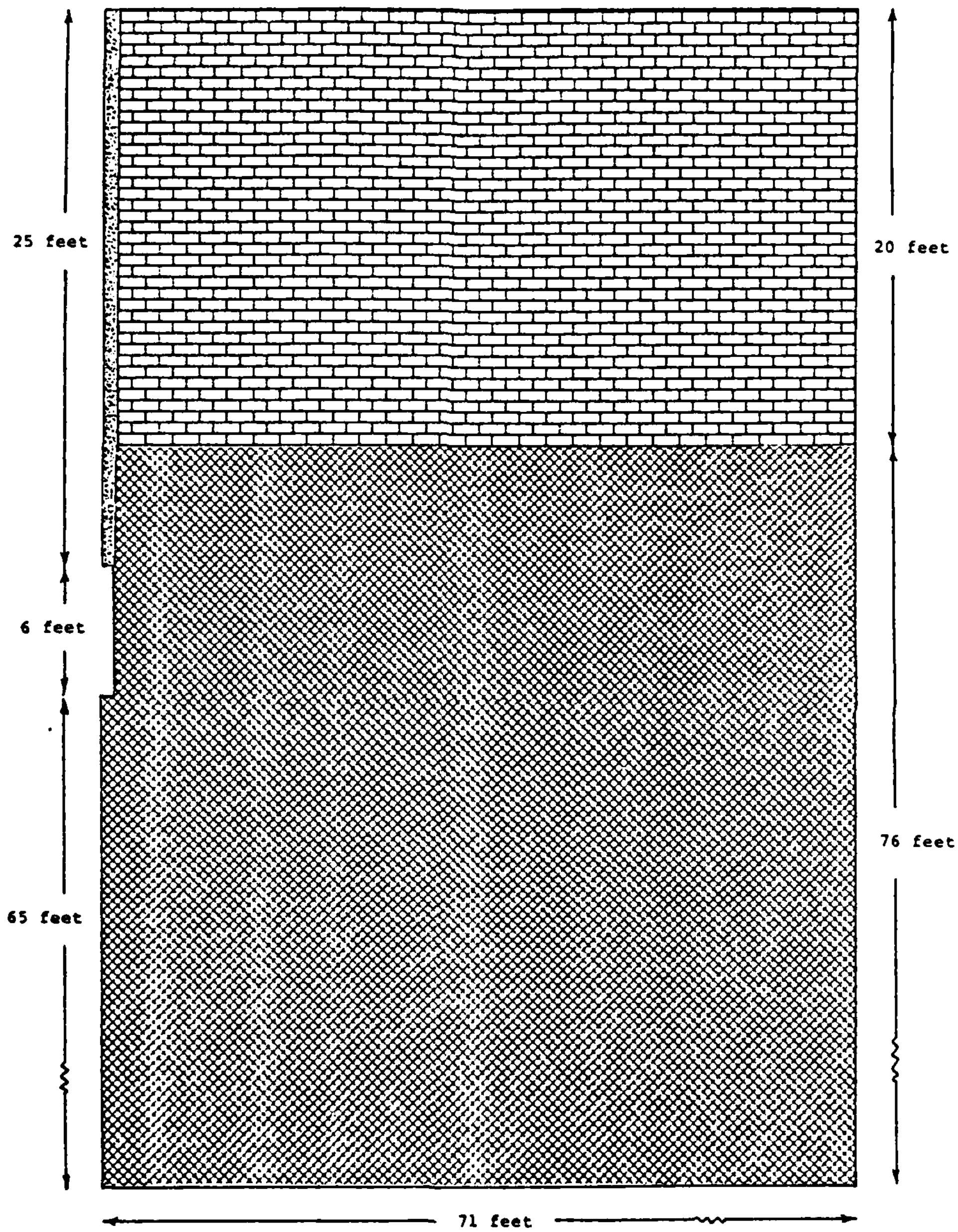

Figure 5. The Geological Setting for Model III.

elements and Model II and III have 729 nodal points and 1348 elements. The size of the finite element models is chosen in such a way that the artificial reflections will not reach the observation points within the time interval of 0 - 15 milliseconds.

The system is set into motion by the application of a sudden, normal stress applied uniformly on both the vertical walls and the two ends of the cylindrical cavity. The time variation of the applied stresses are assumed to be given by a modified Heaviside function as shown in Figure 6. The rise time of the pulse is assumed to be $16\Delta t$, where Δt=20 μseconds, is in order to satisfy the Courant's stability condition.

In order to study the transient response in the region along the vertical surface of the cylindrical cavity, the observation points along LINE A, B, C are selected (see Figure 7). In order to study the diffraction behavior of the rims of the cylindrical cavity and the comparison between the transient response in the weathering layer and the half-space, we choose the observation points to be located along LINE D and E. The observation points along LINE F, G,H,I,J,K are chosen to investigate the transient response in the upper region of the cylindrical cavity and in the filled drilling hole. For the surface response as encountered in seismic exploration, the observation points are selected to be located along LINE L.

For the limited computer time available to the present study, only the computational results for the displacement U_r and U_z in the time interval of 0 - 15 milliseconds for the observation points along LINE A through L of Model I, II, III are obtained as presented in Figure 10 through 21.

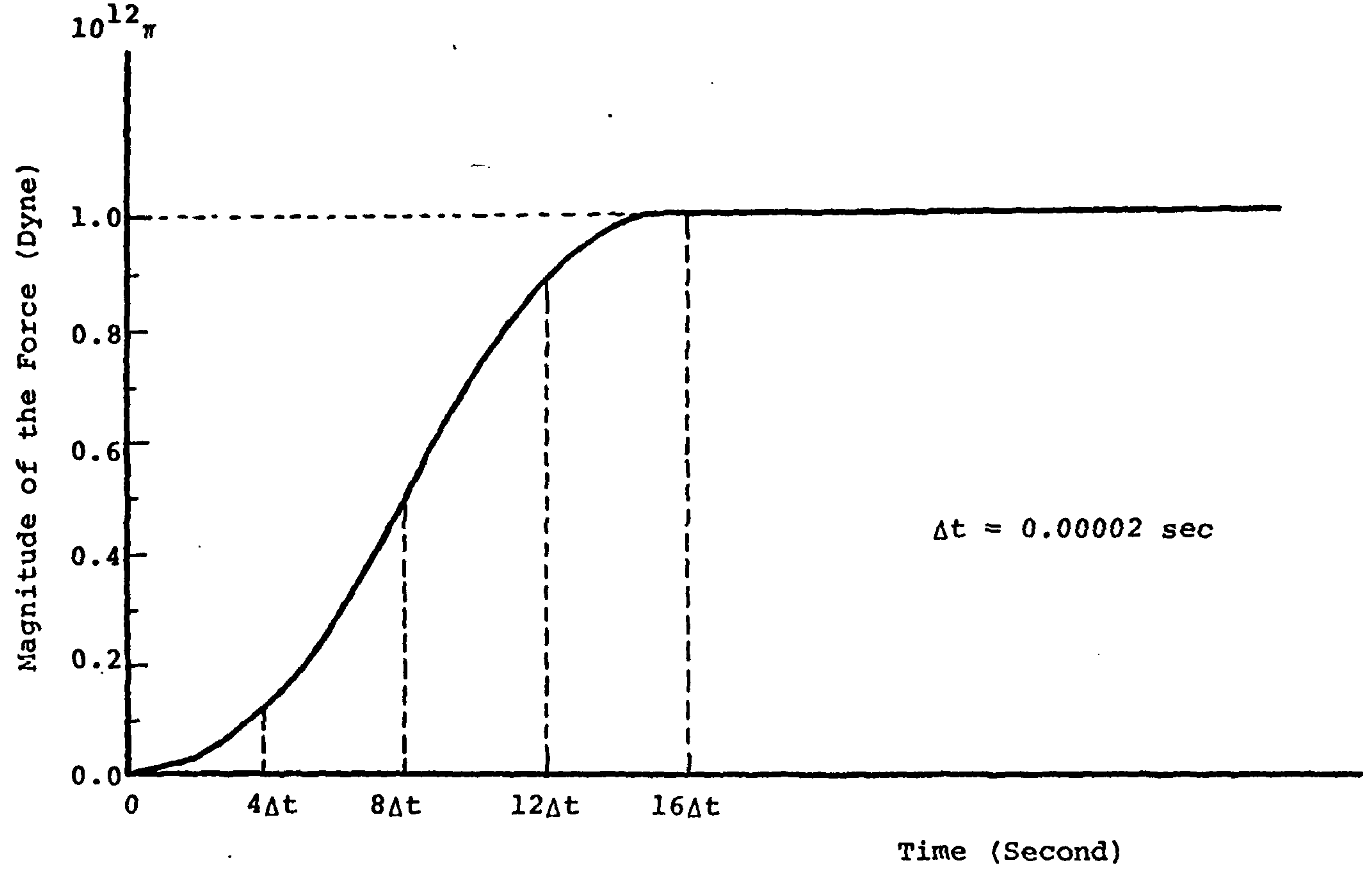

Figure 6. Forcing Function Applied on the Wall of Cylindrical Cavity.

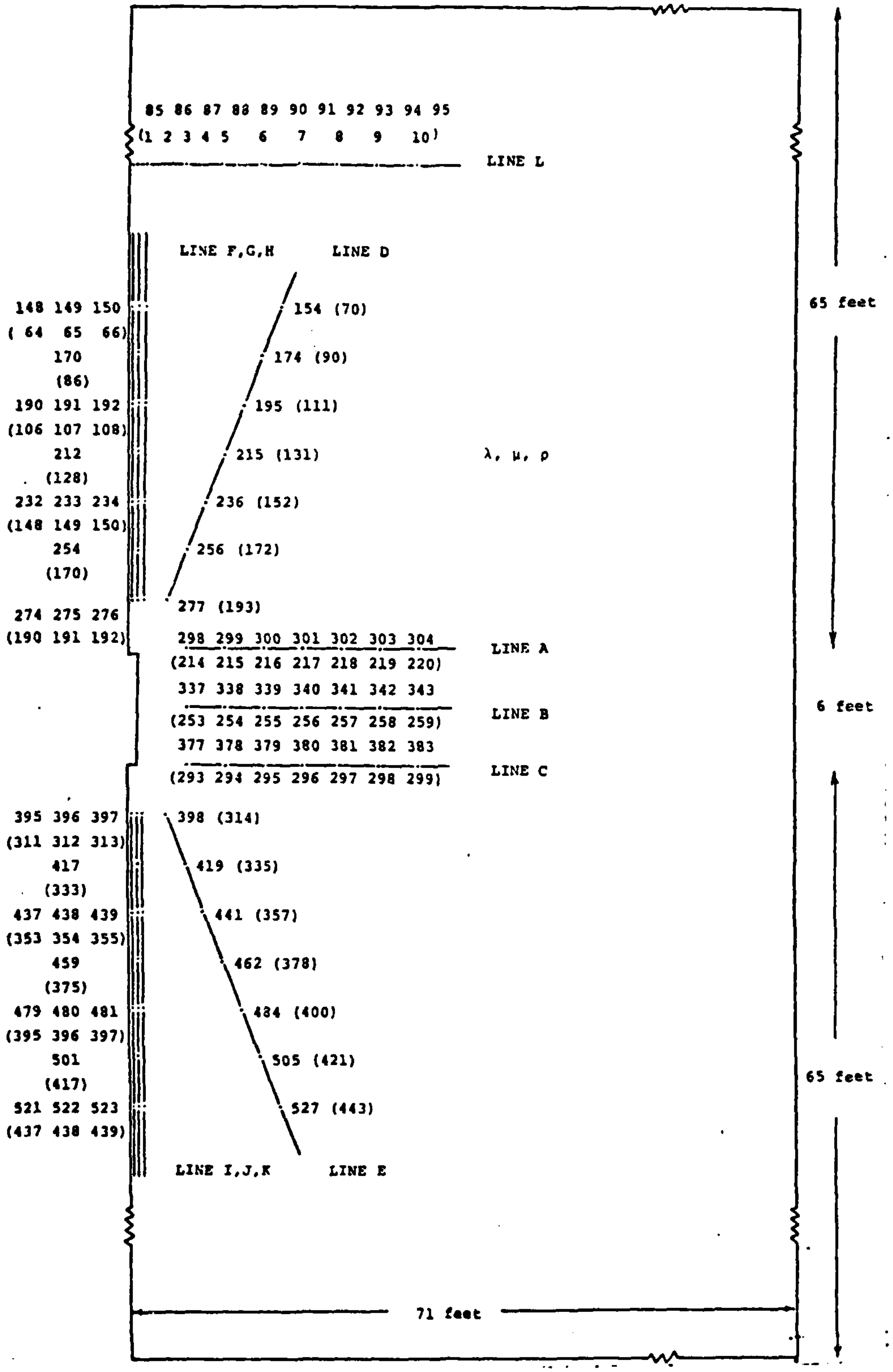

Figure 7a. The Locations of the Observation Points in the Numerical Solution for Model I.

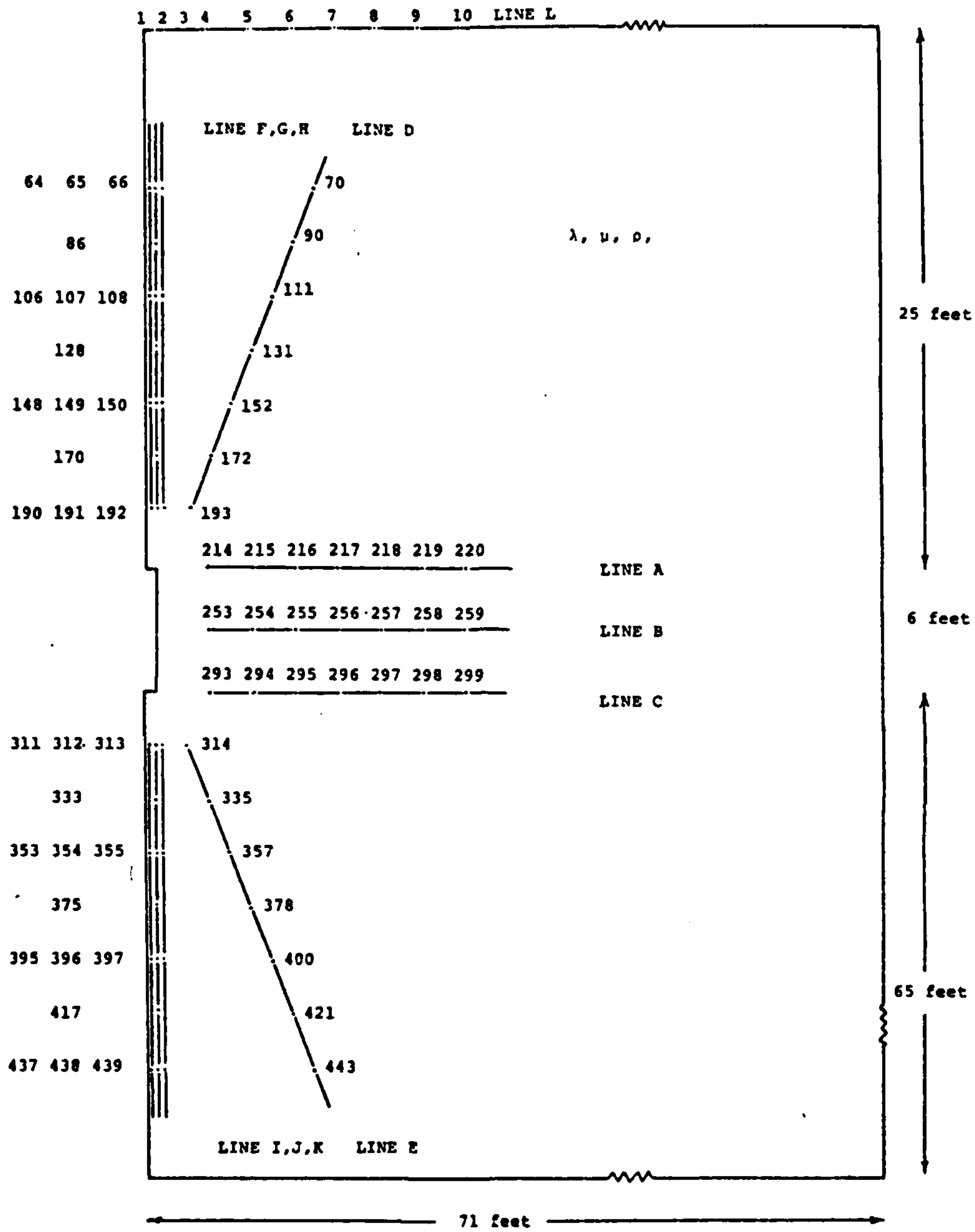

Figure 7b. The Locations of the Observation-Points in the Numerical Solution for Model II.

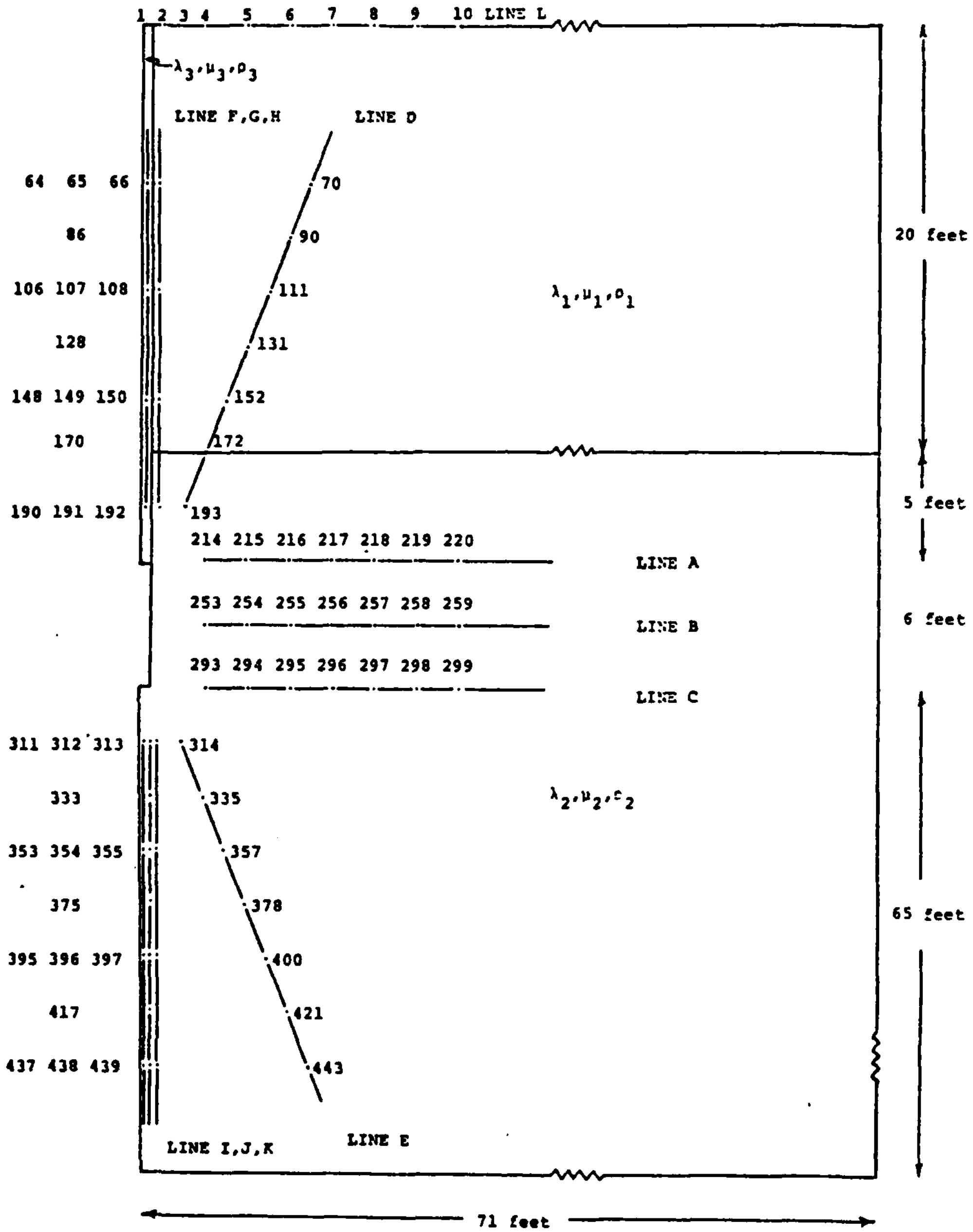

Figure 7c. The Locations of the Observation Points in the Numerical Solution for Model III.

6. INTERPRETATION THE NUMERICAL RESULTS

A. Ray Paths for Model III

It appears to be instructive to use the simple concept of ray to show the various arrivals of waves in Model I, II, and III. As the ray paths for Model I and II are relatively easily traceable, in order to avoid duplication, we choose to show schematically the principal ray paths for Model III of a finite cylindrical cavity source located in a two-layered half-space with a filled drilling hole with unconsolidated material. It is assumed that the upper layer models a weathering layer, whcih is underlain by a relatively consolidated half-space. The filled drilling hole is properly tapped, and there are no blowouts. The cavity simulates a cylindrical charge. The following notations for the expected arrivals of waves are adopted:

(1) Subscripts 1, 2 and 3 refer to wave velocities in the upper layer; i.e. the weathering layer, the underlying half-space and the filled drilling hole, respectively.

(2) Superscript t refers to the rim of the filled drilling hole on the surface, the rim of the contact at the layer-interface, the top rim of the cylindrical cavity, and b refers to the rim of the contact at the layer interface, the bottom rim of the filled drilling hole, and the bottom rim of the cylindrical cavity, so that for example, 1b = 2t, 2b = 3t.

(3) Subscripts J refers to cylindrical waves on the top and bottom faces of the filled drilling hold and the cylindrical cavity of the Bessel function order zero type.

(4) Superscripts, 1N, 2N, and 3N, refer to the repeated multi-ray paths along the surface of the filled drilling hole between 1t, 1b; 2t, 2b; and along the cavity respectively. N is the number of repeated multi-ray path.

(5) Primes, refer to refracted waves.

The ray paths of the principal wave arrivals are shown in Figure 8 and Figure 9, for P-waves, and for P converted into S, respectively. The ray paths for S waves and for S converted into P waves can be similarly traced, according to the Snell's law. The following are the identification of various waves for Models:

(1) Direct Waves,

P, S: P and S waves directly from a point of the cavity source to the observation point.

(2) Direct Diffracted Waves,

P^{3t}, P^{3b}, S^{3t}, S^{3b}: Diffracted P and S waves traveling from the top and bottom rim of the cylindrical cavity source.

(3) Diffracted and Reflected Waves,

$P_2^{3t}P_2$, $P_2^{3b}P_2$, $P_2^{3t}S_2$, $P_2^{3b}S_2$: Diffracted P wave traveling from the top and bottom rim of the cylindrical cavity source to the layer interface and reflected as P wave or converted as S wave, respectively.

$S_2^{3t}P_2$, $S_2^{3b}P_2$, $S_2^{3t}S_2$, $S_2^{3b}S_2$: Diffracted S wave traveling from the top and bottom rim of the cavity source to the layer interface and reflected as P wave or converted as S wave, respectively.

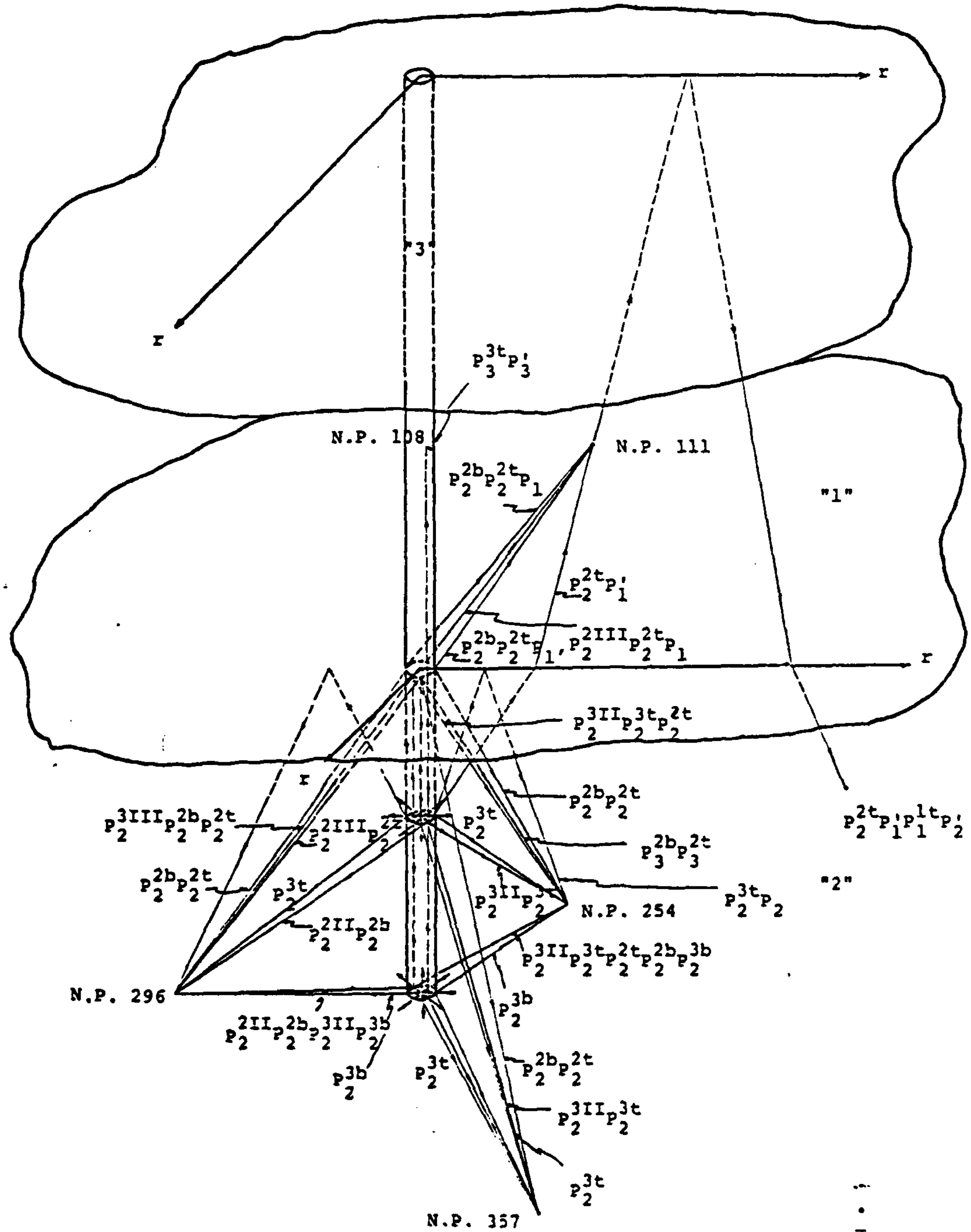

Figure 8. The Ray Paths of the Principal Wave Arrivals

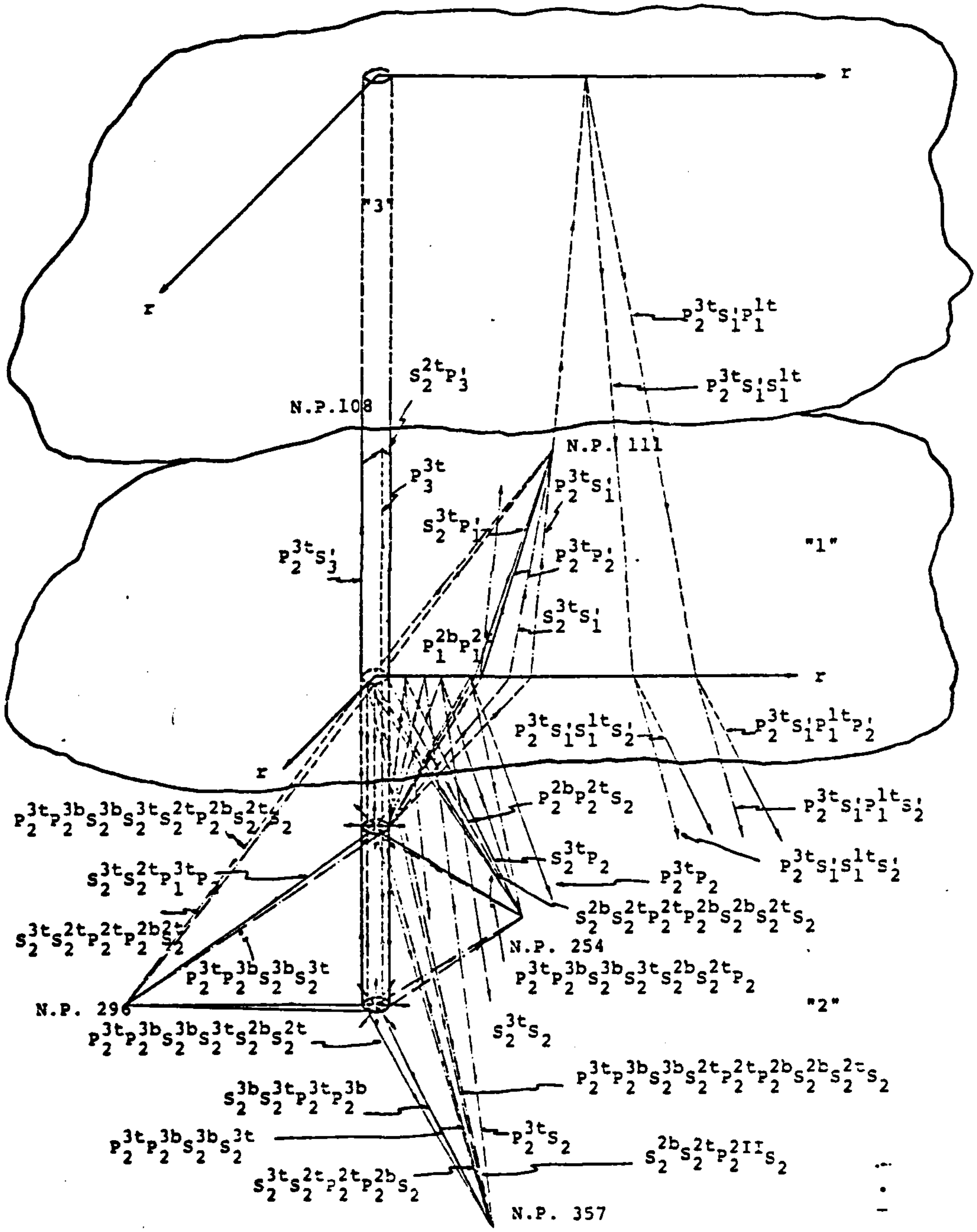

Figure 9. The Ray Paths of the Principal Wave Arrivals (for Converted Waves)

(4) Refracted Waves,

$P_2^{3t}P_1'$, $P_2^{3b}P_1'$, $P_2^{3t}S_1'$, $P_2^{3b}S_1'$: P wave traveling from the top and the bottom rims of the cavity source to the layer interface and refracted into the first medium as P wave, or converted as S wave, respectively.

$S_2^{3t}S_1'$, $S_2^{3b}S_1'$, $S_2^{3t}P_1'$, $S_2^{3b}P_1'$: S wave traveling from the top and the bottom rim of the cavity source to the layer interface and refracted into the first medium as P wave or converted as S wave, respectively.

$P_2^{3t}P_3'$, $P_2^{3t}S_3'$: P wave traveling vertically from the top rim of the cavity source along the interface between the filled drilling hole and the layered medium, with the velocity of the half-space and refracted into the filled drilling hole as P or converted to S.

$P_1^{2t}P_3'$, $P_1^{2t}S_3'$: P wave traveling vertically upward from the rim of the contact between the layer interface and the filled drilling hole and refracted into the filled drilling hole as P or converted to S.

$S_2^{3t}S_3'$, $S_2^{3t}P_3'$: S wave traveling vertically from the top rim of the cavity source along the interface between the filled drilling hole and the layered medium, with the velocity of the half-space and refracted into the filled drilling hole as P or converted to S.

$S_1^{2t}S_3'$, $S_1^{2t}P_3'$: S wave traveling vertically upward from the rim of the contact between the layer interface and the filled drilling hole and refracted into the filled drilling hole as P or converted to S.

(5) Multi-Diffracted Waves,

$P_2^{3t}P_2^{3b}$, $P_2^{3t}P_2^{3b}P_2^{3t}P_2^{3b}(= P_2^{3III}P_2^{3b})$,......

$P_2^{3b}P_2^{3t}$, $P_2^{3b}P_2^{3t}P_2^{3b}P_2^{3t}(= P_2^{3III}P_2^{3t})$,......

AD-A095 919 HENRY KRUMB SCHOOL OF MINES NEW YORK ALDRIDGE LAB OF--ETC F/G 8/11
ELASTIC AND VISCOELASTIC WAVE SCATTERING AND DIFFRACTION.(U)
JAN 81 J T KUO, Y TENG, K CHEN, C E SHEPHERD F49620-77-C-0130
UNCLASSIFIED AFOSR-TR-81-0107 NL

2 OF 3

AD A
095919

$P_2^{3t}P_2^{3b}S_2$, $P_2^{3t}P_2^{3b}P_2^{3t}P_2^{3b}S_2 (= P_2^{3III}S_2^{3b})$,........

$P_2^{3b}P_2^{3t}S_2$, $P_2^{3b}P_2^{3t}P_2^{3b}P_2^{3t}S_2 (= P_2^{3III}S_2^{3t})$,........

Diffracted P wave traveling periodically from the top rim to the bottom rim of the cavity along the vertical interface of the cylindrical cavity and diffracted as P wave or converted as S wave respectively at the top (or bottom) rim of the cavity.

$P_2^{2b}P_2^{2t}$, $P_2^{2b}P_2^{2t}P_2^{2b}P_2^{2t} (= P_2^{2III}P_2^{2t})$,............

$P_2^{2b}P_2^{2t}P_2^{2b}$, $P_2^{2b}P_2^{2t}P_2^{2b}P_2^{2t}P_2^{2b} (= P_2^{2IV}P_2^{2b})$,.......

$P_2^{2b}P_2^{2t}S_2$, $P_2^{2b}P_2^{2t}P_2^{2b}P_2^{2t}S_2 (= P_2^{2III}S_2^{2t})$,.......

$P_2^{2b}P_2^{2t}P_2^{2b}S_2$, $P_2^{2b}P_2^{2t}P_2^{2b}P_2^{2t}P_2^{2b}S_2 (= P_2^{2IV}S_2^{2t})$,..

Diffracted P wave traveling vertically along the hole between the top of the cylindrical cavity and the layer interface and diffracted as P wave or converted as S wave respectively at the top rim of the cylindrical cavity or the layer interface.

(6) Special Waves,

$P_J P_2^{3t}P_2^{3b}P_J P_2^{3b}$, $P_J P_2^{3b}P_2^{3t}P_J P_2^{3t}$,

$P_J P_2^{3t}P_2^{3b}P_J P_2^{3b}P_2^{3t}P_J P_2^{3t} (= P_J P_2^{3II}P_2^{3t})$,.......

P wave traveling periodically from the bottom (or the top) face of the cavity with a motion described by the Bessel function order zero, through the vertical face of the cavity, to the top (or the bottom) face of the cylindrical cavity also with a motion described by the Bessel function order zero.

B. Detailed Interpretation of Synthetic Seismograms

Figure 10 through 21 show synthetic seismograms of both the radial and vertical displacements U_r and U_z of the transient response of Model I - a whole space, Model II - a half-space, and Model III - a layer half-space due to a finite cylindrical cavity source embedded in the medium at the observation points along lines, A to L, as shown in Figure 7.

We here shall attempt to identify the principal wave arrivals, by means of both the recognition of the change of the characteristics of the wave forms and the expected arrival times of these principal waves based on the ray tracing technique.

Line A

Figure 10 shows synthetic seismograms of Line A, at the nodal points 214,215,216,217,218,219 and 220 for Model I, II, and III. (See Figure 7 for the locations of the nodal points) In Figure 10 a_1, the radial displacement U_r, the arrivals of each trace, P_2, S_2^{3b}, $P_J P_2^{3b} P_2^{3t} P_J P_2$, $P_2^{3t} P_2^{3b} P_2^{3t}$, and the multiples of $P_J P_2^{3b} P_2^{3t} P_J P_2$, $P_2^{3t} P_2^{3b} P_2^{3t}$ are identified. The paths of these arrivals are shown in Figure 8 and Figure 9. In addition to these arrivals, by comparing the radial and vertical displacements of Model I with these of Model II, the arrival of the wave, $P_2^{3t} P_2$, is identified as a step in time and is indicated in Figure 10 a_2'. The arrivals of P_2, $P_J P_2^{3b} P_2^{3t} P_J P_2$, $P_2^{3t} P_2^{3b} P_2^{3t}$, $P_2^{2b} P_2^{2t} P_2$, $P_2^{2b} P_2^{2t} S_2$, $P_3^{2b} P_3^{2t} P_2$, $P_3^{2b} P_3^{2t} S_2$, $S_3^{2b} S_3^{2t} P_2$ and the multiples of $P_2^{2b} P_2^{2t} P_2$, $P_2^{2b} P_2^{2t} S_2$, $P_2^{3t} P_2^{3b} P_2^{3t}$, and $P_J P_2^{3b} P_2^{3t} P_J P_2$ are similarly identified in

Figure 10 a_3 for Model III.

As the P wave velocity in the half-space is assumed to be 5000 ft/sec, the travel time of 1.2 milliseconds for a P wave is equivalent to the travel distance of 6 feet, which is the length of the cylindrical cavity. In Figure 10 a_1, the periodic wave train immediately following the arrivals of $P_2^{3t}P_2^{3b}P_2^{3t}$ with a period of about 1.2 millisecond marked by "A" on the seismograms begining at 4.2 milliseconds with respect to the origin time, appears to fit the traveling path of the type of P wave $P_2^{3t}P_2^{3b}P_2^{3t}$ traveling periodically from the top rim to the bottom rim of the cavity as P wave along the vertical interface of the cylindrical cavity. The wave train with a period of 1.6 milliseconds marked by "B" on the trace 214 in Figure 10 a_1 is indicated as $P_JP_2^{3t}P_2^{3b}P_JP_2^{3b}$, as the travel time of 1.6 milliseconds for P in the half-space is equivalent to the traveling distance of 8 feet. The P wave $P_JP_2^{3t}P_2^{3b}P_JP_2^{3b}$ apparently is traveling back and forth periodically around the cylindrical cavity. Because the distances between each of the observation point and the top and bottom rims of the cylindrical cavity are different, waves originated from the top rim and from the bottom rim of the cylindrical cavity interfere constructively and destructively, depending on the distances between the observation point and the top and bottom rims of the cavity. In Figure 10 a_2, for the velocity of the medium assumed, reflected waves, $P_2^{3t}P_2$, from the surface boundary of the half-space does not seem to have significant effects on the amplitude of the wave, compared with P_2^{3t} in a whole space, as in Figure 10 a_1. Seismograms in Figure 10 a_3, and especially 10 a_3', show the superposition of the short period waves of about 1.2 milliseconds on the long period wave of about 5 milliseconds, as marked by "L". The long period waves observed on these seismograms are essentially generated in the filled drilling hole with a very low velocity as radiated cylindrical waves, as the refracted waves from the weathering layer arrive later than the time of 1.5 milli-second. The travel time of the P wave in the filled drilling hole from the top of the cylindrical cavity to the layer interface is 5 milli-second, corresponding to a distance of 5 feet. The travel distance of the wave $P_3^{2b}P_3^{2t}P_2$ is exactly 5 feet. Therefore, these long period waves are identified as $P_3^{2b}P_3^{2t}$, traveling along the hole vertically between the top of the cylindrical cavity and the layer interface. The input step function is not as clearly preserved in the radial displacement in Figure 10 a_1, a_2, and a_3 as in the vertical displacements as shown in Figure 10 a_1',a_2' and a_3'. For a finite cylindrical cavity source, the preservation of the input step largely depends on the configuration of the observation point. All the observation points in Figure 10 a_1, a_2, and a_3 are located along a line perpendicular to the axis and parallel to the top and bottom faces of the cylindrical cavity. The normal applied stresses on the vertical face of the cavity contribute to the radial displacement in a radially outward direction, but the applied stresses on the end faces of the cavity tend to elongate the cavity in an axial direction and contribute to the radial displacement in a radially inward direction along the vertical face of the cavity. The combination of the applied stresses on the both end faces and the vertical face of the cavity gives the resultant complicated radial displacement. Because Nodal Point 214 is only 2.5 feet from the top rim of the cylindrical cavity, the contribution due to the applied stresses on the both end faces of the cylindrical cavity to the radial displacement, at Nodal Point 214 is approximately the same order of magnitude as that due to the applied stresses on the vertical face of the cavity, as reflected through a radially outward response of the wave forms between the arrivals P_2^{3t} and S_2^{3b}. As the distances between Nodal Points 215 to 220, and the cylindrical cavity increase, the contribution due to the applied stresses on the both end faces of the cavity becomes pre-dominant, as reflected through the radially inward response of the wave forms between the arrivals P_2^{3t} and S_2^{3b}, as designated by "C". In Figure 10 a_1', and a_2' , the vertical displacements U_z, the wave arrivals P_2, S_2^{3b}, $P_2^{3t}P_2^{3b}P_2^{3t}S_2$, $P_J P_2^{3III}P_2^{3t}$, $P_2^{3t}P_2^{3b}P_2^{3t}P_2^{3b}P_2^{3t}$ and the multiples of $P_2^{3t}P_2^{3b}P_2^{3t}S_2$, $P_J P_2^{3III}P_2^{3t}$ and $P_2^{3t}P_2^{3b}P_2^{3t}P_2^{3b}P_2^{3t}$ are identified. The ray paths of these arrivals are given in Figures 8 and 9. In addition to these arrivals, the arrival of a step $P_2^{3t}P_2$, in Model II Figure 10 a_2', is identified. In Figure 10 a_3' of the vertical displacement U_z of Model III, the arrivals, P_2, $P_2^{2b}P_2^{2t}$, $P_2^{2b}P_2^{2t}S_2$, $P_3^{2b}P_3^{2t}$, $P_2^{3t}P_2^{3b}S_2$, and $P_3^{2b}P_3^{2t}S_2$ and the multiples of $P_2^{2b}P_2^{2t}$, $P_2^{2b}P_2^{2t}S_2$, $P_3^{2b}P_3^{2t}$ $P_3^{2b}P_3^{2t}S_2$ are identified. The wave arrival of $P_2^{3t}P_2^{3b}P_2^{3t}S_2$ is predominant on all the seismograms in Figure 10 a_1' , a_2' and a_3'. The arrival of $P_3^{2b}P_3^{2t}S_2$ contrarily is only predominant on the seismograms of Figure 10 a_3' . The wave, $P_J P_2^{3b}P_2^{3t}P_J P_2^{3t}$, is identified in each seismogram of Figure 10 a_1' and a_2'. It has a period of about 1.6 milliseconds, as specifically marked "A" on the trace of Nodal Point 217 in the time interval of 8.3 milliseconds and 9.9 milliseconds. The identification of the wave is based on the fact that the P wave velocity in the half-space is 5000 ft/sec, the travel time of 1.6 milliseconds for the P wave is equivalent to the travel distance of 8 feet.

Therefore, the wave $P_J P_2^{3b} P_2^{3t} P_J P_2^{3t}$ is the type of the wave traveling periodically from the bottom (or the top) face of the cavity with a motion described by the Bessel function order zero, through the vertical face of the cavity, to the top (or the bottom) face of the cylindrical cavity also with a motion described by the Bessel function order zero. The ray path of this type of wave is shown in the following diagram.

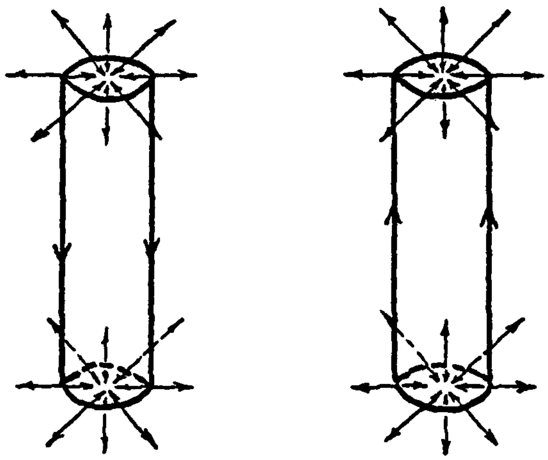

Line B

Figures 11, give synthetic seismograms of the radial displacement U_r and vertical displacement U_z of Line B at Nodal Point 253,254,255,256,257,258 and 259 for Model I, II, and III as shown in Figure 7. The waves P_2, P_2^{3t}, $P_2^{3t} P_2^{3b}$, $P_2^{3b} P_2^{3t}$, $P_J P_2^{3t} P_2^{3b} P_J P_2^{3b}$ and the multiples of $P_2^{3t} P_2^{3b}$, $P_2^{3b} P_2^{3t}$ and $P_J P_2^{3t} P_2^{3b} P_J P_2^{3b}$ are all identified in Figure 11 a_1, Model I, the whole space.

The reflected and converted waves from the layer interface and the diffracted from the top rim of the filled drilling hole, 2t. $P_2^{3t}P_2$, $P_2^{3b}P_2$, $P_2^{3t}S_2$, $P_2^{3b}S_2$, $P_2^{3t}P_2^{3b}P_2^{3t}$, $P_2^{3t}P_2^{3b}P_2^{3t}P_2^{2t}$, $P_JP_2^{3t}P_2^{3b}P_JP_2^{3b}$ and the multiples of $P_2^{3t}P_2^{3b}P_2^{3t}$, $P_2^{3t}P_2^{3b}P_2^{3t}P_2^{2t}$, $P_JP_2^{3t}P_2^{3b}P_JP_2^{3b}$ are identified in Figure 11 a_3 for Model III. The predominant waves observed include: (1) $P_2^{3t}P_2^{3b}P_2^{3t}$, traveling periodically from the top to bottom along the vertical face of the cylindrical cavity with a velocity of 5000 ft/sec and a period of about 1.2 milliseconds. (2) $P_JP_2^{3t}P_2^{3b}P_JP_2^{3b}$, travels periodically from the bottom (or the top) face of the cavity with a motion described by the Bessel function order zero, through the vertical face of the cavity, to the top (or the bottom) face of the cylindrical cavity also with a motion described by the Bessel function order zero.

The normal applied stress on the vertical face of the cavity contributes to the radial displacement in a radially outward direction, (i.e. the sense of direction on the seismogram is "positive") but the applied stresses on the end faces of the cavity tend to elongate the cavity in an axial direction and contribute to the radial displacement in a radially inward direction (i.e. the sense of direction on the seismogram is "negative") along the vertical face of the cavity everywhere. Morever, there are stress concentrations around both the top and the bottom rims of the cavity. As the location of the Nodal Point 253 is only 2.5 feet from the vertical face of the cavity and an equal distance of 3.9 feet from both the top rim and the bottom rim of the cavity, the first arrival P wave from a minimum distance between the observation point Nodal Point 253 and the vertical face of the cavity contributes to the radial displacement in a radially outward direction; the diffracted arrivals P_2^{3t} and P_2^{3b} from both the end faces of the cavity contribute to the radial displacement in a radially inward direction. Subsequently, the arrivals of the diffracted waves $P_2^{3b}P_2^{3t}$, and $P_2^{3t}P_2^{3b}$ and their multiples contribute to the radial displacement to have an oscillatory appearence. Therefore the arrivals of the waves, P, P_2^{3t}, P_2^{3b}, $P_2^{3t}P_2^{3b}$, $P_2^{3b}P_2^{3t}$ give an impulsive like wavelet in the time interval of 0 and 3 milliseconds, and the arrivals of the multiples of the diffracted waves $P_2^{3t}P_2^{3b}$ and $P_2^{3b}P_2^{3t}$give the resultant oscillatory radial displacement and followed by a long period wave train as clearly shown in the seismograms of Nodal Point 253 of Model I, II, and III (see Figure 11 a_1, a_2, and a_3).

As expected, there are no vertical displacement at every nodal point along Line B, symmetrically with respect to the two end faces of the cylindrical cavity in Model I, in the whole space as shown in Figure 11 a_1'. Because the applied stresses on the both end faces of the cavity are equal and in an opposite direction, the resultant vertical displacement along Line B is therefore zero; Likewise the stresses applied to the vertical face of the cavity are in the r-direction, the resultant vertical displacement along Line B is also zero. In Figure 11 a_2' ,the vertical displacement along Line B for Model II, a half space, is zero until the arrival of $P_2^{3t}P_2$, i.e. P wave is reflected at the surface of the half-space. The waves for Model III are complex as shown in Figure a_3'. There are eight principal arrivals accounted for, e.g. $P_2^{3b}P_2^{3t}$, $P_2^{3t}P_2$, $P_2^{3t}S_2$, $S_2^{3b}S_2$, $S_2^{3t}S_2$, $P_2^{3b}P_2^{3t}P_3^{2b}P_3^{2t}S_2$, $P_3^{2b}P_3^{2t}P_2$ and $P_3^{2b}P_3^{2t}S_2$, and the multiples of $P_3^{2b}P_3^{2t}P_2$ and $P_3^{2b}P_3^{2t}S_2$.

Waves with a period close to 5 milliseconds marked by "A" are clearly identifiable on virtually all the seismograms in Figure 11 a_3' ; they are $P_3^{2b}P_3^{2t}P_2$ traveling periodically along the vertical face of the drilling hole between the two rims at 2b and 2t with the velocity of the filled drilling hole.

Line C

Figure 12 gives synthetic seismograms of the radial displacement U_r and the vertical displacement U_z of Line C at Nodal Point 293,294,295,296,297,298, and 299. Line C lies in the plane of the bottom face of the cavity, as Line A lies in the plane of the top face of the cavity. The locat' ns of these nodal points are shown in Figure 7. As expected, the radial displacements of all these nodal points as shown in Figure 12 a_1 are identical to these as shown in Figure 10 a_1, the vertical displacements of all these nodal points as shown in Figure 12 a_1', are also identical to these of Figure 10 a_1', except the vertical displacements of Line C are in an opposite direction of these of Line A. The seismograms of the radial and the vertical displacements as shown in Figure 12 a_2 and a_2' are identical to these as shown in Figure 12 a_1 and a_1', until the arrival of $P_2^{3t}P_2$ and $P_2^{3b}P_2$ as in the case of Line A. In comparison of the radial and the vertical displacements Line C in Figure II-12 a_3 and a_3' with these of Figure 12 a_1 and a_1', the arrivals of $P_2^{3b}P_2$, $P_2^{3t}P_2$, $P_2^{3t}S_2$, $P_2^{3b}S_2$, $P_3^{2b}P_3^{2t}P_2$, $P_3^{2b}P_3^{2t}S_2$, $P_3^{2b}P_3^{2t}P_3^{2b}P_2$ and $P_3^{2b}P_3^{2t}P_3^{2b}P_2$ are easily identified on the seismograms of Model III as shown in Figure 12 a_3 and a_3'.

Line D

Figure 13 shows synthetic seismograms of the radial displacement U_r and vertical displacement U_z of Line D at Nodal Point 193,172,152,131,111,90 and 70 for Model I, II, and III. As shown in Figure 7, Line D is situated diagonally with respect to the top rims of the cylindrical cavity. For Model III, Nodal Point 193 is in the half-space, 172 in the layer interface, and 152,131,111,90, and 70 in the weathering layer as shown in Figure 7c. The wave arrivals P_2^{3t}, S_2^{3t}, P_2^{3b}, S_2^{3b}, $P_2^{3b}P_2^{3t}S_2$, $P_2^{3b}P_2^{3t}P_2^{3b}P_2^{3t}$, $P_2^{3b}P_2^{3t}P_2^{3b}P_2^{3t}S_2$, $P_JP_2^{3b}P_2^{3t}P_JP_2^{3t}$ and the multiples of $P_2^{3b}P_2^{3t}P_2^{3b}P_2^{3t}$, $P_2^{3b}P_2^{3t}P_2^{3b}P_2^{3t}S_2$ and $P_JP_2^{3b}P_2^{3t}P_JP_2^{3t}$ are all identified on every seismogram of Figure 13 a_1 and a_2, Model I, and II. In Figure 13 a_3, the arrivals at Nodal Point 193 include P_2^{3t}, P_2^{3b}, S_2^{3t}, $P_JP_2^{3t}$, S_2^{3b}, $P_2^{2b}P_2^{2t}P_2^{2b}P_2^{2t}S_2$, $P_3^{2b}P_3^{2t}P_2$, $P_3^{2b}P_3^{2t}S_2$, $S_3^{2b}S_3^{2t}P_2$, $S_3^{2b}S_3^{2t}S_2$ and the multiples of $P_2^{2b}P_2^{2t}P_2$, $P_3^{2b}P_3^{2t}P_2$, $P_2^{2b}P_2^{2t}S_2$, $P_3^{2b}P_3^{2t}S_2$ and $P_JP_2^{3b}P_2^{3t}P_JP_2^{3t}$.

Nodal Point 193 is located at a distance of 2.9 feet from the top rim of the cavity and at a distance of 8.6 feet from the bottom rim of the cavity. Since Nodal Point 193 is located above the cavity, the applied stress on the top end-face of the cavity contributes to the radial displacement at Nodal Point 193 in a radially outward direction for the arrival of P_2^{3t}, and the applied stress on the bottom end-face of the cavity contributes to the radial displacement at Nodal Point 193 in a radially inward direction for the arrival of P_2^{3b}. In Figure 13 a_3, the high frequency components with a period of .1 milli-second are superimposed on the low frequency component as shown in the seismogram of Nodal Point 193. As Nodal Point

193 is located very close to the top of the cylindrical cavity, the location is very sensitive to the motion on the immediate top end of the cavity, therefore, the wave $P_J P_2^{3t}$ is the type of the wave traveling periodically from the top rim of the cavity to the axis of the cavity with a period of 1 milliseconds. On the trace of Nodal Point 172 in Figure 13 a_3, the high frequency arrivals with a period around 1.2 milliseconds are superimposing on top of the low frequency response. The wave $P_2^{3b} P_2^{3t}$ is the type of the wave traveling periodically from top to bottom of the cavity along the vertical wall of the cavity. The long period wave is shown on all the traces in Figure 13 a_3. This long period waves is identified as $P_3^{2b} P_3^{2t}$, traveling with the P wave velocity in the shot hole between the two rims at 2b and 2t. The Nodal Point 152,131,111,90, and 70 are located in the first layer (weathering layer), all the high frequency arrivals are filtered out in the seismogram of Figure 13 a_3 and a_3'. The weathering layer behaves as a low pass filter.

In Figure 13 a_1' and a_2', seven arrivals, P_2^{3t}, P_2^{3b} S_2^{3t}, S_2^{3b}, $P_2^{3b} P_2^{3t} P_2^{3b} P_2^{3t}$, $P_2^{3b} P_2^{3t} P_2^{3b} P_2^{3t} S_2$, $P_J P_2^{3t} P_2^{3b} P_J P_2^{3b} P_2^{3t} P_J P_2^{3t}$ and the multiples of $P_J P_2^{3t} P_2^{3b} P_J P_2^{3b} P_2^{3t} P_J P_2^{3t}$ are identified, likewise the arrival of $P_2^{3t} P_2$ also is identified on each seismogram in Figure 13 a_2'. In Figure 13 a_3', the arrivals of P_2^{3t}, S_2^{3t}, $P_2^{3t} P_2^{2t} P_2$, $S_2^{3t} S_2^{2t} S_2$, $P_2^{2b} P_2^{2t} P_2^{2b} P_2^{2t} P_2^{2b} P_2$ $P_3^{2b} P_3^{2t} P_2$, $P_2^{3t} P_2^{3b} P_2^{2t} P_2^{3b} P_2^{2t} P_2$ and the multiples of $P_3^{2b} P_3^{2t}$ are identified on the seismogram of Nodal Point 193; the arrivals of P_2^{3t}, S_2^{3t}, $P_2^{3t} P_2^{2t} P_1'$, $P_2^{3t} P_2^{2t} S_1'$, $P_3^{2b} P_3^{2t} P_1'$ and the multiples of $P_3^{2b} P_3^{2t}$ are identified on the trace of Nodal Point 172.

For the rest of the seismogram the first arrival of $P_2^{3t}P_1'$ is clearly identifiable. In Figure 13 a_1' and a_2', the wave with a period of about 1.6 milliseconds as marked by "A" on the seismogram of Nodal Point 172 in a_2' is identified as $P_J P_2^{3b} P_2^{3t} P_J P_2^{3t}$ on the basis of the travel path and the travel time. The wave $P_J P_2^{3b} P_2^{3t} P_J P_2^{3t}$ is the type of waves traveling periodically from bottom end-face of the cavity, through vertical face of the cavity, then to the top face of the cavity with a travel time of 1.6 milliseconds. The direct shear wave S_2^{3t} is clearly identified on the seismogram of Nodal Point 193 for Model III, Figure 13, a_1', a_2', and a_3'. The long period waves in Figure 13 a_3 and a_3' are $P_3^{2b}P_3^{2t}P_2$, which travels with a P wave velocity of the filled drilling hole periodically along the vertical face of the hole between the top and bottom rims at 2b and 2t. The shape of the input forcing function is well preserved on each seismogram in Figure 13 a_1, a_2, a_3, a_1', a_2', and a_3' as indicated by dash lines.

Line E

Figure 14 shows the synthetic seismograms of the radial displacement U_r and the vertical displacement U_z of Line E at Nodal Point 314,335,357,378,400,421, and 443 as shown in Figure 7. Line E is situated diagonally with respect to the bottom rim of the cylindrical cavity. Therefore, the radial and vertical displacements shown in Figure 14 a_1 and a_1' are identical to those displacements in Figure 13 a_1 and a_1', except the vertical displacements in Figure 14 a_1' are in the opposite direction and are negative as shown in Figure 13 a_1'. The seismograms as shown in Figure 14 a_2

and a_2' are identical to those as shown in Figure 14 a_1 and a_1' until the arrival of $P_2^{3t}P_2$ in Model II, the half-space. Since the nodal points of Line E are located in the half space and far away from the layer interface and the filled drilling hole, the effects of weathering layer and the filled drilling hole on the early response of the radial and vertical displacement at these nodal points of Line E are insignificant. However, arrivals, $P_2^{3t}P_2$, $P_2^{3b}P_2$, $P_2^{3t}S_2$, $P_2^{3b}S_2$, $S_2^{3t}P_2$, $P_3^{2b}P_3^{2t}P_2$, $S_2^{3b}S_2$, $P_3^{2b}P_3^{2t}S_2$, $P_3^{2b}P_3^{2t}P_3^{2b}P_2$, $P_3^{2b}P_3^{2t}P_3^{2b}S_2$ and $S_3^{2b}S_3^{2t}P_2$ are identifiable in Figure II-14 a_3 and a_3'.

Line F

Figure 15 shows the synthetic seismograms of the radial displacement U_r and the vertical displacement U_z of Line F at Nodal Point 192,150,108, and 66.(Figure 7) For Model III, Nodal Point 192 is in the half-space, and 150 108, and 66 in the weathering layer. In Figure 15 a_1 and a_2, the arrivals of the waves P_2^{3t}, P_2^{3b}, S_2^{3t}, S_2^{3b}, $P_2^{3b}P_2^{3t}$ and $P_JP_2^{3b}P_2^{3t}P_JP_2^{3t}$ and the multiples of $P_2^{3b}P_2^{3t}$, and $P_JP_2^{3b}P_2^{3t}P_JP_2^{3t}$ are identified. In Figure 15 a_3, the arrivals of the waves P_2^{3t}, S_2^{3t}, $P_2^{2b}P_2^{2t}$, $P_2^{3b}P_2^{3t}$, $P_2^{3b}P_2^{3t}P_2^{2t}$, $P_3^{2b}P_3^{2t}$ and the multiples of $P_2^{3b}P_2^{3t}$, $P_2^{3b}P_2^{3t}$, and $P_3^{3t}P_3^{2t}$ are also identified in the seismogram of Nodal Point 192, which is in the half-space. The arrival of P_2^{3t}, $P_2^{3b}P_2^{3t}$, $P_2^{2b}P_2^{2t}$, $P_2^{3t}P_2^{2t}P_1'$, $P_2^{3t}P_2^{2t}S_1'$, $P_3^{3t}P_3^{2t}P_1'$, $P_3^{3t}P_3^{2t}S_1'$, $P_2^{3b}P_2^{3t}P_2^{2t}P_1'$ and the multiples of $P_2^{2b}P_2^{2t}$, $P_2^{3b}P_2^{3t}$, $P_2^{3t}P_2^{2t}P_1'$, $P_2^{3t}P_2^{2t}S_1'$, and $P_2^{3b}P_2^{3t}P_2^{2t}P_1'$ are identified on the seismogram of Nodal Point

150. Since Nodal Point 150,108, and 66 are all located in the weathering layer,which behaves as a low-pass filter, all the high frequency responses are filtered out in the the seismograms of Figure 15 a_3 and a_3'. Several beats are observed in the seismograms of the the radial displacement U_r in Figure 15 a_1, a_2, and a_3.

The beat phenomenon is commonly observed at two wavetrains of slightly different frequencies beat together to give the beats and the amplitude modulation. In the present case, from seismogram at Nodal Point 192 in Figure 15 a_1, the period of the envelope of the beats as marked by "beats" in the time interval of 6.8 milliseconds and 11.8 milliseconds is measured to be 5 milliseconds, and the period of the amplitude modulation on the seismogram of Nodal Point 192 in the time interval of 8.6 milliseconds to 9.3 milliseconds is measured to be 0.7 milliseconds Therefore, the frequency of the envelope of the beats and that of the amplitude modulation are found to be about 196 and 1333 Hz, respectively. By knowing these two frequencies, the periods of these two wavetrains are 1.3 milliseconds and 1.7 milliseconds. Therefore, these two corresponding waves are identified as $P_2^{3b}P_2^{3t}$, which travels periodically from the bottom to the top of the cavity along the vertical face of the cylindrical cavity with a period 1.2 milliseconds and as $P_J P_2^{3b} P_2^{3t} P_J P_2^{3t}$, which travels back and forth periodically from the center of the bottom (or top) end-face of the cavity, to the rim , then travels along the vertical face of the cavity, to the center of the top (or bottom) end-face of the cavity through the rim with a period of 1.6 milliseconds These beat phenomena are also clearly observed on the radial displacements of Nodal Point 150,108, and 66. A typical beating phenomenon is shown in the seismograms.

In Figure 15 a_1' and a_2', the arrivals of the waves P_2^{3t}, S_2^{3t}, $P_2^{3b}P_2^{3t}S_2$, $P_2^{3t}P_2^{3b}P_2^{3t}$, $P_2^{3t}P_2^{3b}P_2^{3t}S_2$, $P_JP_2^{3b}P_2^{3t}P_JP_2^{3t}$, and the multiples of $P_2^{3t}P_2^{3b}$, $P_2^{3b}P_2^{3t}S_2$, $P_2^{3t}P_2^{3b}P_2^{3t}S_2$ and $P_JP_2^{3b}P_2^{3t}P_JP_2^{3t}$ are identified on each seismogram of the nodal point. The arrivals of $P_2^{3t}P_2$ are also identified on each seismogram as shown in Figure 15 a_2'. In Figure 15 a_3', the arrivals of P_2^{3t}, S_2^{3t}, $P_2^{3t}P_2$, $P_2^{3t}S_2$, $P_2^{2b}P_2^{2t}P_2$, $P_2^{2b}P_2^{2t}S_2$, $P_3^{2b}P_3^{2t}P_2$, $P_3^{2b}P_3^{2t}S_2$, $P_2^{3b}P_2^{3t}P_2$, $P_2^{3b}P_2^{3t}S_2$ and the multiples of $P_2^{2b}P_2^{2t}$, $P_3^{2b}P_3^{2t}$, $P_2^{3b}P_2^{3t}$ are identified on the seismogram of Nodal Point 192. The arrivals, $P_2^{3t}P_2^{2t}P_1'$, $P_2^{3t}P_2^{2t}S_1'$, $S_2^{3t}S_2^{2t}S_1'$, $P_3^{2b}P_3^{2t}P_1'$, $P_3^{2b}P_3^{2t}S_1'$ and $S_3^{2b}S_3^{2t}P_1'$ are identified on the seismogram of Nodal Point 150. Nodal Point 108 and 66 are located in the weathering layer, only the arrival of $P_2^{3t}P_2^{2t}P_1'$ is shown. In Figure 15 a_1' and a_2', the wave in each seismogram with a period very close to 1.6 milliseconds as marked by "A" for Nodal Point 192 in the time interval of 6.8 milliseconds to 8.4 milliseconds, is identified as $P_JP_2^{3b}P_2^{3t}P_JP_2^{3t}$, a wave traveling periodically from the bottom end-face of the cavity, through the vertical face of the cavity to the top end-face of the cavity. In Figure 15 a_3', on the seismogram of Nodal Point 192, 150, 108, and 66, the wave with a period close to 5 milliseconds as marked "B" on 192 in the time interval of 6 milliseconds and 11 milliseconds is identified as $P_3^{2b}P_3^{2t}$ with a velocity of the filled drilling hole. In Figure 15 a_1', a_2', and a_3', the form of an input step pulse is well preserved in each seismogram, the amplitudes of the vertical displacement are larger than these of the radial displacements. The arrivals of S_2^{3t} on the seismogram for Nodal Point 192 in Figure 15 a_1', a_2', and a_3' are well identifiable.

Line G

Figure 16 shows synthetic seismograms of the radial displacement U_r and the vertical displacement U_z of Line G at Nodal Point 191, 170, 149, 128, 107, 86, and 65. For Model III, Nodal Point 191 is in the half-space, 170 in the layer interface, and 149, 128, 107, 86, and 65 in the weathering layer. The locations of these nodal points are along the Line G as shown in Figure 7. The locations of every nodal point along Line G are very close to the locations of nodal points along Line F. Line F is in the same direction but with a distance of 0.5 feet away from Line G. The wave forms of the radial displacements at Nodal Point 191, 149, 107, and 65 in Figure 16 a_1, a_2, and a_3 are very similar to these of the radial displacement at Nodal Point 192, 150, 108, and 66 as shown in Figure 15 a_1, a_2, and a_3, except the amplitudes of the radial displacement for Nodal Point 192, 150, 108, and 66 are smaller than these for Nodal Point 191, 149, 107, and 65. There are high frequency component responses observed at Nodal Point 170, 128, and 86. In examining the configuration of the finite element mesh around Nodal Point 149, 170, and 191, as shown in Figure 5, these high frequency components may be resulted from the different arrangements of the finite element mesh at Nodal Point 170 and Nodal Point 191 as shown in the following diagram:

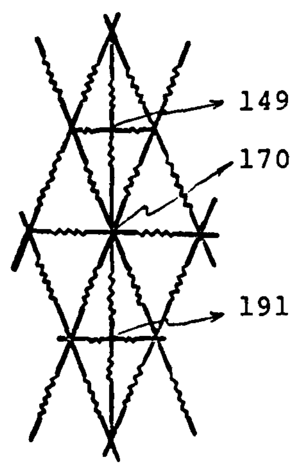

So that Nodal Point 170 responses to a high frequence radial displacement more efficiently than Nodal Point 191 or 149. At Nodal Point 170, it can be viewed as if two horizontal springs connected with two adjacent nodal points, contrarily to that at Nodal Point 191, there are as if four diagonal springs intersected at the Nodal Point.

In Figure 16 a_1' and a_2', the arrivals of the waves P_2^{3t}, S_2^{3t}, P_2^{3b}, S_2^{3b}, $P_2^{3t}P_2^{3b}P_2^{3t}$, $P_2^{3t}P_2^{3b}P_2^{3t}S_2$, and $P_JP_2^{3b}P_2^{3t}P_JP_2^{3t}$ and the multiples of $P_2^{3t}P_2^{3b}P_2^{3t}$, $P_2^{3t}P_2^{3b}P_2^{3t}S_2$, and $P_JP_2^{3b}P_2^{3t}P_JP_2^{3t}$ are identified on the seismograms for Nodal Point 191, 170, 149, 128, 107, 86, and 65. In Figure 16 a_3', for Model III, the locations of Nodal Point 191, 170, 149, 128, 107, 86, and 65 are in different regions,therefore, the arrivals of the waves are identified each Nodal Point by each Nodal Point. The arrivals of waves P_2^{3t}, $P_2^{2b}P_2^{2t}P_2$, $P_2^{3b}P_2^{3t}P_2$, S_2^{3t}, $S_JS_2^{3t}$, $P_2^{3t}P_2^{2t}S_2$, $S_2^{3b}S_2^{3t}P_2$, $S_2^{2b}S_2^{2t}S_2$, $S_2^{3b}S_2^{3t}S_2$, $P_2^{3t}P_2^{2t}P_3$, $P_2^{3b}P_2^{3t}P_3$, $P_3^{3t}P_3^{2t}P_2$ $P_3^{2b}P_3^{2t}S_2$, S_3^{3t}, $S_2^{2b}S_2^{2t}P_3$, $P_2^{3t}P_2^{2t}S_3$, $P_2^{3b}P_2^{3t}S_3$, $P_3^{3t}P_3^{2t}P_3$, $P_2^{3b}P_2^{2t}S_3$, $S_2^{3b}S_2^{3t}S_3$, $S_2^{3b}S_2^{2t}S_3$, $P_3^{3t}P_3^{2t}S_3$, $S_3^{3t}S_3^{2t}P_2$, $S_3^{3t}S_3^{2t}S_2$, $S_3^{2b}S_3^{2t}P_3$ are identified for Nodal Point 191. The arrivals of P_2^{3t}, P_2^{3b}. S_2^{3t}, $P_2^{3b}P_2^{3t}P_2$, $P_2^{3b}P_2^{3t}S_2$, S_2^{3b}, P_3^{3t}, $P_2^{3b}P_2^{2t}P_3$, $S_2^{3b}S_2^{3t}P_3$ are identified for Nodal Point 170. The arrival, $P_2^{2b}P_2^{2t}P_1'$, $S_2^{2b}S_2^{2t}P_1'$, $P_2^{2b}P_2^{2t}P_3$, $P_2^{2b}P_2^{2t}S_1'$, and $S_2^{2b}S_2^{2t}S_1'$, $P_3^{3t}P_3^{2t}P_1'$, $P_3^{3t}P_3^{2t}P_3$, $P_3^{3t}P_3^{2t}S_1'$, $S_2^{3t}S_2^{2t}S_3$, $P_3^{3t}P_3^{2t}S_3$, $S_3^{3t}S_3^{2t}P_1'$, $S_3^{3t}S_3^{2t}S_1'$ are identified on the seismogram of Nodal Point 149. The arrivals $P_2^{3t}P_2^{2t}P_1'$, $P_2^{3t}P_2^{2t}S_1'$, $P_3^{3b}P_3^{2t}P_1'$, $P_3^{3t}P_3^{2t}P_3$, $P_3^{3t}P_3^{2t}S_1'$ are identified on the seismogram of 128... Only the arrival of $P_2^{3t}P_2^{2t}P_1'$ is clearly shown in the seismograms of Nodal Point 107, 86, and 65.

Because Nodal Point 191 is located right on the vertical interface of the filled drilling hole, the location is very sensitive to the motion on the top end of the cavity. The seismogram of Nodal Point 191 in Figure 16 a_3' shows that the high frequency components are superimposed on the long period components. These high frequency components with a period of about 0.5 milliseconds as marked by "A" on the seismogram of Nodal Point 191 in a_3' appear in the time interval between 10.9 milliseconds and 11.4 milliseconds. As the traveling path of P_J is 0.5 foot, and the top end-face of the cylindrical cavity is in contact with the filling of the drilling hole (a P velocity of 1000 ft/sec), the high frequency components likely are excited by P_J, traveling periodically on the top (or bottom) end-face of the cylindrical cavity. On the other hand, the long period component in all the seismograms in a_3' can be identified as $P_3^{2b}P_3^{2t}$, traveling periodically between the top and bottom rims as designated by 2t and 2b along the vertical interface of the drilling hole with a P wave velocity in the drilling hole of 1000 feet/sec and a period of 5 milliseconds. Nodal Point 149, 128, 107, 86, and 65 are located in the weathering layer, therefore, most of the high frequency response are apparently filtered out.

<u>Line H</u>

Figure 17 shows the responses of both the radial component and the vertical component at Nodal Point 190, 140, 106, and 64 along Line H. All the nodal points along this line are on the top region of the cylindrical cavity source. For Model III, these points are located in the filled drilling hole. Similar to that of Line G and Line F, a beating phenomenon is again observed in the time history of the radial displacement at these four nodal points along Line H for Model I and II. In the present case, these beats have much smaller amplitude modulations than these of Lines F, and G. As nodal points along Line H is located close to the axis of the cylindrical cavity, therefore, the radial motion of the top end-face of the cavity contributes to the vertical displacement significantly. The high frequency response due to the radial motion of the end-faces of the cavity is clearly observed on the synthetic seismograms. The wave, $P_J P_2^{3b} P_2^{3t} P_J P_2^{3t}$, is clearly identified in the seismogram of the vertical displacement U_z, which are very similar to that of $P_J P_2^{3b} P_2^{3t} P_J P_2^{3t}$ in Figure 15, and Figure 16. For Model III, Figure 17 a_3', because the nodal points are located in the drilling hole, which is filled with unconsolidated material, the amplitudes of both the radial and the vertical displacements are very much amplified, for instance an extremely large amplitude wave is observed at Nodal Point 190. The wave is attenuated rapidly as the observation point moves away from the cavity (see both in Figure 17 a_3 and a_3'). In Figure 17 a_3, at Nodal Point 148, the waves $P_3^{2b} P_3^{2t}$, and $P_2^{2b} P_2^{2t}$ apparently travel back and forth periodically along the vertical interface between the two rims as designated by 2t and 2b. At Nodal Point 148, 106 and 64, the most pronounced arrivals are indicated on the seismograms. The arrival of $P_3^{3t} P_3^{2t} P_2^{2t}$ with a period of about 5 milliseconds is indicated on each seismogram of Nodal Point 148, 106, and 64.

Line I, J, K

Figures 18, 19, and 20 give synthetic seismograms of the radial and the vertical displacements at the nodal points along Line I, J, and K. These three lines are located in the region bellow the bottom of the cavity. Geometrically the locations of these nodal points along these three lines are symmetric to those of nodal points along Line F, G, and H. For the whole-space case, the symmetrical responses of the radial and vertical displacements are displayed in a_1 and a_1' of Figure 18, 19, and 20, and can be compared with the results of a_1 and a_1' of Figure 15, 16, and 17 to be exactly identical. For the half-space case as compared with the whole-space case, the only difference is the arrival of additional reflected wave $P_2^{3t}P_2$ from the surface of the half-space as indicated on each seismogram for each nodal point as shown in a_2 and a_2' of Figure 18, 19, and 20. For Model III, the layered half-space case, the synthetic seismograms in general are quite similar in appearance as these for the whole-space case, except the additional diffracted arrivals.

All the above interpretations are limited to the arrivals in the time interval of 0 to 15 milliseconds.

7. CONCLUSION

The present study has demonstrated the possibility of obtaining the numerical solutions for a finite length energy source within a half-space, and a layered half-space by means of the finite element method. The significant results regarding the displacement field due to a finite cylindrical cavity source in a whole-space, a half-space, and a layered half-space, may be summerized as follows:

1). For the observation points inside the medium, the reflected waves from the surface boundary of the half-space for the velocity of the medium assumed does not seem to have significant effects on the amplitude of the wave.

2). The amplitudes of both the vertical and radial displacements at the observation point on the surface of the half-space model are much larger than these at these corresponding observation points in the whole-space.

3). The wave forms of the transient response strongly depend on the dimensions of the finite cylindrical cavity, i.e. the radius of the cavity, and the length of the cavity.

4). The type of P wave traveling periodically from the top rim to the bottom rim of the cavity along the vertical interface of the cylindrical cavity and the type of P wave traveling periodically from the bottom (or the top) face of the cavity with a motion described by the Bessel function order zero, through the vertical face of the cavity, to the top (or the bottom) face of the cylindrical cavity also with a motion described by the Bessel function order zero are dominanted in all three models.

5). There are no vertical displacements U_z at any point along the middle plane, which is symmetrical with respect to the two end faces of the cylindrical cavity, in Model I - a whole-space.

6). For Model III - a layer half-space, the long period wave is clearly identifiable, traveling periodically along the vertical face of the drilling hole between the two rims, the rim of the contact at the layer-interface and the top rim of the cylindrical cavity.

7). All the high frequency arrivals are filtered out in the seismograms at those observation points located in the weathering layer. The weathering layer behaves as a low pass filter.

8). The shape of the input forcing function is will preserved on each seismogram of the vertical displacement U_z but not the radial idsplacement U_r.

9). The beat phenomenon is clearly observed on the radial displacements of these observation points located in the upper region of the cavity source.

10). The amplitudes of both the radial and vertical displacements are extremely large at these observation points close to the cavity in the filled drilling hole, but are attenuated rapidly as the observation point moves away from the cavity.

11). Shear wave can be generated from the finite length cavity source with only normal stresses applied on the surfaces of the cavity. The arrival of shear waves are clearly identifiable at these observation points in the region along the diagonal line of the cylindrical cavity.

Medium	Density (gm/cm^3)	Poisson's Ratio	Young's Modulus ($dynes/cm^2$)	V_p (cm/sec)	V_s (cm/sec)
1	2.2	0.35	0.50939×10^{11}	60960	29284
2	2.5	0.25	0.48387×10^{11}	152400	87988
3	2.0	0.40	0.86710×10^{11}	30480	12443

Table 1. Model Parameters

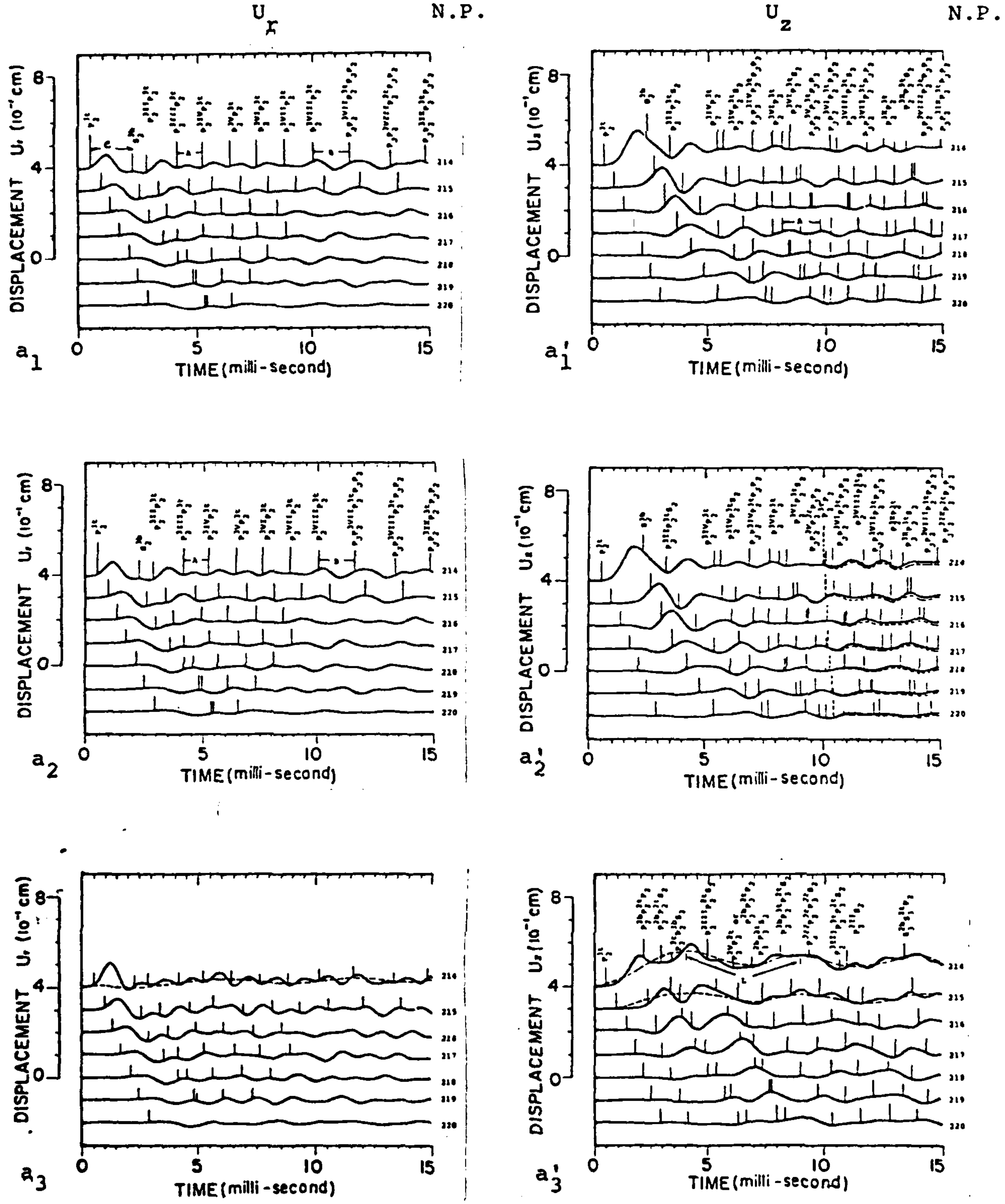

Figure 10. Synthetic seismograms of both the radial and vertical displacements U_r and U_z of the transient response of Model I, II, and III along LINE A as show in Figure 7.

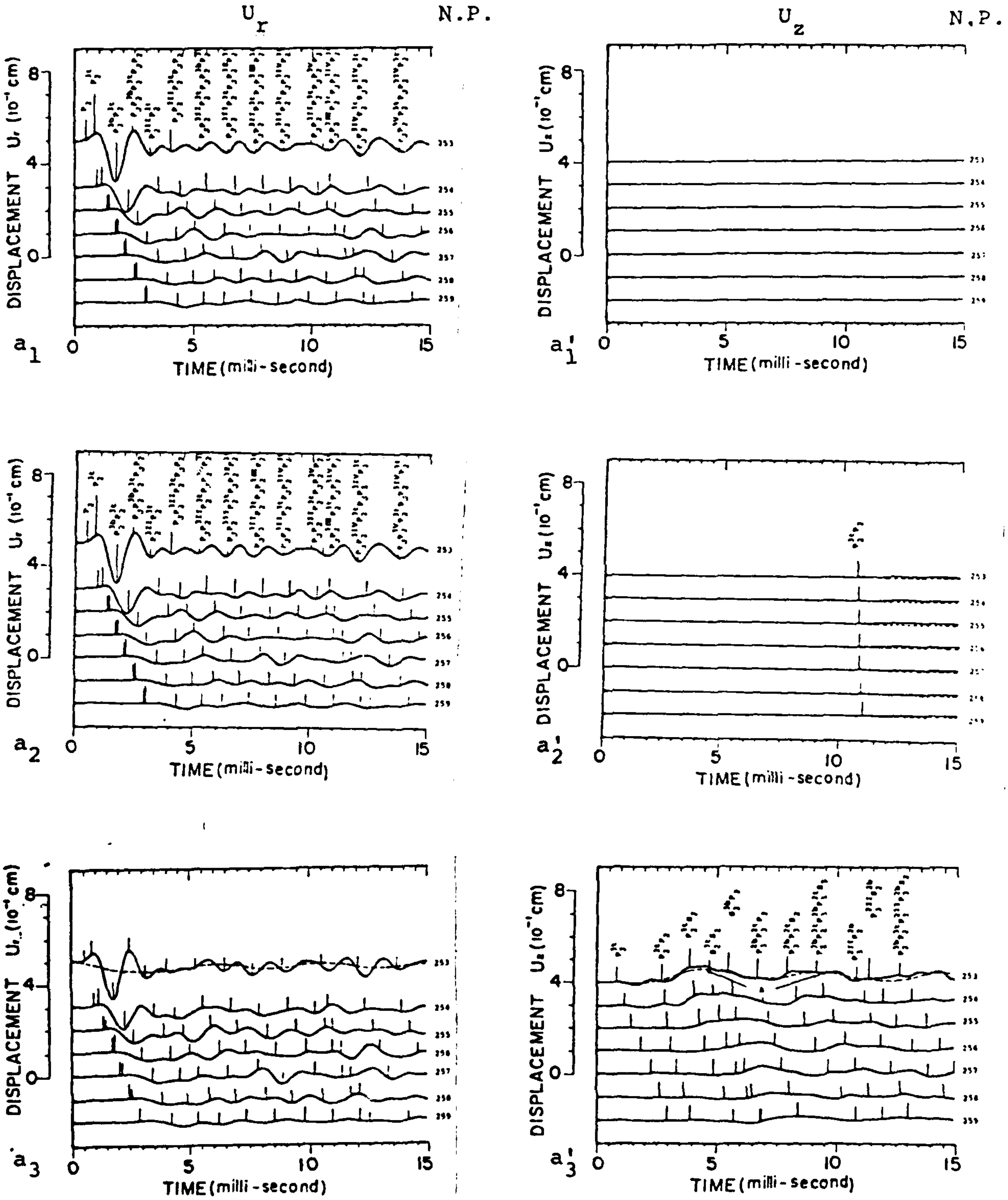

Figure 11. Synthetic seismograms of both the radial and vertical displacements U_r and U_z of the transient response of Model I, II, and III along LINE B as show in Figure 7.

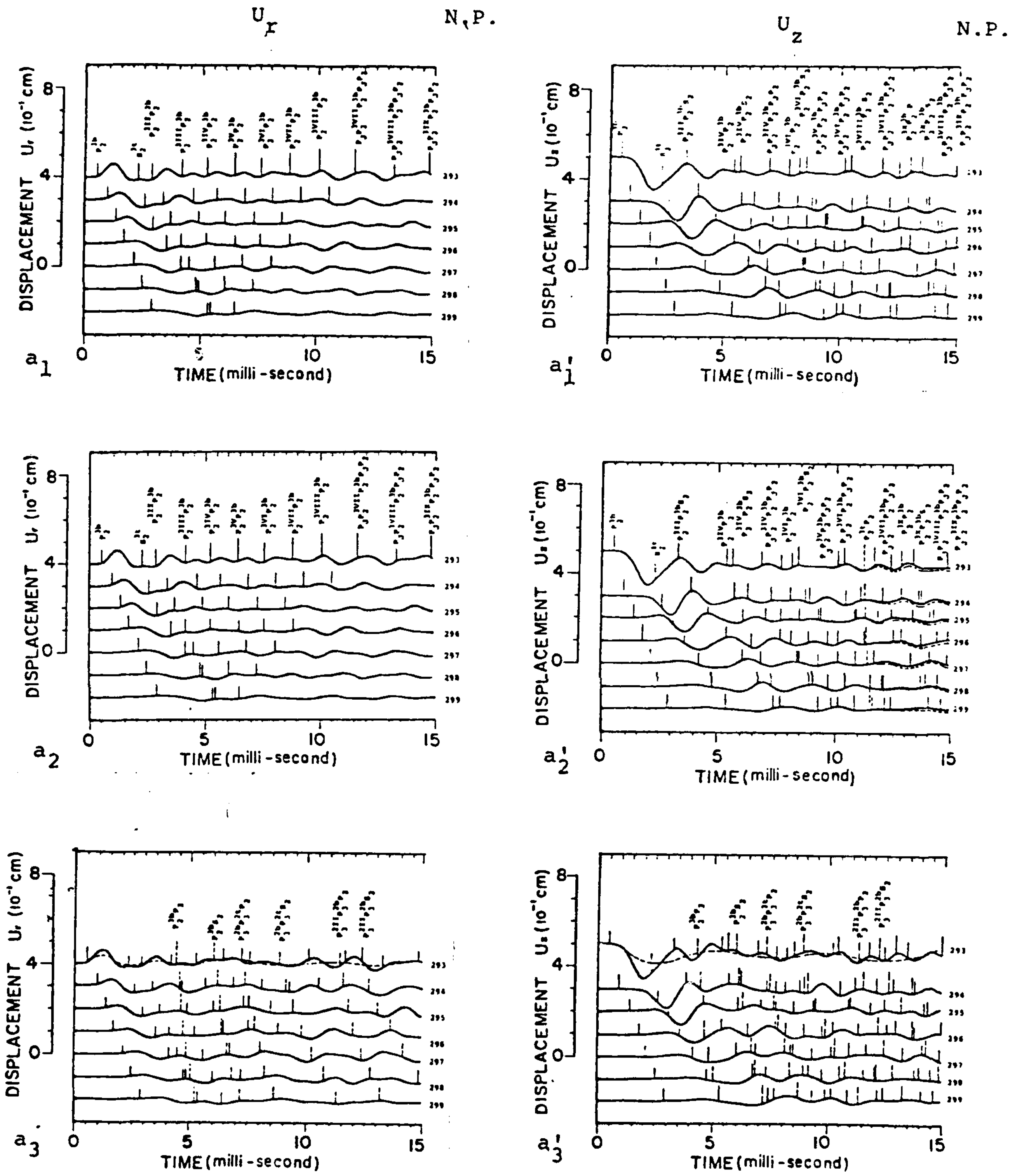

Figure 12. Synthetic seismograms of both the radial and vertical displacements U_r and U_z of the transient response of Model I, II, and III along LINE C as show in Figure 7.

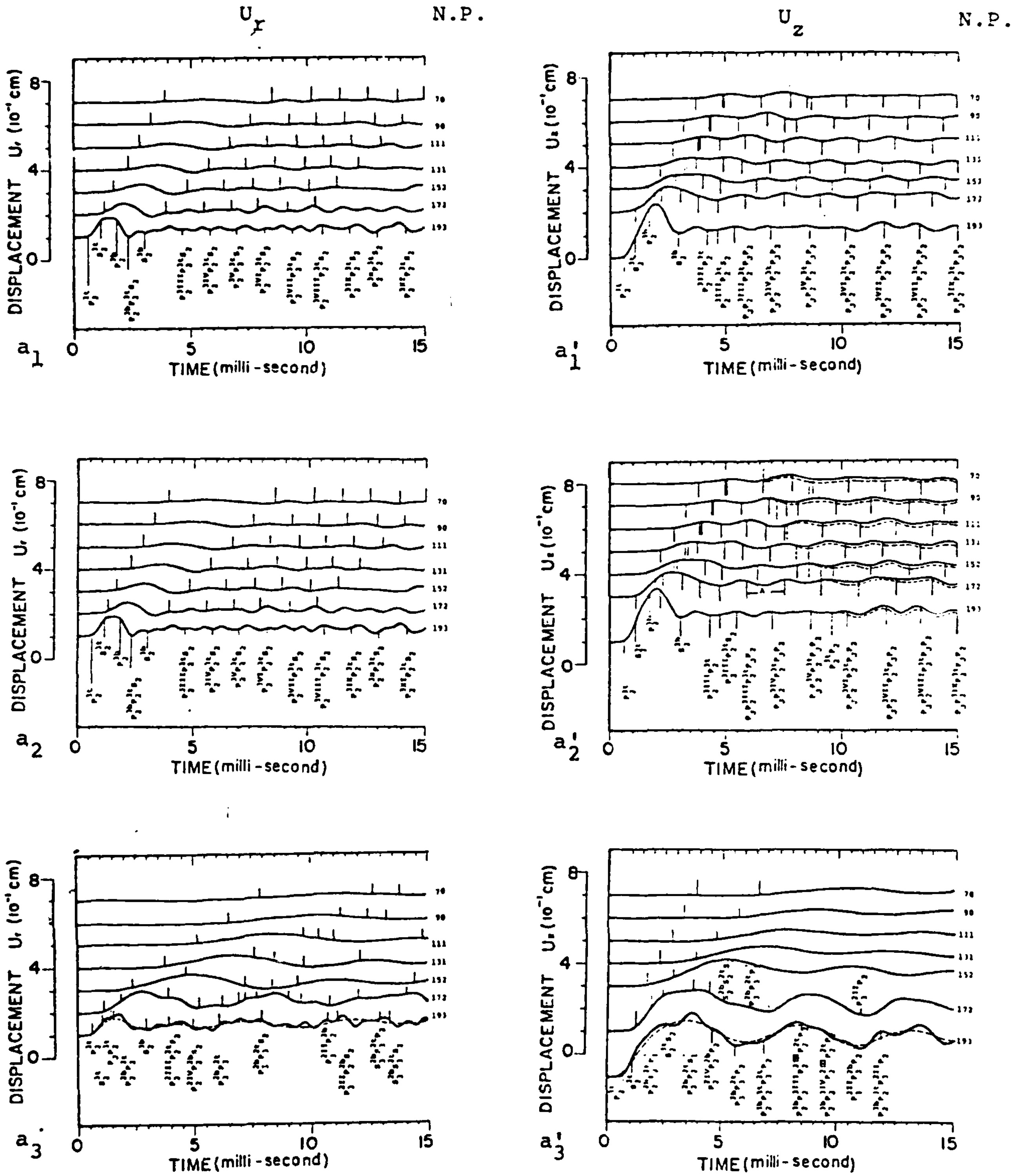

Figure 13. Synthetic seismograms of both the radial and vertical displacements U_r and U_z of the transient response of Model I,II, and III along LINE D as show in Figure 7.

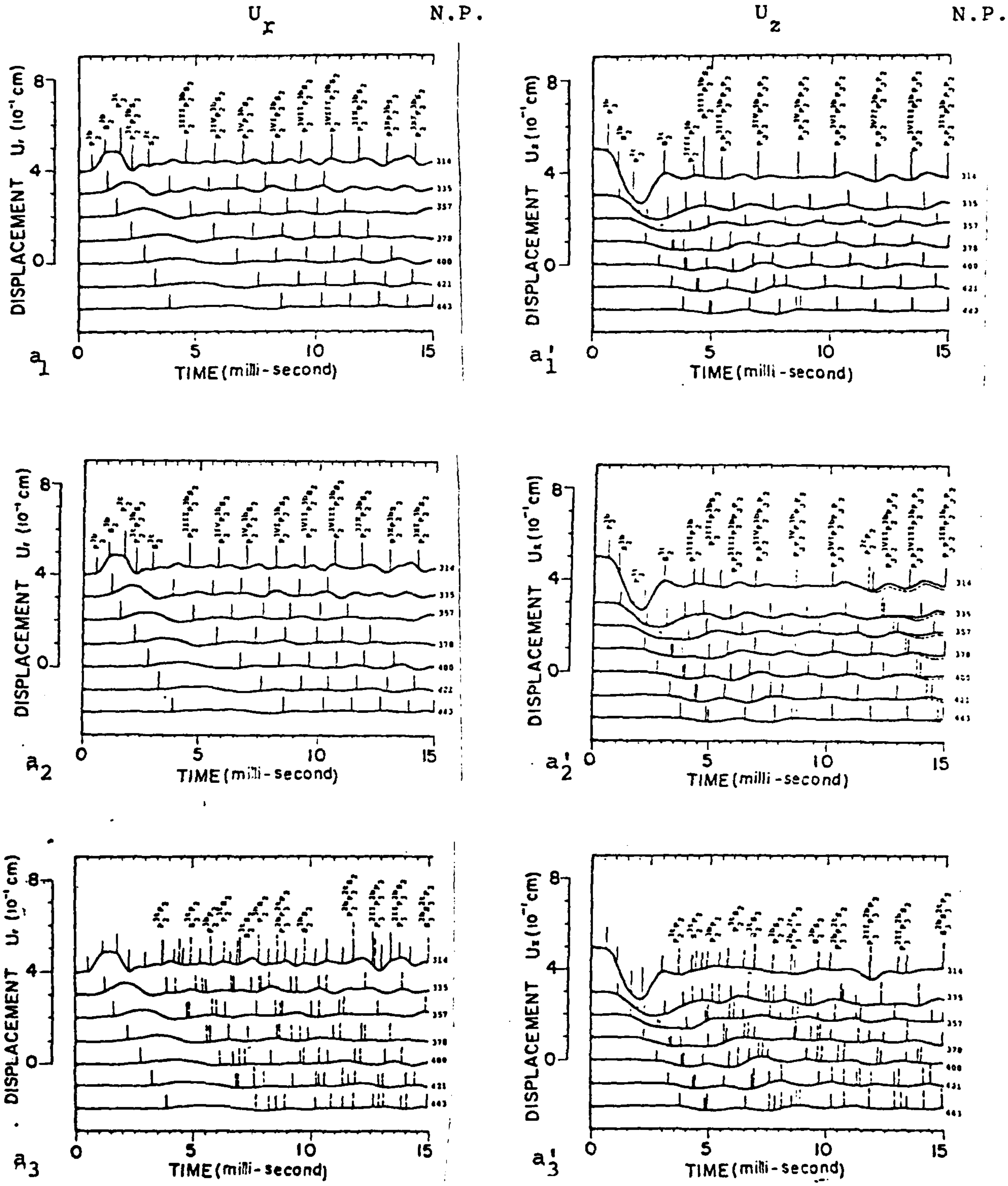

Figure 14. Synthetic seismograms of both the radial and vertical displacements U_r and U_z of the transient response of Model I, II, and III along LINE E as show in Figure 7.

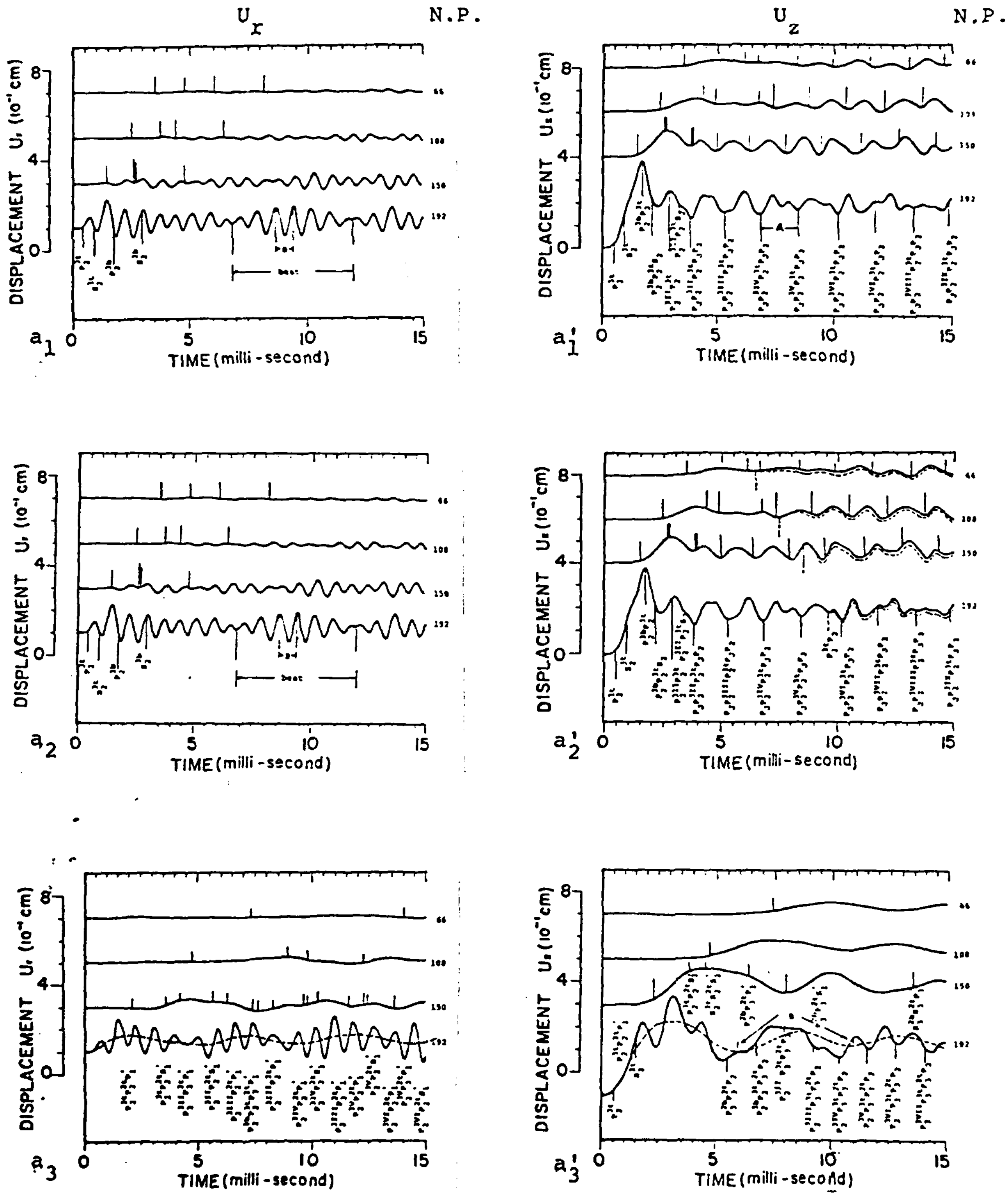

Figure 15. Synthetic seismograms of both the radial and vertical displacements U_r and U_z of the transient response of Model I, II, and III along LINE F as show in Figure 7.

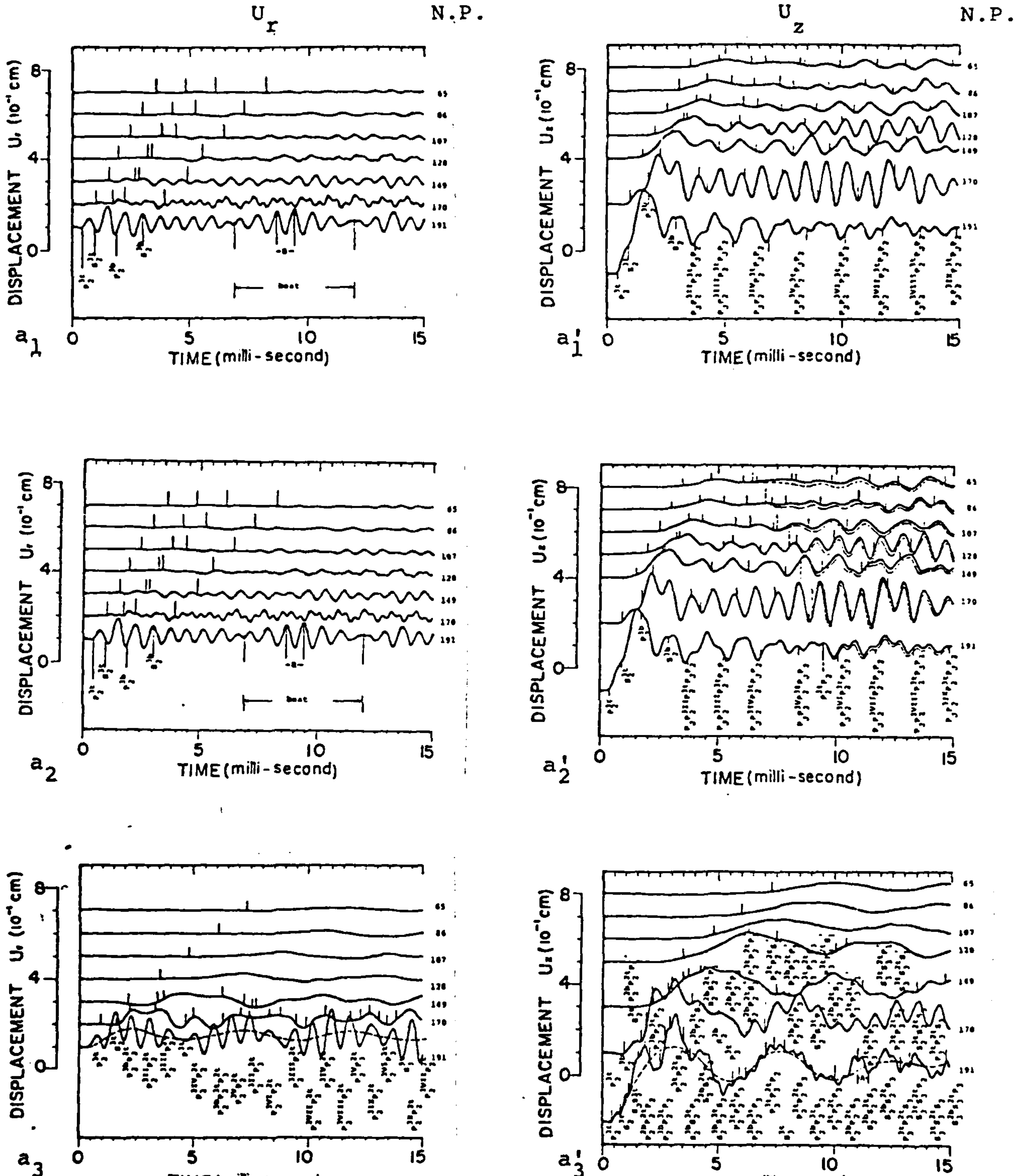

Figure 16. Synthetic seismograms of both the radial and vertical displacements U_r and U_z of the transient response of Model I, II, and III along LINE G as show in Figure 7.

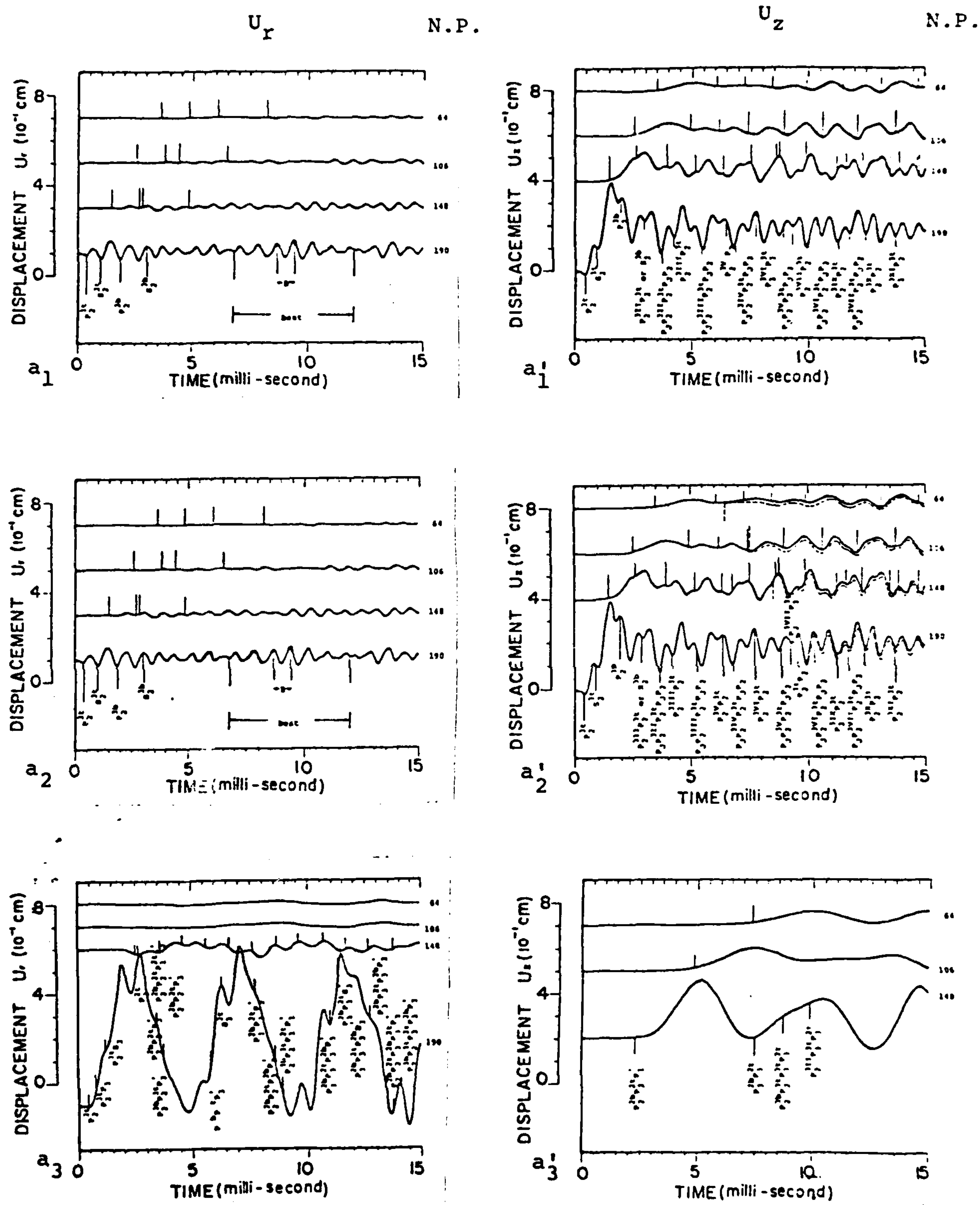

Figure 17. Synthetic seismograms of both the radial and vertical displacements U_r and U_z of the transient response of Model I, II, and III along LINE H as show in Figure 7.

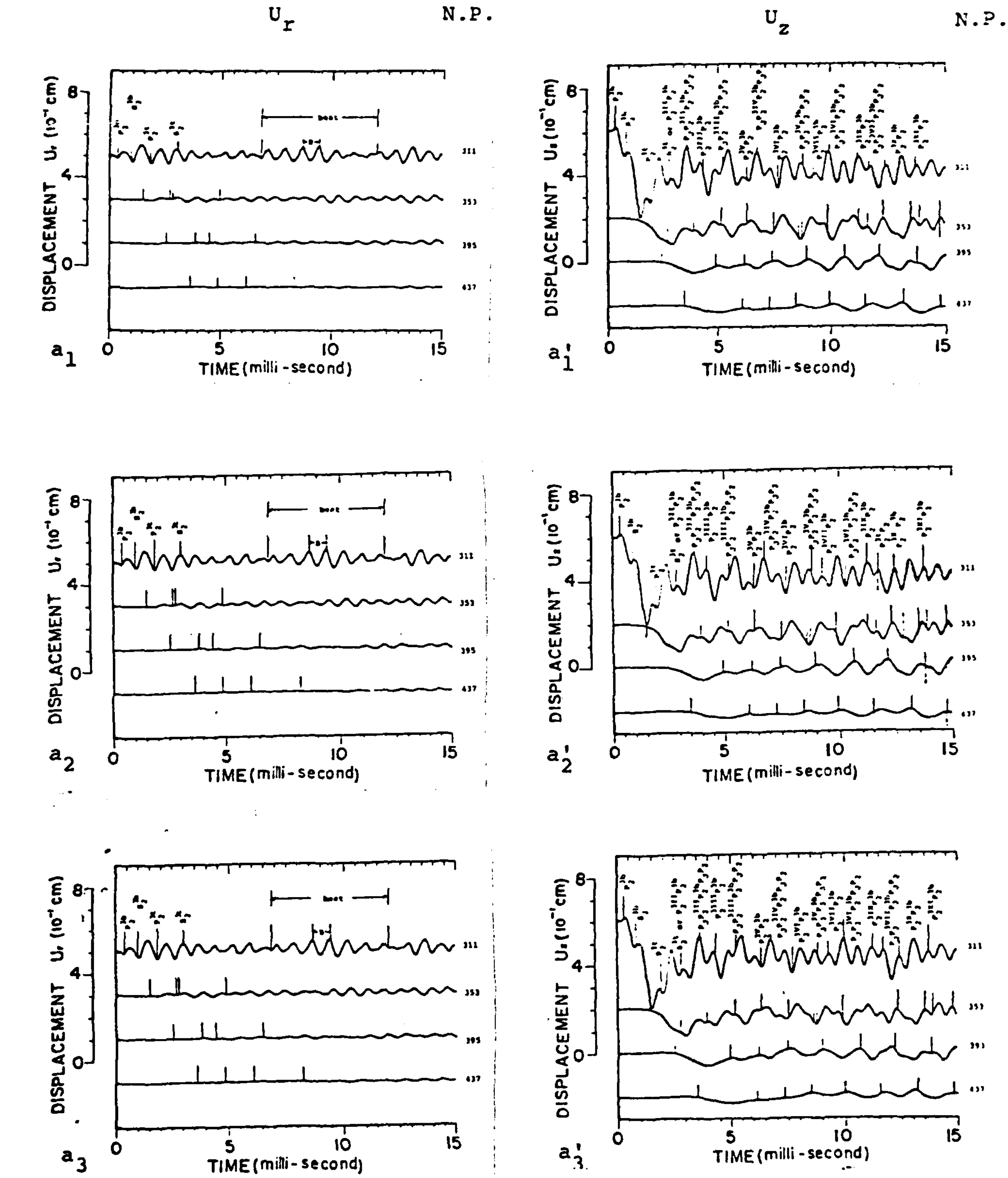

Figure 18. Synthetic seismograms of both the radial and vertical displacements U_r and U_z of the transient response of Model I, II, and III along LINE I as show in Figure 7.

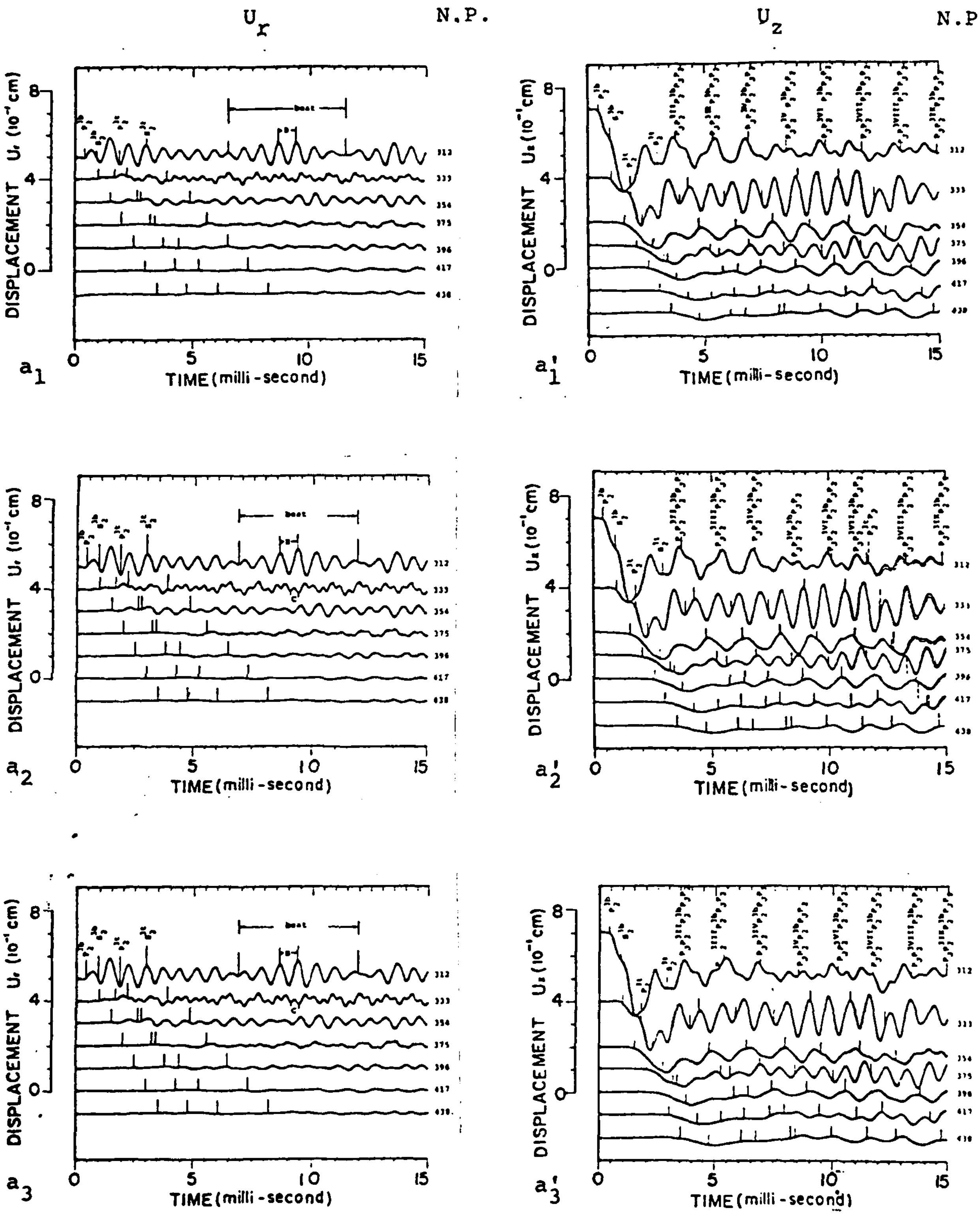

Figure 19. Synthetic seismograms of both the radial and vertical displacements U_r and U_z of the transient response of Model I, II, and III along LINE J as show in Figure 7.

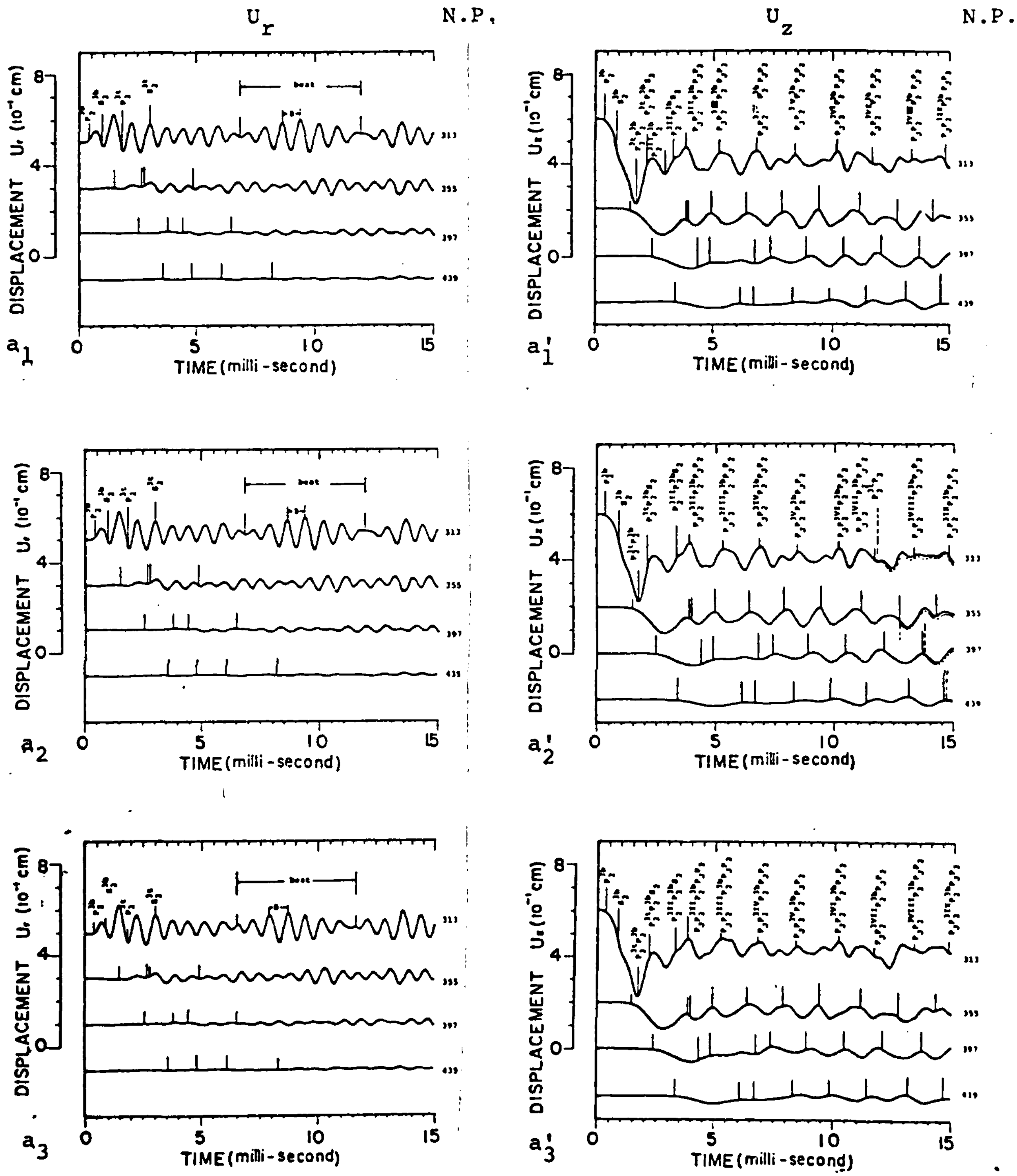

Figure 20. Synthetic seismograms of both the radial and vertical displacements U_r and U_z of the transient response of Model I, II, and III along LINE K as show in Figure 7.

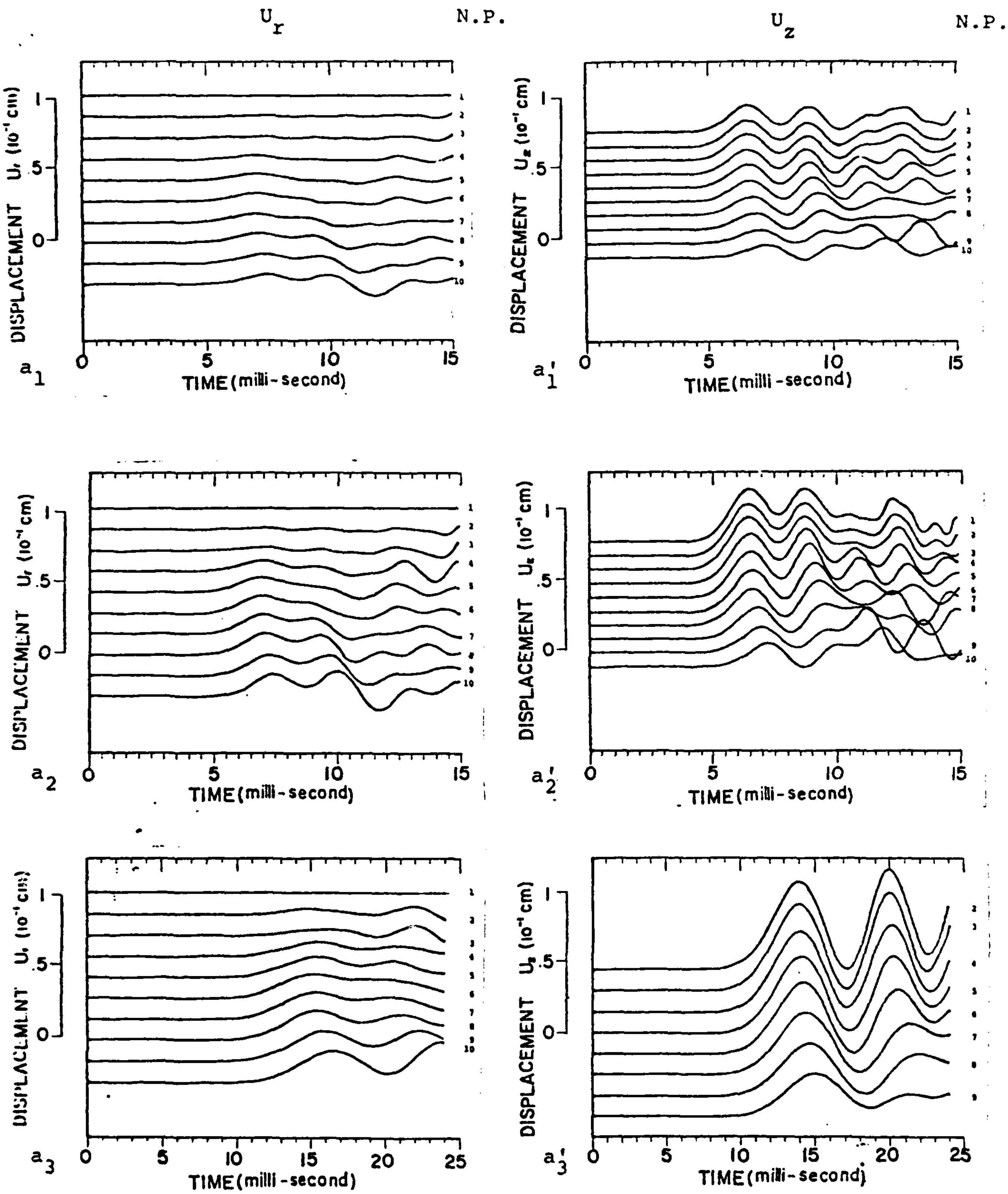

Figure 21. Synthetic seismograms of both the radial and vertical displacements U_r and U_z of the transient response of Model I, II, and III along LINE L as show in Figure 7.

REFERENCES

Baylor, J.L., Bieniek, J.L., and Wright, J.P., 1974, A 3-D Finite Element Code for Transient Nonlinear Analysis, Interim Report of Weidlinger Associates, Consulting Engineers, N.Y., N.Y.

Fung, Y.C., 1965, Foundations of Solid Mechanics, Prentice-Hall, Inc., Englewood Cliff, N.J.

Kuo, J.T., Chen, K.H., Teng, Y.C., Gong, C., 1975, Numerical and Analytical Solutions to Elastodynamic Problems, Final Report, AFCRL-TR-75-0428.

Krieg, R.D., 1970, Unconditional Stability in Numerical Time Integration Methods, Sandia Laboratories Report SL-DR-70-400.

IV. THREE DIMENSIONAL EXPERIMENTAL STUDY OF ACOUSTIC-ELASTIC WAVE SCATTERING AND DIFFRACTION

Table of Contents

ABSTRACT

Three dimensional model experiments are performed to study the acoustic-elastic wave scattering and diffraction by a vertical elastic cylinder immersed in a fluid due to a trainsient acoustic point source. The direct, transmitted and diffracted waves in the volume exterior to the cylinder are clearly observed. Particularly, the diffracted longitudinal, transverse, Rayleigh and acoustic (creeping) waves which propaage near the cylindrical interface are observed together with the waves transmitted through the cylinder. The moveout of the diffracted waves for non-symmetric source-receiver configurations is shown. Splitting of each diffraction at non-symmetric receiver positions is verified and explained as a result of diffracted energy propagating in both directions around the cylinder. Helical diffracted waves propagating up and down the cylinder, as predicted by theory, are verified for the first time.

Three dimensional ray path and wavefront equations are given for all of the waves encountered in this experiment. The amplitude spectra maxima are shown to be related to the relative arrival times between the various events observed on the data trace. Envelope dectection and

homomorphic filtering are applied and shown to provide information on the arrival times and on the temporal duration of the observed transmitted and diffracted events.

List of Figures

INTRODUCTION

Bodies possessing a cylindrical shape are of considerable importance in the theory of scattering and diffraction of acoustic and elastic waves. Many man-made structures, such as, mine shafts and drifts, fiber reinforced materials, underground and ocean-bottom pipes, cast metals containing inclusions or imperfections and missile silos, as well as such natural formations like salt domes, mineral deposits, igneous intrusives, caves, sink holes, seamounts and coal gasification cavities may be approximated geometrically by a cylindrical shape. Since the analytical solution to the three dimensional scattering and diffraction of an elastic cylinder embedded in either an elastic or an acoustic medium due to a transient point source of energy is intractable, the alternative method of an experimental model study provides a means of obtaining a physical understanding of the problem. Moreover, an experimental study may provide a means to verify that the waves predicted by two dimensional theory do exist in both two and three dimensions.

The basic physics of scattering and diffration at various discontinuities is dicsussed by Keller(1958, 1962), Keller and Karal(1964) and Kouyoumjian (1975). Excellent reviews of the scattering and diffraction of fluid-loaded structures are provided by Uberall and Hwang(1976), Uberall(1973) and Neubauer(1973). These reviews are limited to discussing the analytical solutions to simple acoustic and elastic problems by the method of integral transforms and they discuss the use of surface waves propagating on plane and curved boundaries. The principal analytic solutions which have been obtained, only beginning to scratch the surface of acoustic and elastic scattering and diffraction by cylindrical and spherical bodies, are for sound pulses diffracted by a circular cylindrical cavity(Chen and Pao, 1977), for sound pulses diffracted by a rigid and a soft cylinder embedded in a solid(Gilbert,1960 and Gilbert and Knopoff, 1959), for three dimensional acoustic wave scattering and diffraction by an open-ended vertical soft cylinder in a half-space(Teng, Kuo and Gong,1975) and for the scattering and diffraction of an infinite cylindrical cavity in an elastic medium due to an impulsive elastic P wave source(Hwang and Kuo, unpublished). These solutions provide a basis for the understanding of the manner in which incident impulsive energy is scattered and diffracted by cylinders, but they fall short of the total problem of showing the interaction of the transmitted waves through an elastic cylinder with the diffracted waves around the cylinder. Failure occurs because the boundary conditions used prohibit energy from being refracted into the cylinder. Incorporation of transmission into the problem leaves a characteristic equation to solve whose roots are extremely difficult to extract. Except for the solutions by Teng and Kuo(1975) and Hwang and Kuo(unpublished), the previously mentioned solutions are for two dimensional problems.

Experimental model studies have provided the verification of the existence of circumferential diffracted creeping waves and of diffracted Rayleigh waves (Barnard and McKinney, 1961, Faran, 1951, Bunney, Goodman and Marshall, 1969, Harbold and Steinberg, 1969, and Neubauer, 1968). These experiments were specifically designed to study individual diffractions by using a bistatic source and receiver configuration with the transducers oriented to the cylindrical surface at the critical angle at which the diffracted wave to be verified is excited. Through this orientation the desired diffraction event is enhanced while all of the other arriving events are less enhanced in order that they will not interfere and confuse the verification of the diffraction. Except for the work of Steinberg(1969), all of the experiments were performed for two dimensional cylinders,i.e. the source and receiver were kept coplanar. Another drawback of the previous experiments designed to study diffractions on cylinders is that long monochromatic tonebursts were used as sources which were long compared to the characteristic dimension of the cylindrical scatterer. Sachse(1974), Sachse and Chian(1974) and Pao and Sachse(1974) used a short transient pulse to study backscattered and diffracted ultrasonic pulses from elastic and fluid cylindrical inclusions in a solid medium. Verification of a circumferential diffracted S wave propagating at a fluid-solid interface for the case of a fluid inclusion in a solid medium was obtained.

This thesis addresses the acoustic-elastic scattering and diffraction of an infinite elastic cylinder immersed in a fluid medium due to a simulated transeint point source.

ACOUSTIC-ELASTIC EXPERIMENTAL MODEL

Model System

The experiments are performed in an acoustic model tank which measures 24' long by 18' wide by 12' deep (Figure 1). By suspending the source, the receiver and the elastic cylindrical model in the center 3 sq. ft. of the tank, the sides and the bottom are far removed to prevent the recording of unwanted reflections. In the present experiment, using a rectangular coordinate system, the source and the receiver can be moved in both directions along a system of rails using the position of the cylinder as the origin. For the cylindrical system, the source transducer is used as the origin and the receiver is rotated about the source at a radius r. In both systems the vertical movements are achieved by raising or lowering the transducers attached to the rods. Both the source and the receiver can be rotated vertically and horizontally about their fixed positions in space to simulate a point source or a line source. Through the rotation of the source in a horizontal plane in degree increments and summing the recorded data traces for each increment, a line source can be simulated because a narrow beam transducer is used as the source. If, for

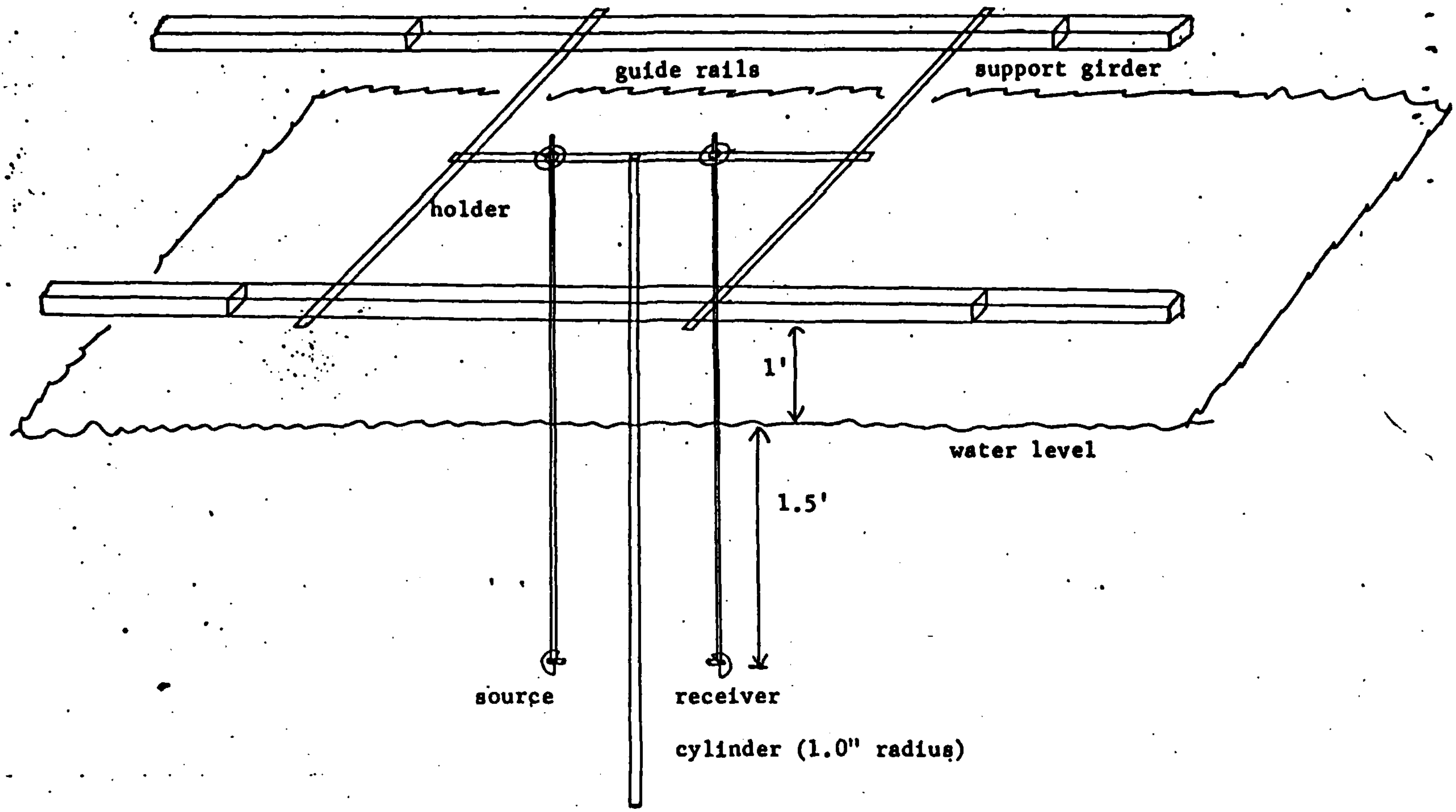

Figure 1. Acoustic model (not to scale)

each horizontal increment, the source is rotated vertically in equal increments and these data are summed, a point source is simulated.

The source and the receiver are suspended at a depth of one foot or greater below the free surface to eliminate unwanted reflections from the surface. A cylinder of 4.5 ft. in length is used. The source and the receiver are kept far enough from each end of the cylinder so that diffrations from the ends do not interfere with the arrivals of primary interest.

The source and the receiver used in the experiments are immersion transducers manufactured by Panametrics, Inc.. These transducers measure 1.25 in. in length and 0.625 in. in diameter. The element used is a 0.5 in. diameter PZT (Lead-Zirconium-Titanate) ceramic which is backed by a specially designed tungsten-doped epoxy resin. Figure 2b displays a typical source wavelet for this type of transducer in The pulse mode along with its amplitude and phase spectra as shown in Figure 2a. The pulse emitted from the transducer used as the source is short, approximately 2 μsec. duration, and the radiation patterns are about 10 db. down at 10° from the transducer axis creating a narrow directed beam of energy (Figure 3). The lack of significant ringing, as seen in the wavelet in Figure 2b, when the transducer is pulsed by a narrow, 1 μsec., high voltage(approximately 80 volt) pulse is obtained by highly damping the transducer using a tungsten-doped epoxy resin to back the PZT ceramic disk. This resin is

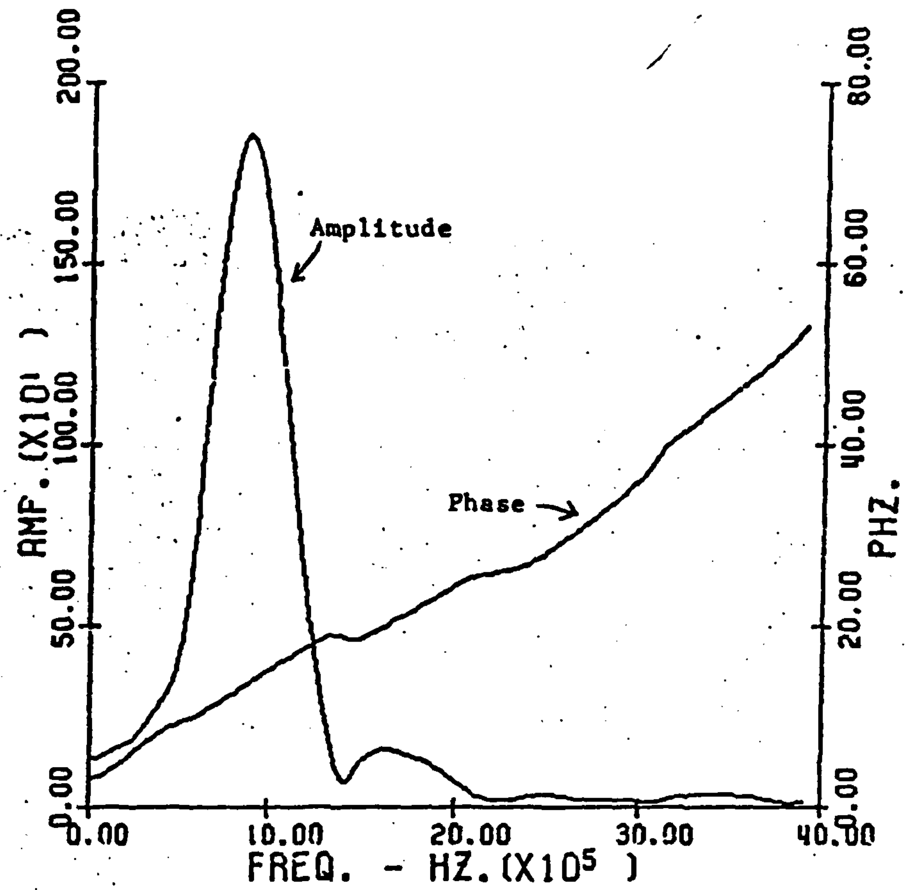

a) Source Spectrum

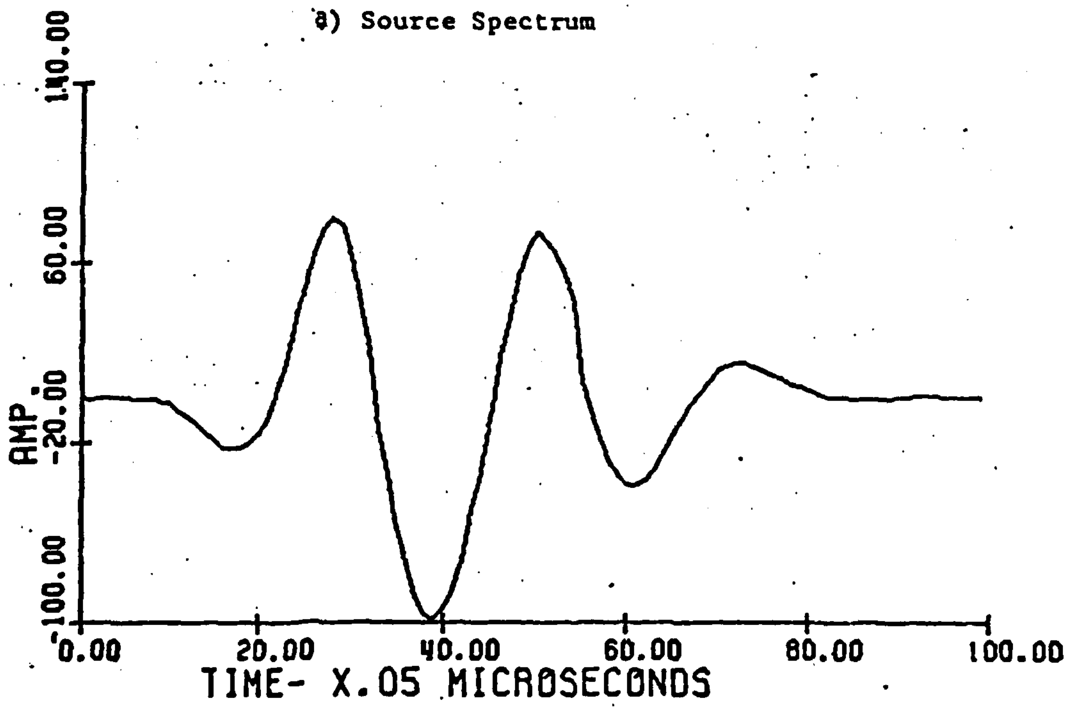

b) Source Wavelet

Figure 2

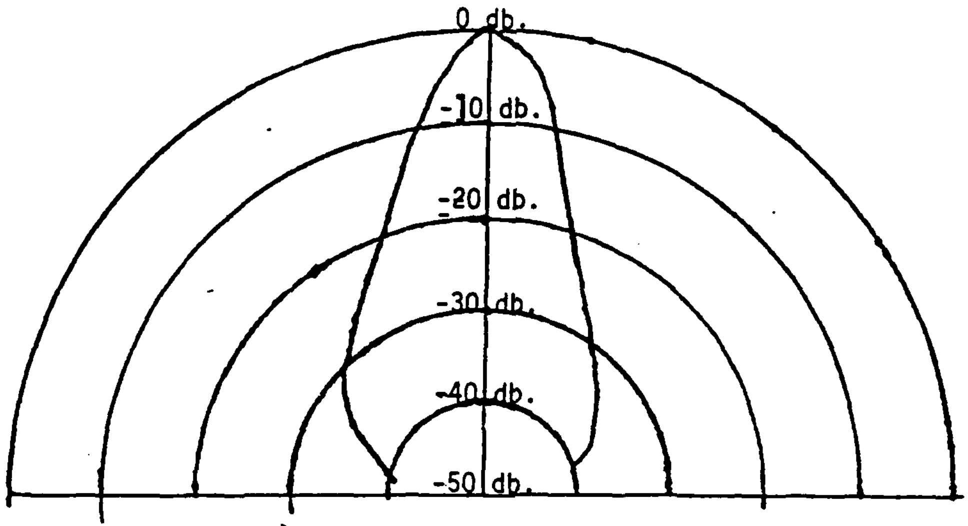

a.) Receiver Radiation Pattern

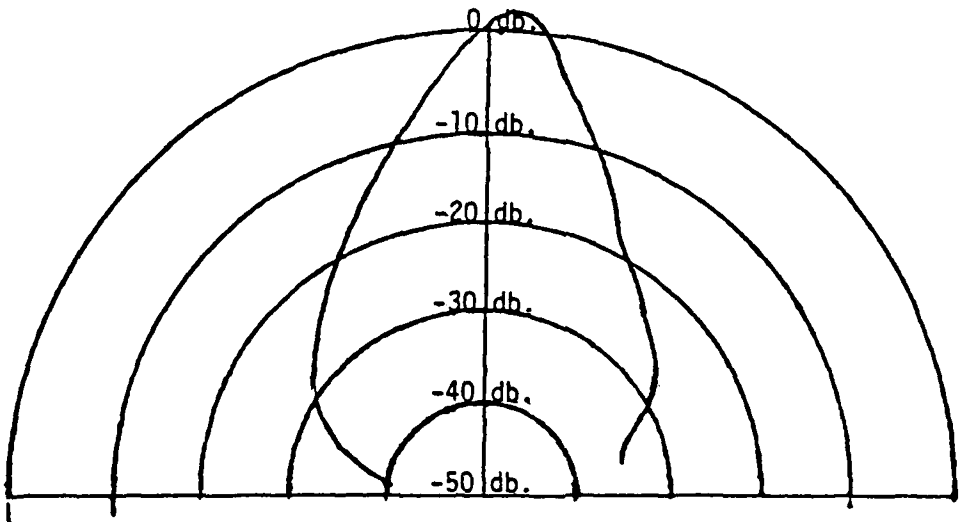

b.) Source Radiation Pattern

Figure 3

designed to match the impedance of the PZT ceramic allowing 100% of the energy to be transmitted at the back of the ceramic. Since the epoxy has a well determined velocity, by doping the epoxy with tungsten dust the density of the resin can be increased enough that the impedance of the resin matches the impedance of the PZT ceramic. However, the epoxy has a low Q which completely attenuates the signal transmitted at the back of the ceramic before it reaches the ceramic following reflection from the rear casing. These transducers were chosen specifically because they emitted a short almost symmetric pulse when used in the pulse mode. This type of pulse is desired because it allows greater resolution between arrivals.

Data Acquisition System

The experimental data acquisition system is shown in Figure 4. It uses an HP-214A pulse generator to pulse a Panametrics immersion transducer with a narrow, 1 μsec., high voltage pulse to provide a narrow, 2 μsec, source wavelet (Figure 2b). The received signal, which is scattered and diffracted from the cylinder model, is first received by a Panametrics immersion transducer, then it is pre-amplified, then amplified 20 db. by an HP-450A amplifier. It is then filtered by a 100 KHZ. high pass RC Rockland filter before it enters the Tektronix sampling unit for reduction to an analog signal compatible with the 8 bit A/D converter. Since the center frequency of the transducer pulse is in the megahertz range(see Figure 2b), a Tektronix

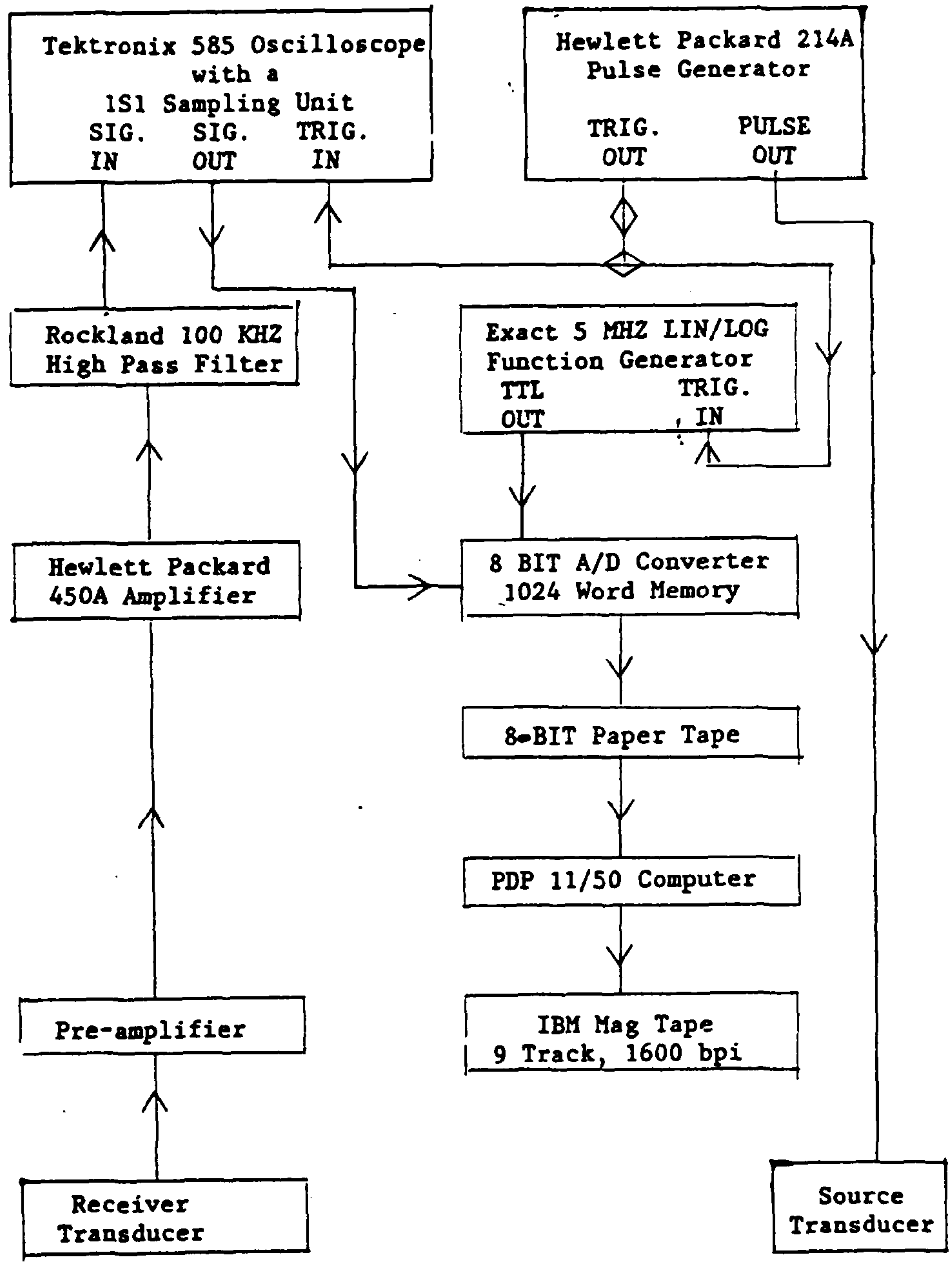

Figure 4 Data Acquisition System

585 oscilloscope with a 1S1 sampling unit plug-in is used to slow the signal down to a recordable level. A replica of the input signal to the sampling unit is output as a lower frequency analog signal which is digitized.

The analog output signal from the sampling unit is input into an 8 bit analog-to-digital (A/D) converter which has a memory of 1024 8-bit words. Since the desired signal requires more than 1024 samples to record the entire signal, the A/D conveter has a built-in option which allows the recording of successive records of 1024 samples by counting $(N-1)^2 1024$ samples before beginning to digitize the signal (N = the number of the data group which is desired). After each data group is written into the memory of the A/D converter, it is read out onto an 8-bit paper tape which is then read into a PDP 11/50 computer for the appropriate pre-processing prior to analysis on an IBM 360-91/75 computer. The pre-processing performed on the PDP 11/50 consists of merging and editing the appropriate data groups together to form one data record for each receiver position recorded. If the data were clipped, this record would be read to paper tape and the amplification factors would be adjusted to record an unclipped record. Once recorded both clipped and unclipped records are read into the computer and corrected using a scaling program to obtain the final unclipped record of the data trace for that receiver position.

Model

The model used is a 2.0 inch, 4.5 feet long, stainless steel cylinder which has a longitudinal wave velocity of 18996 ft/sec and a transverse wave velocity of 10170 ft/sec. Three dimensional scattered and diffracted fields of a simulated acoustic point source due to a cylinder are studied: (1) the 2D coplanar case; (2) the 3D non-coplanar case. Receivers are placed in the same horizontal plane as the source for Case (1) and for Case (2) they are placed in a horizontal plane different from the source. The non-coplanar case is particularly designed to study the helical waves. The coplanar case simulates the scattering and diffraction from an infinite elastic cylinder immersed in a fluid due to an acoustic line source parallel to the cylinder axis.

The geometrical configuration of the source and the receivers for both the coplanar and the non-coplanar cases are shown in Figures 5 and 6. The same azimuthal receiver locations are used throughout the experiment. Only the horizontal plane of the receivers is altered. In order to obtain data in the illuminated zone the source and the receiver locations were changed to $6R_0$ as shown in Figure 6.

The configurations of the source and the receivers in this study are divided into four regions. Region I consists of receivers at azimuths 0° to 30° on a circular arc of $3.5R_0$ about the cylinder for a source located $3.5R_0$ from the cylinder axis. These receivers are

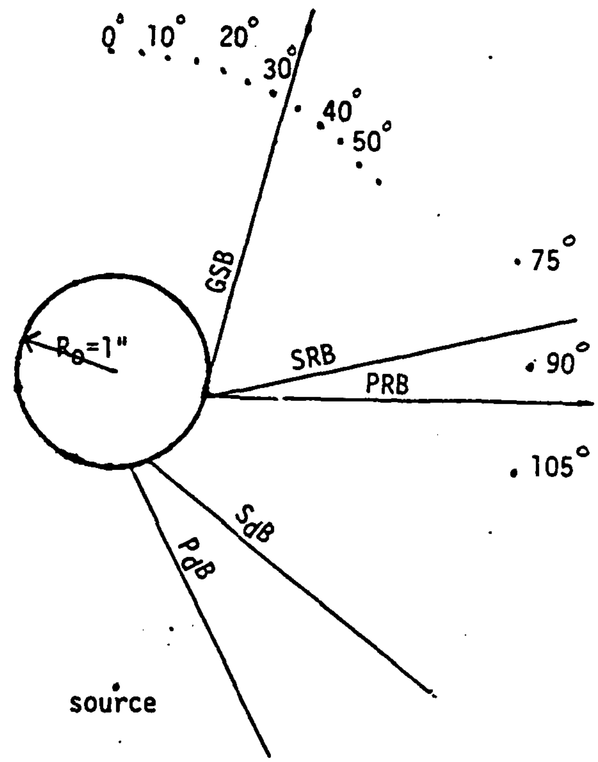

Figure 5: Source and receiver configuration for regions I, II, III.
GSB = Geometrical Shadow Boundary
SRB = S Reflection Boundary
PRB = P Reflection Boundary
S_dB = Diffracted S Wave Boundary
P_dB = Diffracted P Wave Boundary

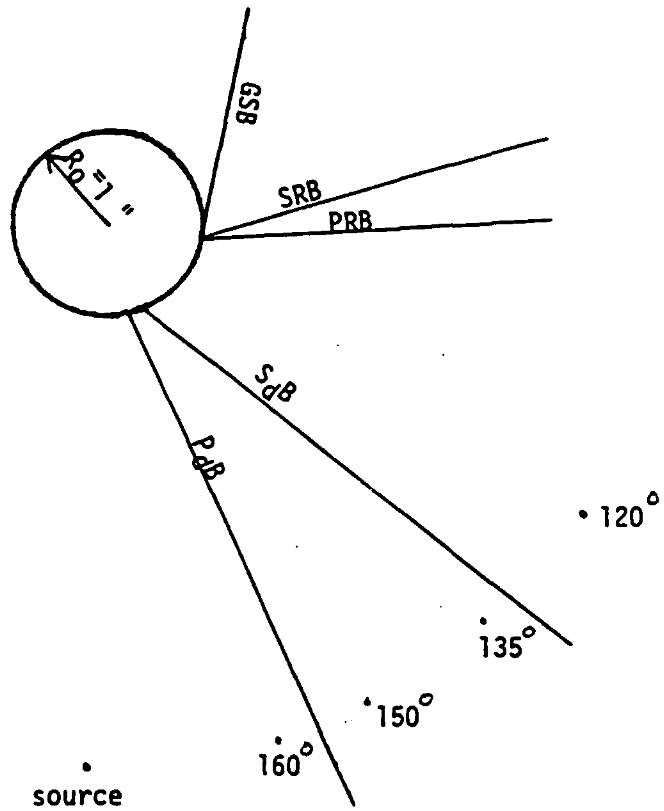

Figure 6: Source and receiver configuration for region IV.
GSB = Geometrical Shadow Boundary
SRB = S Reflection Boundary
PRB = P Reflection Boundary
S_dB = Diffracted S Wave Boundary
P_dB = Diffracted P Wave Boundary

all located in the geometrical shadow zone beyond the geometrical shadow boundary(GSB). Regions II, III and IV are all within the illuminated zone. Region II has the source located at $3.5R_0$ with the receivers also at $3.5R_0$ at azimuths 35° to 55°. This region is beyond the S Reflection Boundary(SRB) where reflected waves are not dectected but diffracted waves are detected. Region III has the source located at $3.5R_0$ while the receivers are on a $4.5R_0$ circular arc at azimuths 75° to 105°. This region is within the S and P Reflection Boundaries(SRB and PRB) where critically reflected and diffracted waves propagate. For Region IV, as shown in Figure 6, the source is located at $6R_0$ and the receivers are placed at azimuths 120° to 160° $6R_0$ from the cylinder. This region is within the boundaries for P and S wave diffractions where only reflected and transmitted waves propagate. Figures 7 display the interpreted data for the Region I, the shadow zone(SZ). Figures 8,9 and 10 display the interpreted data for Regions II, III and IV located in the various parts of the illuminated zone(IZ).

ANALYSIS, INTERPRETATION AND DISCUSSION

Geometry of Raypaths(Wavefront Parametric Equations)

Definition and notation of various types of waves

The following symbols are used to define the various types of waves in this thesis. K is used to denote the acoustic waves propagating in the acoustic medium outside the elastic cylinder. P and S are used to denote the longitudinal and transverse waves propagating

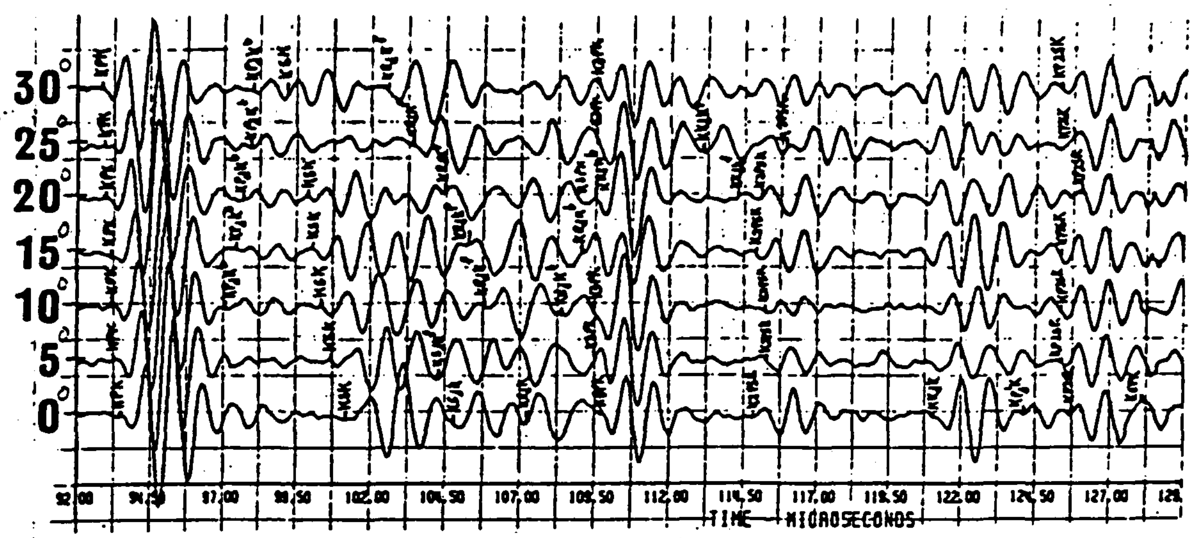

a.) 3D

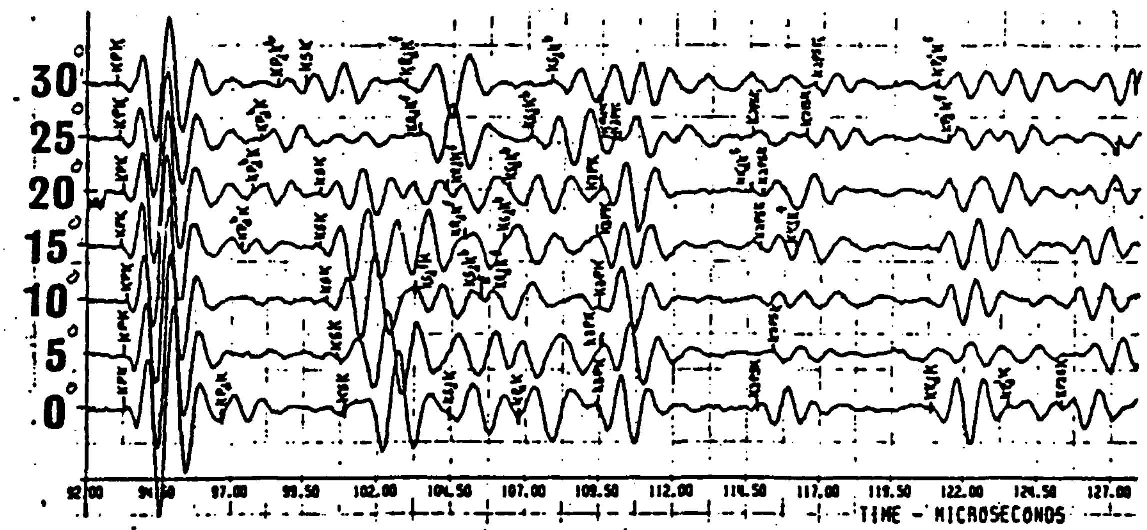

b.) 2D

Figure 7: Region I data

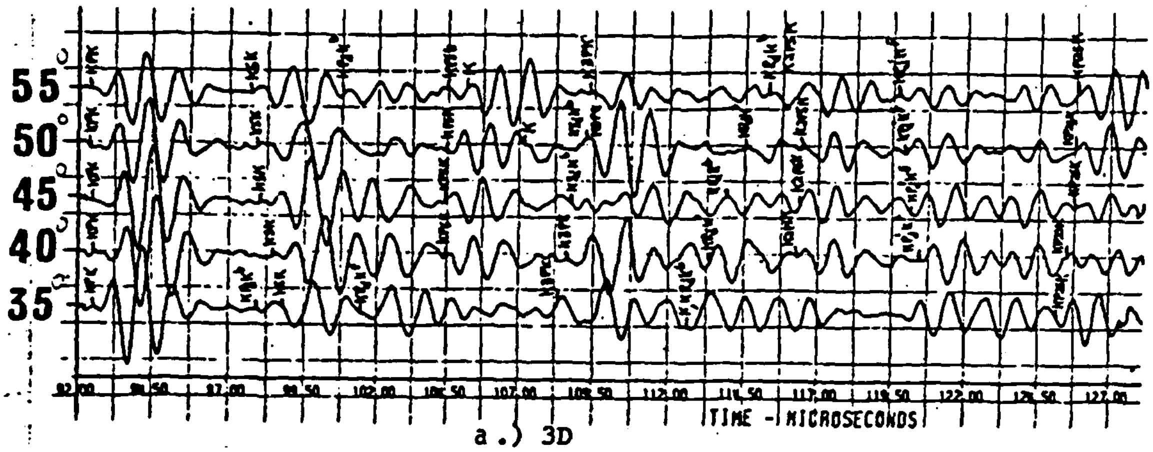

a.) 3D

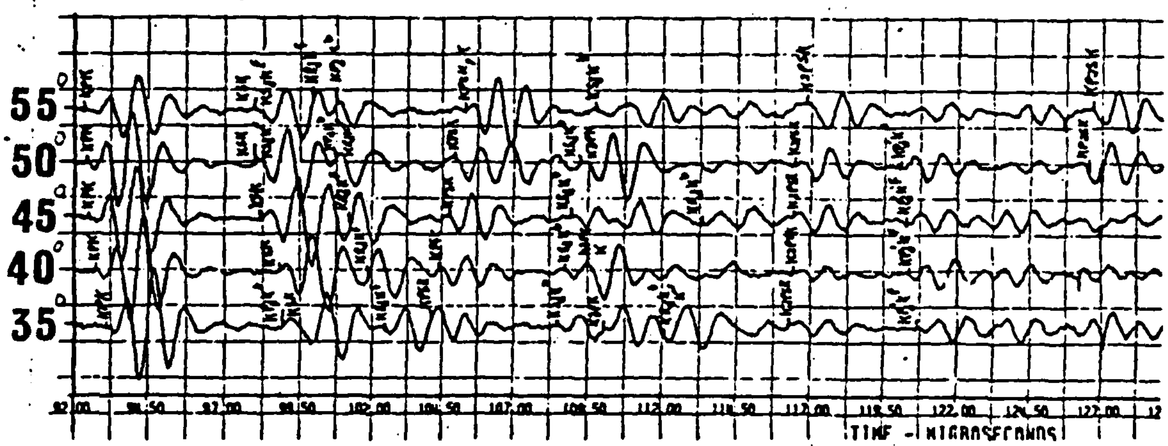

b.) 2D

Figure 8: Region II data

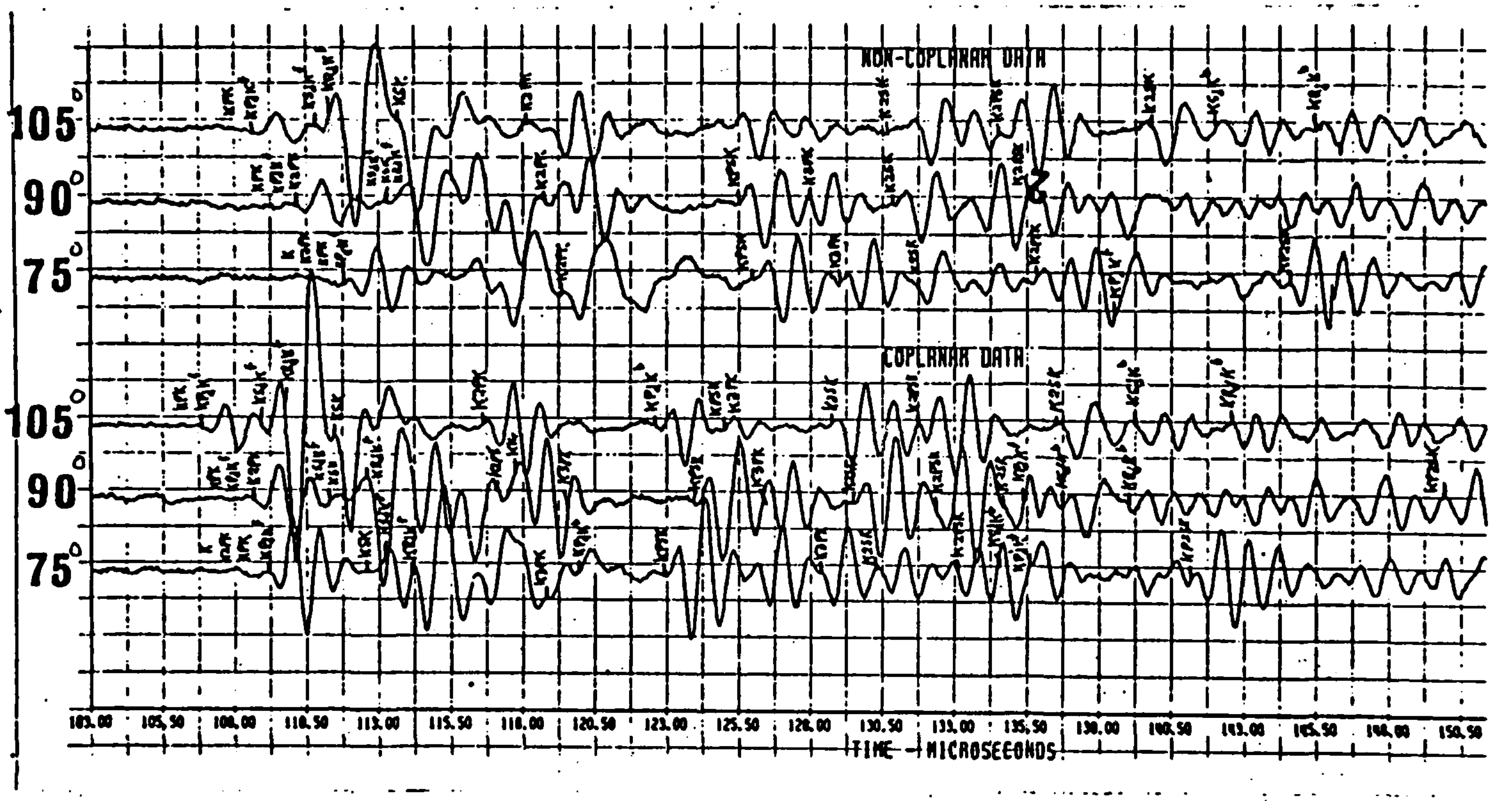

Figure 9: Region III data
Bottom 3 traces are 2D data
Top 3 traces are 3D data

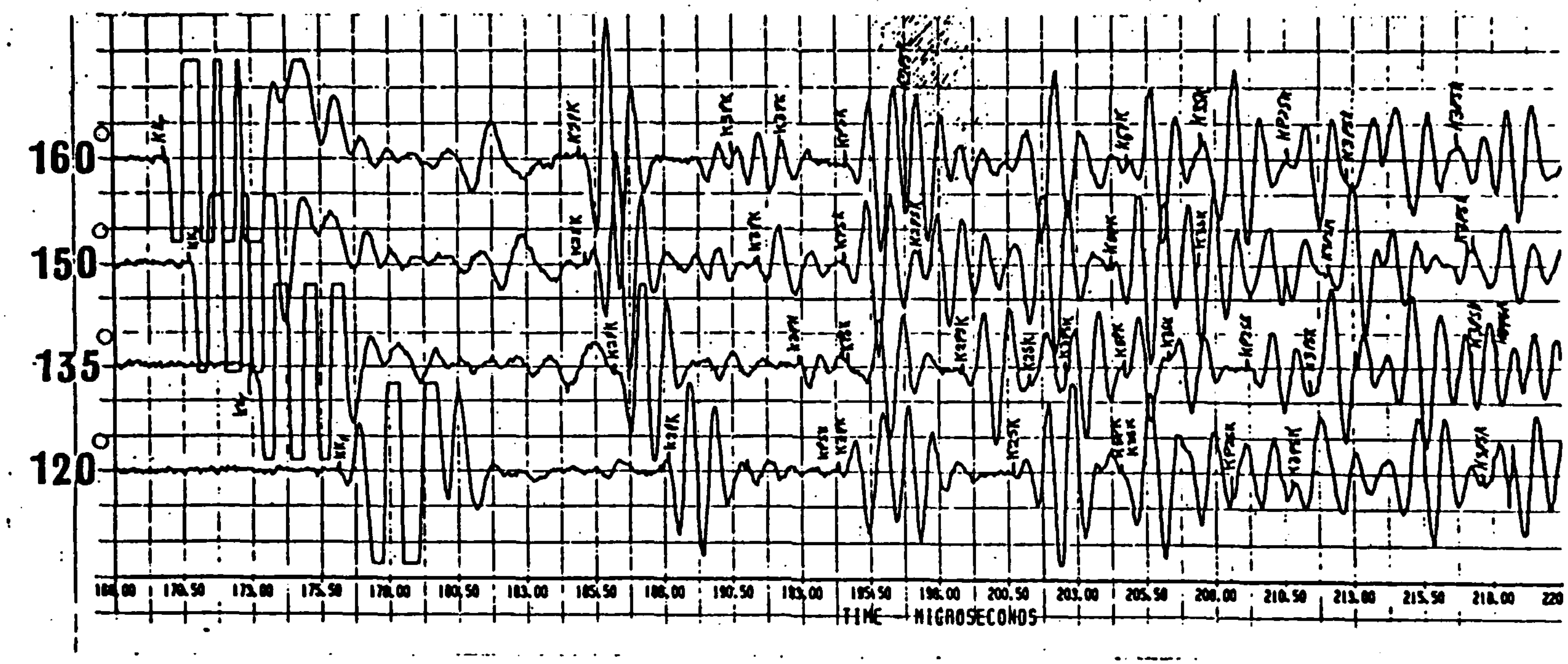

Figure 10a: Region IV 2D data

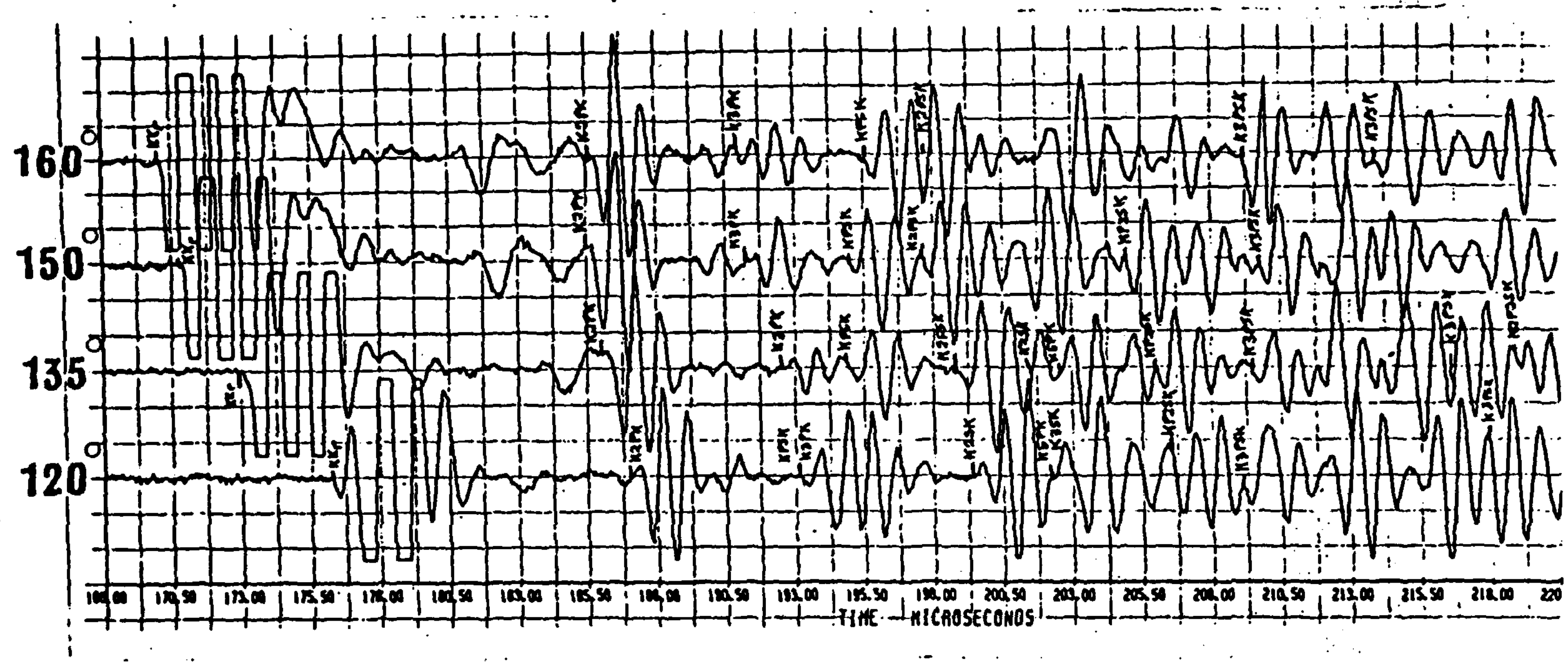

Figure 10b: Region IV 3D data

inside the elastic cylinder. P_d and S_d denote the diffracted longitudinal and transverse waves which propagate at the cylinder interface. K_d and R_d denote the diffracted acoustic wave and the diffracted Rayleigh wave ,respectively.

Combinations of the symbols K, P, S, P_d, S_d, R_d and K_d are used to describe the ray paths of the waves interpreted in this study. The direct acoustic wave which has no interaction with the cylinder model is denoted by K. KK_r denotes an incident acoustic wave, K, reflected from the cylinder. KPK denotes an incident acoustic wave, K, refracted into the elastic cylinder as a longitudinal wave, P, and refracted into the acoustic medium as an acoustic wave, K. Analogous to KPK is KSK , the difference being the wave travels as a transverse wave, S, inside the elastic cylinder. Waves which are multiply reflected a P waves inside the elastic cylinder are denoted by KnPK, where n equal the number of P wave ray paths. Similarly, KmSK denote multiply internally reflected S waves with m being the number of S wave ray paths. points inside the elastic cylinder. Diffracted waves are denoted as follows: KP_dK is the diffracted P wave; KS_dK is the diffracted S wave; KR_dK is the diffracted Rayleigh wave; KK_dK is the diffracted acoustic wave. Full circumnavigations of the cylinder by the various diffracted waves are denoted by $KP_d{}^1K$ and similarly for the other diffracteins. For non-symmetric source-receiver configurations , as shown in Figures 5 and 6 the diffractions propagate in both directions.

The front diffraction(the shortest path) is denoted by KP_dK^f and the back diffraction(the longest path) is denoted by KP_dK^1. the same symbolism is used for all of the front and back diffracted waves.

Direct Waves

The direct waves, K,are only observed in the illuminated zone, i.e., at receivers in Regions II, III and IV. In Region II, K arrives at approximately 112 μsec at 35° coupled with KR_dK^b (see Figure 8). At 40°, K arrives coupled with K3PK and again at 55° coupled with KPSK at approximately 105.5 μsec. At 45°, K is not visible. There is a data void from 107 to 108.25 μsec. Destructive interference as well as low source strength account for the loss of data where K should appear. Unlike Region II, K arrives among the first arrivals in Region III(see Figure 8). It is coupled with KPK, K2PK and KP_dK^f arriving at approximately 109.25 μsec at 75° for the coplanar case. Region IV is devoid of K arrivals due to the source radiation pattern and the geometrical configuration used.

Reflected Waves

Region II receives no reflected events, KK_r, because this region is beyond the critical reflection boundaries for P and S waves. Critically reflected P and S waves are excited beyond the P and S diffracted wave boundaries. The most prominent KK_r arrivals appear at receivers in Region IV. They are the first arrivals and their amplitude is much greater than the diffracted and refracted wave arrivals. In order to show all of the arrivals, the KK_r events are displayed clipped.

The wavefronts for the reflected waves, KK_r, can be described parametrically. According to Huygens' Principle the surface of the cylinder will have and an infinite number of secondary sources when the incident energy from the source irradiates it. Let $Q(\xi,\eta,\zeta)$ be the coordinate point of the secondary source on the surface of the cylinder. Let $P(x,y,z)$ represent a point on the advancing wavefront of the reflected wave from the secondary sources on the cylinder's surface. The length of the incident ray from the source, $S(0,0,0)$, to the cylinder is given parametrically as

$$R_i = (Y_0{}^2 - 2aY_0\cos\theta + a^2\sec^2\phi)^{\frac{1}{2}} \qquad (1)$$

where Y_0 is the y coordinate of the offset cylindrical axis and a is the radius of the cylinder. The parameters used to describe the wavefront are θ and ϕ(see Figure 11). Parametrically, the point $Q(\xi,\eta,\zeta)$on the surface of the cylinder is given as

$$\xi = a\sin\theta \tag{2a}$$

$$\eta = Y_0 - a\cos\theta \tag{2b}$$

$$\zeta = a\tan\phi \ . \tag{2c}$$

From the surface of the cylinder, the general equation for the expanding wavefront in three dimensions from $Q(\xi,\eta,\zeta)$ is

$$(x - \xi)^2 + (y - \eta)^2 + (z - \zeta)^2 = R^2 \tag{3}$$

where R is the radius of the expanding wavefront at any point $P(x,y,z)$. In order to describe the surface of the wavefront due to all of the secondary sources at a given point $P_0(x_0,y_0,z_0)$, equation (3) is differentiated with respect to θ and ϕ and then these equations are solved along with equation (3) for the coordinates x, y, and z. This solution provides the coordinates of the point $P_0(x_0,y_),z_0)$ on the wavefront of the reflected waves,KK_r. Differentiating equation(3) we obtain

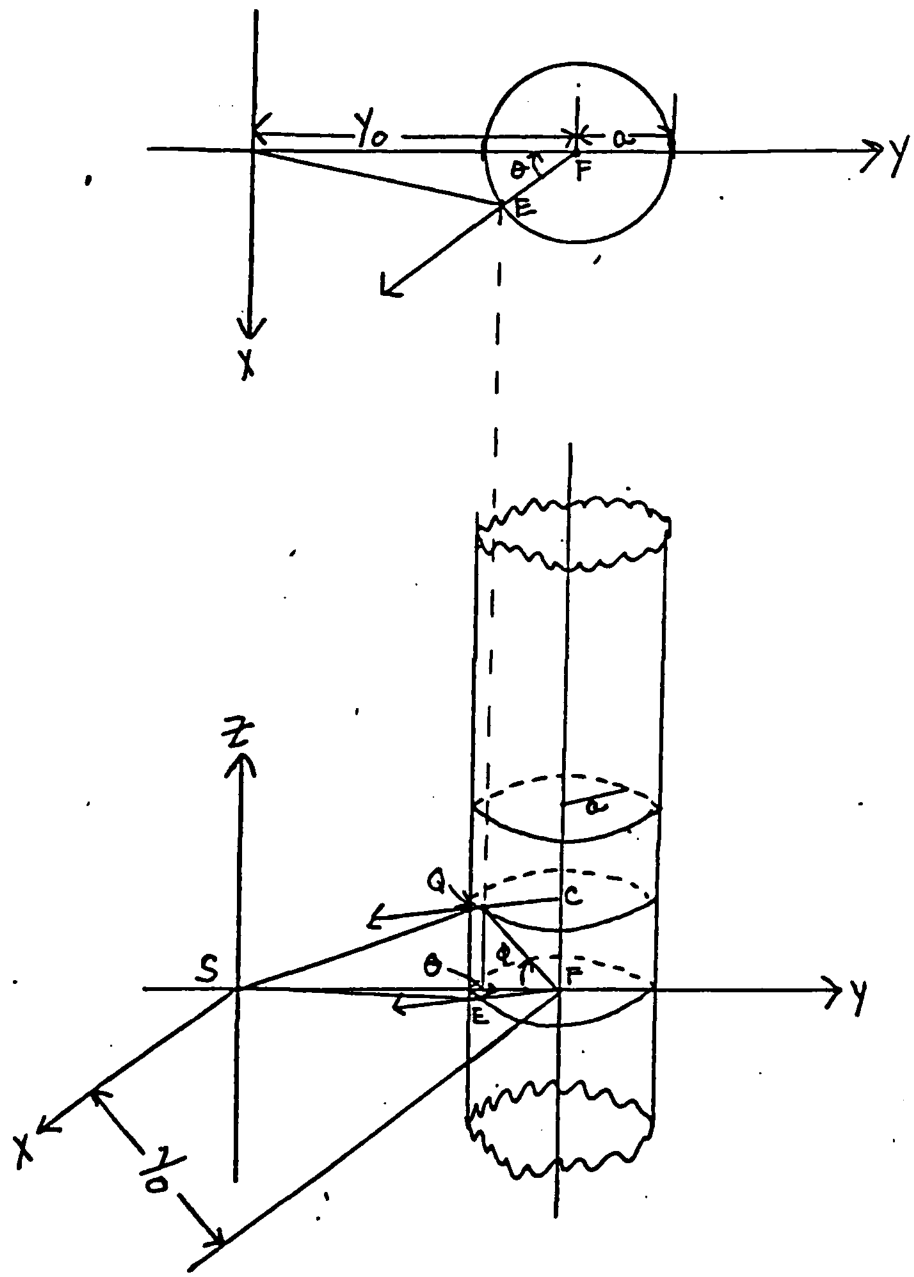

Figure 11: Reflected wave parameter description
S = S(0,0,0)
Q = Q(ξ,η,ζ)
C = C(0,Y_o,ζ)
E = E(ξ,η,0)
F = F(0,Yo,0)

$$a(x_0 - \xi)\cos\theta + a(y_0 - \eta)\sin\theta = -R\partial R/\partial\theta \tag{4a}$$

$$a(z_0 - \zeta)\sec^2\phi = -R\partial R/\partial\phi \quad . \tag{4b}$$

The radius of the expanding wavefront for KK_r is

$$R_1 = c^2t - R_i \tag{5}$$

where t is the time variable, c is the acoustic velocity of the fluid surrounding the cylinder and R_i is the length of the ray, or the wavefront radius, from the source to the cylinder as given in equation (1). By substituting equations (1), (2) and (5) into equations (3) and (4) and solving for x, y and z, we obtain the following solution for a point $P_0(x_0,y_0,z_0)$ on the wavefront of KK_r:

$$x_0 = \xi + R_1(R_i^{-1}Y_0\sin\theta\cos\theta \pm \sin\theta(1 - R_i^{-2}$$
$$Y_0^2\sin^2\theta - a^2R_i^{-2}\tan^2\phi)^{\frac{1}{2}}) \tag{6a}$$

$$y_0 = \eta + R_1(R_i^{-1}Y_0\sin^2\theta \mp \cos\theta(1 - R_i^{-2}$$
$$Y_0^2\sin^2\theta - a^2R_i^{-2}\tan^2\phi)^{\frac{1}{2}}) \tag{6b}$$

$$z_0 = \zeta + aR_1R_i^{-1}\tan\phi \tag{6c}$$

Equations (6) describe the three dimensional wavefront of the waves reflected from the cylinder. If $\theta = 0$ equations (6) reduce to the two dimensional wavefront and ray path equations as follow:

$$x_0 = \xi + R_1(R_i^{-1}Y_0\sin\theta\cos\theta \pm \sin\theta(1 - R_i^{-2}$$

$$Y_0^2\sin^2\theta)^{\frac{1}{2}} \tag{7a}$$

$$y_0 = \eta + R_1(R_i^{-1}Y_0\sin^2\theta \mp \cos\theta(1 - R_i^{-2}Y_0^2\sin^2\theta)^{\frac{1}{2}}) \tag{7b}$$

$$z_0 = 0 \tag{7c}$$

$$R_i = (Y_0^2 + a^2 - 2aY_0\cos\theta)^{\frac{1}{2}} . \tag{7d}$$

Refracted Waves

Refracted waves are not recorded in this study because the receivers are restricted to recording in the fluid exterior to the cylinder. The parametric wavefront equations are given for completeness. The radius of the refracted waves expanding wavefront is given as follows

$$R_2 = \gamma_p(ct - R_i) \qquad \gamma_p = v/c. \tag{8}$$

where v is the velocity of the refracted wave. For the refracted P wave, KP, $v = \alpha$ and for the refracted S wave, KS, $v = \beta$. The length of the incident ray, R_i, is given by equation (1) and the point $Q(\xi,\eta,\zeta)$ on the cylinder's surface is given by equations (2). Substituting equations (1), (2) and (8) into equations (3) and (4) we obtain the parametric equations for the wavefront of the refracted wave (P or S) at P_0 as follows:

$$x_0 = \xi + R_2(R_i^{-1}Y_0\sin\theta\cos\theta \pm \sin\theta(1 - \gamma_p^2 R_i^{-2}Y_0^2\sin^2\theta - \gamma_p^2a^2R_i^{-2}\tan^2\phi)^{\frac{1}{2}}) \tag{9a}$$

$$y_0 = \eta + R_2(R_i^{-1}Y_0\sin^2\theta \mp \cos\theta(1 - \gamma_p^2R_i^{-2}Y_0^2 \sin^2\theta - \gamma_p^2a^2R_i^{-2}\tan^2\phi)^{\frac{1}{2}}) \tag{9b}$$

$$z_0 = \zeta + \gamma_p aR_2R_i^{-1}\tan\phi \, . \tag{9c}$$

For equations (9) to apply, θ and ϕ are subject to the condition that:

$$0 < \theta_{inc} < \sin^{-1}(v/c) \tag{10}$$

where v is equal to α for KP and β for KS.

Transmitted Waves

The transmitted waves are due to the numerous combinations of waves refracted inside the cylinder before they are transmitted(refracted) into the fluid medium outside the cylinder in which the recording is being done. The secondary source points $Q(\xi,\eta,\zeta)$ on the surface of the cylinder are redefined as follows (see Figure 12):

$$\xi = a\sin(\theta + \theta_i) \tag{11a}$$

$$\eta = Y_0 - a\cos(\theta + \theta_i) \tag{11b}$$

$$\zeta = a\tan\phi + b_i \tag{11c}$$

$$b_i = 2a^2\sin(\theta_i/2)\tan\phi/Y_0\sin\theta \tag{11d}$$

$$\theta_i = \pi - 2(\sin^{-1}(\gamma_i Y_0 \sin\theta/(Y_0{}^2 + a^2 - 2aY_0\cos\theta)^{\frac{1}{2}}) \tag{11e}$$

where i = 1 for P waves and 2 for S waves and

$$\gamma_1 = \alpha/c; \ \gamma_2 = \beta/c; \ \theta_{ti} = \sin_{-1}(\gamma_i \sin\theta_{inc}) \tag{11f}$$

For a given ray path defined by an initial θ and ϕ, the three dimensional ray paths interior to the elastic cylinder trace out a helix on the surface of the cylinder. Figure 12 defines the parameters to be used to obtain equation (11d). Figures 13, 14 and 15 show thw plan views of the three triangles used to obtain the following relationships leading to equation (11d).

$$\overline{SQ} = R_i = (Y_0{}^2 - 2aY_0\cos\theta + a^2\sec^2\phi)^{\frac{1}{2}} \tag{12}$$

$$\overline{SC} = D_i = (Y_0{}^2 + a^2\tan^2\phi)^{\frac{1}{2}} \tag{13}$$

$$\overline{QC} = a = \text{cylinder radius} \tag{14}$$

$$\psi_1 = \measuredangle\, SCQ \ . \tag{15}$$

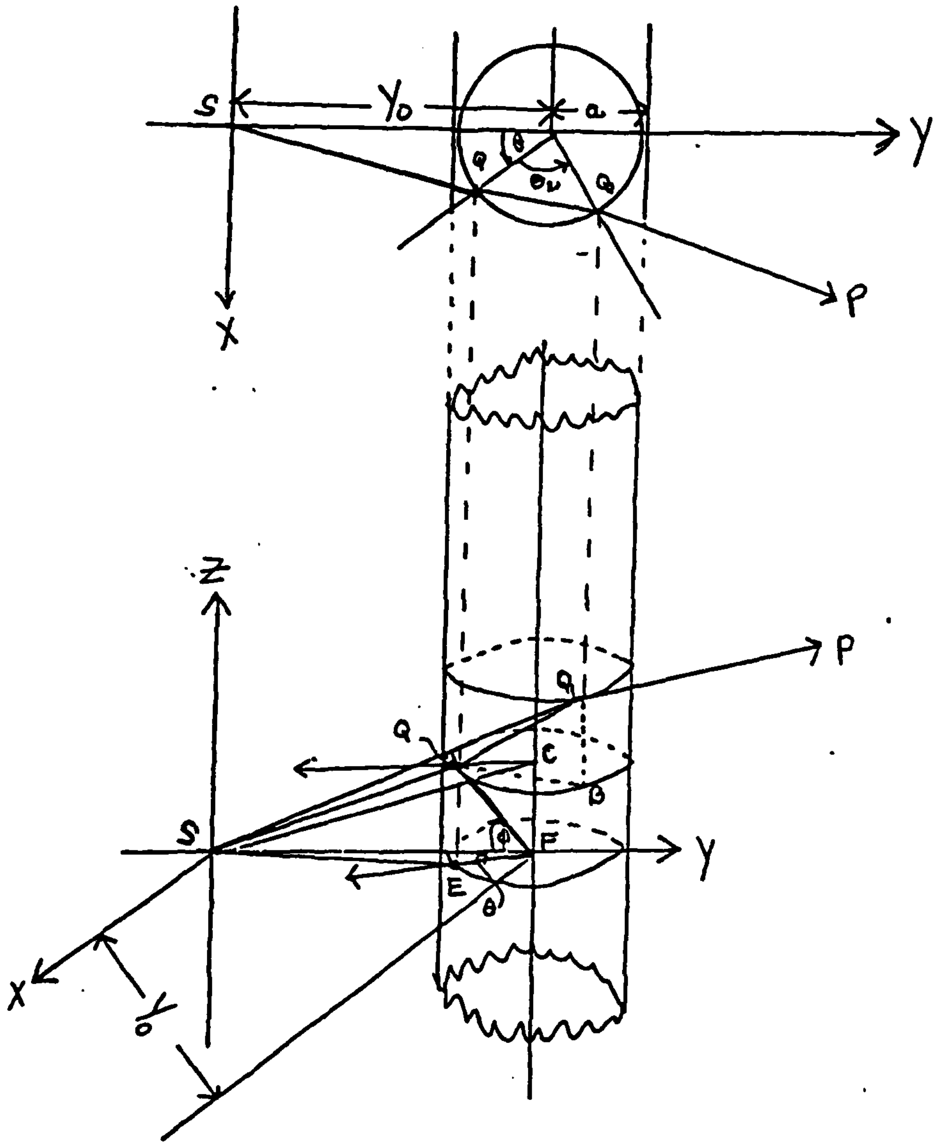

Figure 12: Transmitted wave parameter description

$S = S(0,0,0)$ | $E = E(\xi,\eta,0)$
$Q = Q(\xi,\eta,\zeta)$ | $F = F(0,Y_0,0)$
$Q_1 = Q_1(\xi_1,\eta_1,\zeta_1)$ | $\measuredangle SEF = \theta$
$C = C(0,Y_0,\ )$ | $\measuredangle BQQ_1 = \Psi_2$
$B = B(\xi_1,\eta_1,\zeta)$ | $\measuredangle SCQ_1 = \Psi_1$

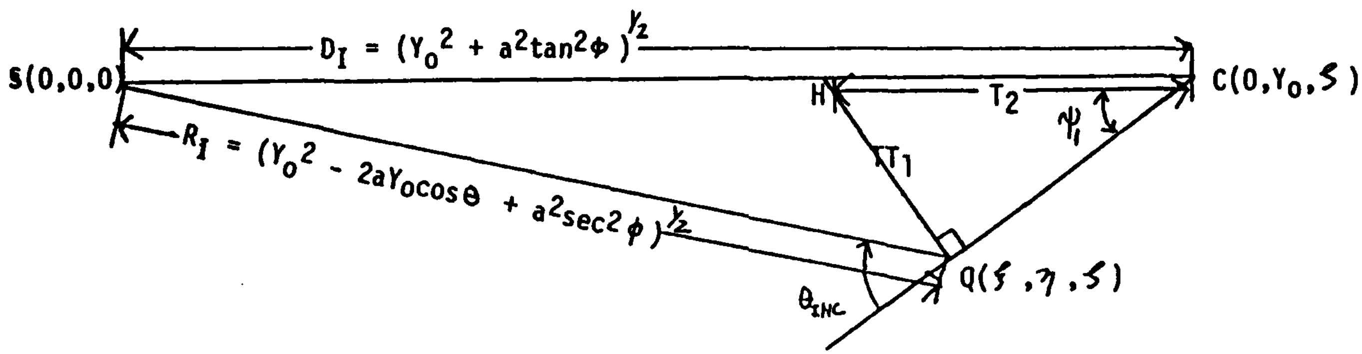

Figure 13: Triangle SQC 2D representation

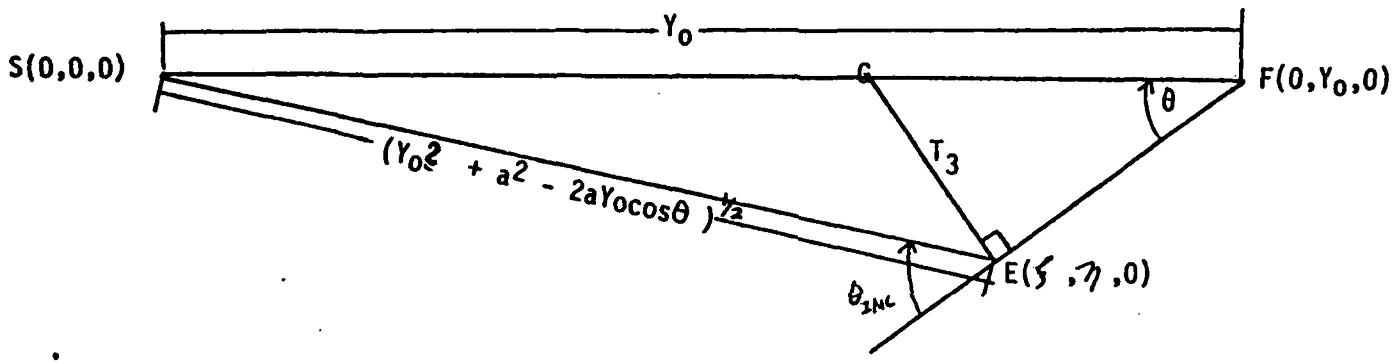

Figure 14: Triangle SEF 2D representation

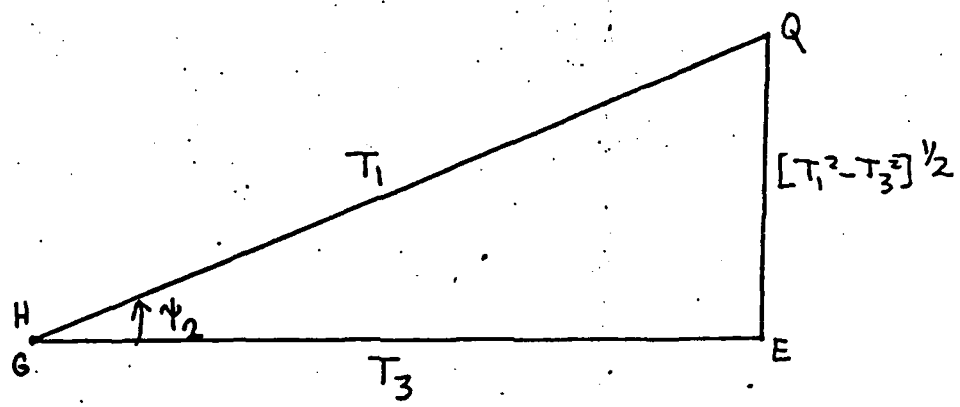

Figure 15 Right triangle giving helix slope

Using equations (13), (14) and (15) we can rewrite equation (12) and solve for $\cos\psi_1$:

$$R^2_i = D^2_i + a^2 - 2aD_i\cos\psi_1 \tag{16}$$

$$\cos\psi_1 = -Y_0\cos\theta(Y^2_0 + a^2\tan^2\phi)^{-\frac{1}{2}} \tag{17}$$

$$T_2 = \overline{HC} \quad ; \quad \cos\psi_1 = a/T_2 \tag{18}$$

$$T_2 = a(Y^2_0 + a^2\tan^2\phi)^{\frac{1}{2}}/Y_0\sin\theta \tag{19}$$

$$T_1 = \overline{HQ} = (T^2_2 - a^2)^{\frac{1}{2}} \tag{20}$$

$$T_1 = a(Y^2_0\sin^2\theta + a^2\tan^2\phi)^{\frac{1}{2}}/Y_0\cos\theta \tag{21}$$

$$T_3 = a\tan\theta \tag{22}$$

$$\tan\psi_2 = (T^2_1 - T^2_3)^{\frac{1}{2}}/T_3 \tag{23}$$

$$\tan\psi_2 = a\tan\phi/Y_0\sin\theta \ . \tag{24}$$

$$b_i = \overline{QB}\tan\psi_2 \tag{25}$$

$$\overline{QB} = 2a\sin(\theta_i/2) \ . \tag{26}$$

Using equations (24), (25) and (26) we obtain equation (11d) for the pitch of the helix: For the first transmitted P wave, KPK, the expanding secondary source radius is:

$$R_4 = ct - R_i - 2(c/\alpha)a^2\sin(\theta_1)(1+ a^2\tan^2\phi/Y_0{}^2\sin^2\theta)^{\frac{1}{2}} \tag{27}$$

Similarly, the expanding radius for the first transmitted S wave, KSK, is:

$$R_5 = ct - R_i - 2(c/\beta)a^2\sin(\theta_2)(1+ a^2\tan^2\phi/Y_0{}^2\sin^2\theta)^{\frac{1}{2}} \tag{28}$$

Substituting equations (27) and (28) into equations (3) and (4), we obtain the parametric wavefront and ray path equations for KPK and KSK as follow:

$$x_0 = \xi - ((Z_1 + Z_2)/(1 + Y_i))\cos(\theta + \theta_i) \pm \sin(\theta + \theta_i)$$

$$(R_j^2 - ((Z_1 + Z_2)/(1 + Y_i))^2 - (z_0 - \zeta)^2)^{\frac{1}{2}} \qquad (29a)$$

$$y_0 = \eta - ((Z_1 + Z_2)/(1 + Y_i))\sin(\theta + \theta_i) \mp \cos(\theta + \theta_i)$$

$$(R_j^2 - ((Z_1 + Z_2)/(1 + Y_i))^2 - (z_0 - \zeta)^2)^{\frac{1}{2}} \qquad (29b)$$

$$z_0 = \zeta - R_j a\tan\phi(R_i^{-1}(2ac/c_i)\sin(\theta_i/2)(1 + a^2\tan^2\phi//Y_0^2$$

$$\sin^2\theta)^{-\frac{1}{2}})/(Y_0\sin\theta + 2a\sin(\theta_i/2)) \qquad (29c)$$

$$Z_1 = R_j((-ac/c_j)(1 + a^2\tan^2\phi/Y_0^2)^{\frac{1}{2}}Y_i\cos(\theta_i/2) + (2a^3c/c_j$$

$$Y_0^2)\sin(\theta_i/2)\tan^2\phi(1 + a^2\tan^2\phi/Y_0^2\sin^2\theta)^{-\frac{1}{2}}\csc^2\theta\cot\theta$$

$$+ \ Y_0R_i^{-1}\sin\theta) \qquad (29d)$$

$$Z_2 = (z_0 - \zeta)(aY_i\tan\phi\cos(\theta_i/2)/Y_0\sin\theta - (a/Y_0)\tan\phi$$

$$\csc\theta\cot\theta\sin(\theta_i/2)) \qquad (29e)$$

$$Y_i = (\gamma_i a Y_0{}^2 \sin^2\theta - \gamma_i Y_0 \cos\theta (Y_0{}^2 + a^2 - 2aY_0\cos\theta))$$

$$/((Y_0{}^2 + a^2 - 2aY_0\cos\theta)(Y_0{}^2 + a^2 - 2aY_0\cos\theta - \gamma_i{}^2 Y_0{}^2$$

$$\sin\theta)^{\frac{1}{2}}) . \tag{29f}$$

For the KPK wavefronts and ray paths use equations (28) and(29) with $i = 1$ and $j = 4$. Similarly for KSK use $i = 2$ and $j = 5$ in equations (28) and (29).

Multiply internally reflected and converted transmitted waves

To obtain these wavefront and ray path parametric equations, we again must redefine the secondary source points $Q(\xi,\eta,\zeta)$ which are on the surface of the cylinder as:

$$\xi = a\sin(\theta + l\theta_1 + m\theta_2) \tag{30a}$$

$$\eta = Y_0 - a\cos(\theta + l\theta_1 + m\theta_2) \tag{30b}$$

$$\zeta = a\tan\phi + l\theta_1 + m\theta_2 \tag{30c}$$

l and m take on integer values which state the number of complete internal P and S wave ray paths that have been completed. The expanding radius of the secondary wavelet for these type of transmitted waves is given by:

$$R_{l,m} = ct - R_i - 2a(1 + a^2\tan^2\phi/Y_0{}^2\sin^2\theta)^{\frac{1}{2}}((lc/\alpha)\sin(\theta_1/2)$$

$$+ (mc/\beta)\sin(\theta_2/2)) \; . \tag{31}$$

Substitution of equations (30) and (31) into equations (3) and (4) yields the parametric wavefront and ray path equations for the KlPmSK transmitted waves:

$$x_0 = \xi - ((Q_1 + Q_2)/(1 + lY_1 + mY_2))\cos(\theta + l\theta_1 + m\theta_2)$$

$$\pm \sin(\theta + l\theta_1 + m\theta_2)(R_{l,m}{}^2 - (z - \zeta)^2 - ((Q_1 + Q_2)/(1 + lY_1$$

$$+ mY_2)))^{\frac{1}{2}} \tag{32a}$$

$$y_0 = \eta - ((Q_1 + Q_2)/(1 + lY_1 + mY_2))\sin(\theta + l\theta_1 + m\theta_2)$$

$$\mp \cos(\theta + l\theta_1 + m\theta_2)(R_{l,m}{}^2 - (z_0 - \zeta)^2 - ((Q_1 + Q_2)/(1 +$$

$$lY_1 + mY_2)))^{\frac{1}{2}} \tag{32b}$$

$$z_0 = \zeta + R_{1,m}(aR_i^{-1}Y_0\tan\phi\sin\theta - 2a^2\tan\phi((1c/\alpha)\sin(\theta_1/$$

$$2))(1 + a^2\tan^2\phi/Y_0^2\sin^2\theta)^{\frac{1}{2}})/Y_0\sin\theta(Y_0\sin\theta + 2a(\sin(\theta_1/2) +$$

$$\sin(\theta_2/2))) \quad (32c)$$

$$Q_1 = (z_0 - \zeta)((a^2\tan^2\phi/Y_0\sin\theta)(Y_1\cos(\theta_1/2) + Y_2\cos(\theta_2/2))$$

$$- (2a^2\tan\phi/Y_0)(\sin(\theta_1/2) + \sin(\theta_2/2))) \quad (32d)$$

$$Q_2 = R_{1,m}(Y_0R_i^{-1}\sin\theta + ((1c/\alpha)\sin(\theta_1/2) + (mc/\beta)\sin(\theta_2/2))$$

$$(1+ a^2\tan^2\phi/Y_0^2\sin^2\theta)^{-\frac{1}{2}}(2a^3/Y_0^2)\tan^2\phi\csc^2\theta\cot\theta +$$

$$(1 + a^2\tan^2\phi/Y_0^2\sin^2\theta)((1c/\alpha)Y_1\cos(\theta_1/2) + (mc/\beta)Y_2$$

$$\cos\theta_2/2))) \quad . \quad (32e)$$

Y_1 and Y_2 are given by equation (29e). Equations (32) will provide the wavefronts and ray paths for all of the transmitted waves. If $1 = 1$ and $m = 0$ or $1 = 0$ and $m = 1$ are applied to equations (32) we obtain equations (17) for KPK and KSK, respectively. If we let $\phi = 0$ in equations (29) we obtain the two dimensional equations as follows:

$$x = \xi - ((Z_1 + Z_2)/(1 + Y_i))\cos(\theta + \theta_i) \pm \sin(\theta + \theta_i)$$

$$(r_j{}^2 - ((Z_1 + Z_2)/(1 + Y_i))^2 - (z - \zeta)^2)^{\frac{1}{2}} \tag{33a}$$

$$y = \eta - ((Z_1 + Z_2)/(1 + Y_i))\sin(\theta + \theta_i) \mp \cos(\theta + \theta_i)$$

$$(r_j{}^2 - ((Z_1 + Z_2)/(1 + Y_i))^2 - (z - \zeta)^2)^{\frac{1}{2}} \tag{33b}$$

$$z = 0 \tag{33c}$$

$$Z_1 = r_j(Y_0 r_i{}^{-1}\sin\theta - (ac/c_i)Y_i\cos(\theta_i/2)) \tag{33d}$$

$$Z_2 = 0 \tag{33e}$$

$$Y_i = \text{see equation (29f)} \tag{33f}$$

$$r_j = ct - r_i - (c/c_i)2a\sin(\theta_i/2) \tag{33g}$$

$$r_i = (Y_0{}^2 + a^2 - 2aY_0\cos\theta)^{\frac{1}{2}} . \tag{33h}$$

The following Figures 16 and 17 display the wavefronts, ray paths and caustics generated by the various transmitted waves according to the two dimensional equations obtained from equations (32) by allowing ϕ to become 0. These waves are identified in the data in Figures 7 through 10. All transmitted converted waves, which have the same number of P and S ray segments interior to the cylinder, arrive simultaneously at the receivers ,.e.g., KPSK and KSPK and K2PSK, KPSPK and KS2PK arrive superimposed as single wavelets. Figure 18 shows the ray combination for the simultaneous arrival of KPSK and KSPK. The interpreted data are labeled K1PmSK since these waves arrive simultaneously. The form of the transmitted mode converted waves, K1PmSK, varies greatly between receivers as shown in Figures 7 through 10. However, the K1PK and KmSK homogeneous transmitted waves retain their waveform between receivers. The variance of the waveform character for the K1PmSK events and the retainment of the waveform character for the K1PK and KmSK events is noticeable by an inspection of the data received in Regions I and II as displayed in Figures 7 and 8. Transmitted waves are received in all four regions. Their interference with the diffracted waves is most noticeable in Regions I and II. It is within these two regions that the diffractions retain enough energy so that they are not masked by the transmitted waves as they are in Regions III and IV.

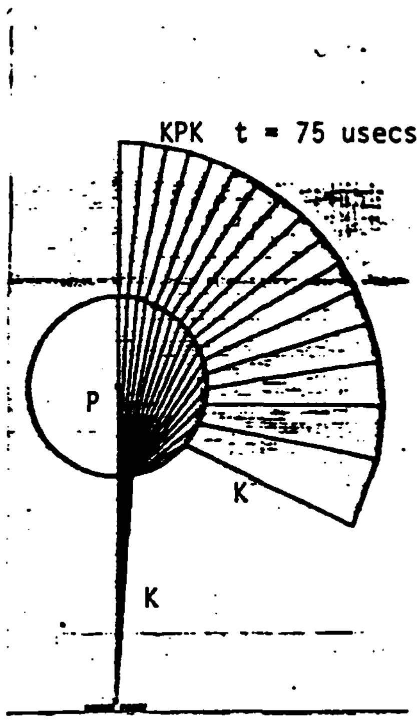

a.) KPK, t = 75 usecs.

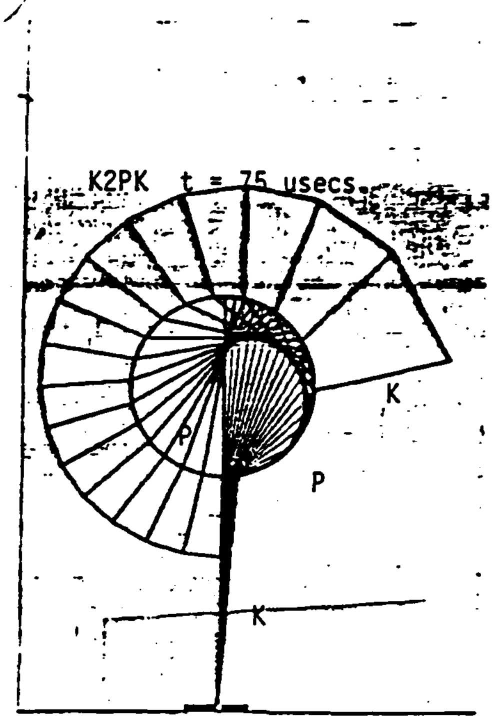

b.) K2PK, t = 75 usecs.

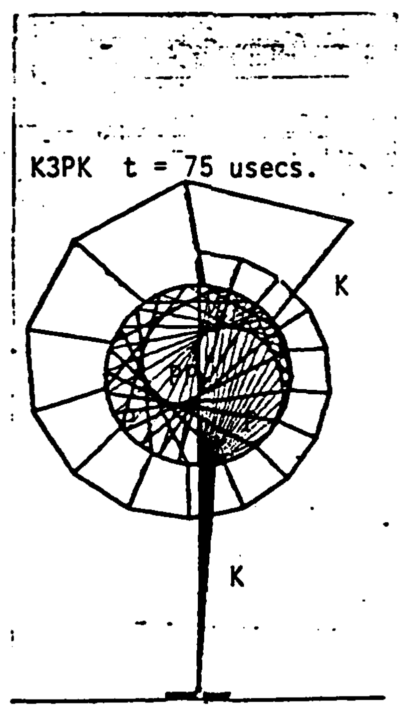

c.) K3PK, t = 75 usecs.

Figure 16a.) Transmitted wavefronts
KPK, K2PK, K3PK at t = 75 usecs.

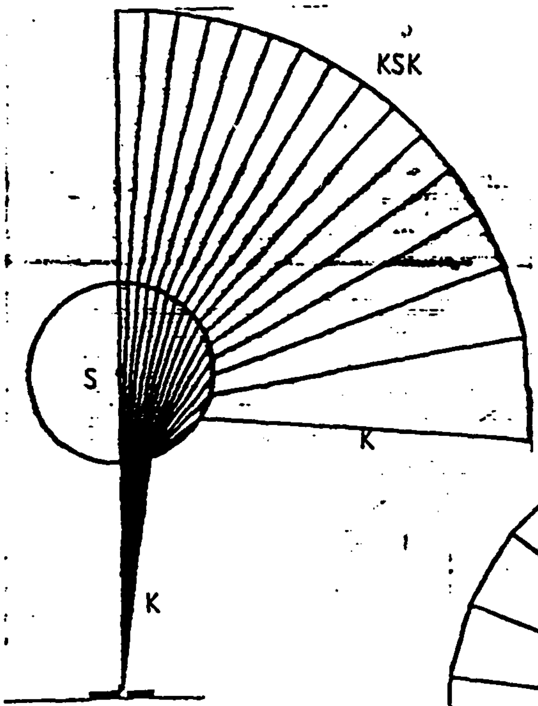

a.) KSK, t= 120 usecs.

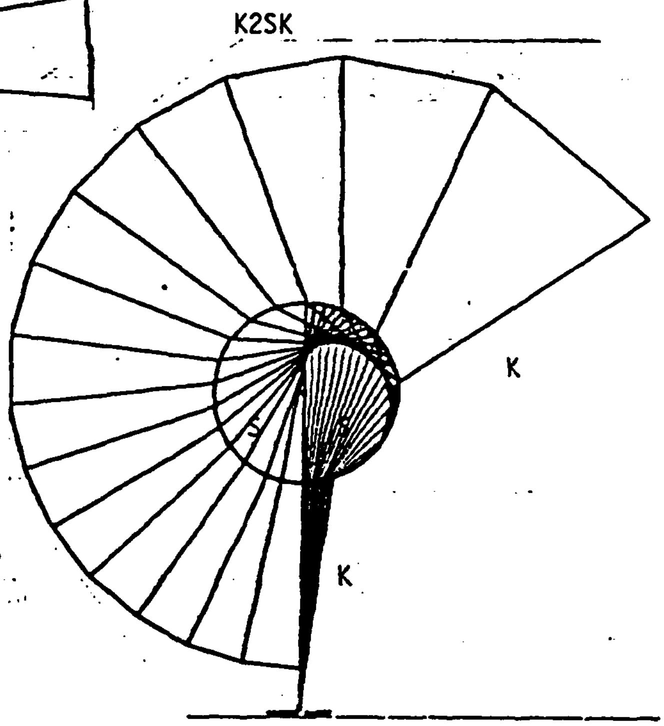

b.) K2SK, t = 120 usecs.

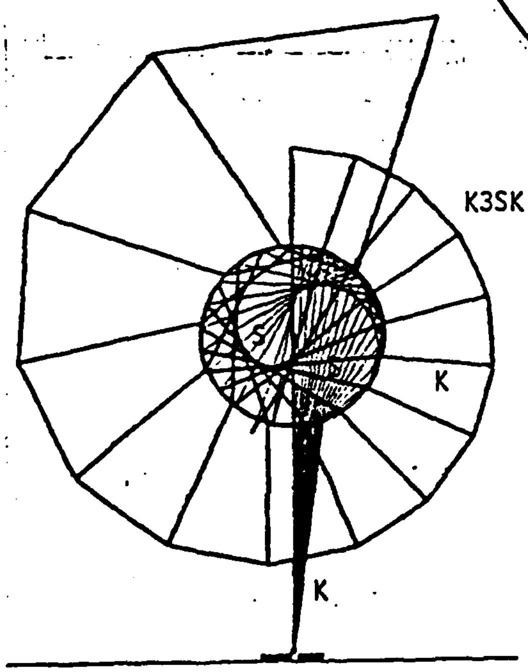

Figure 16b. Transmitted wavefronts KSK, K2SK,K3SK at t = 120 usecs.

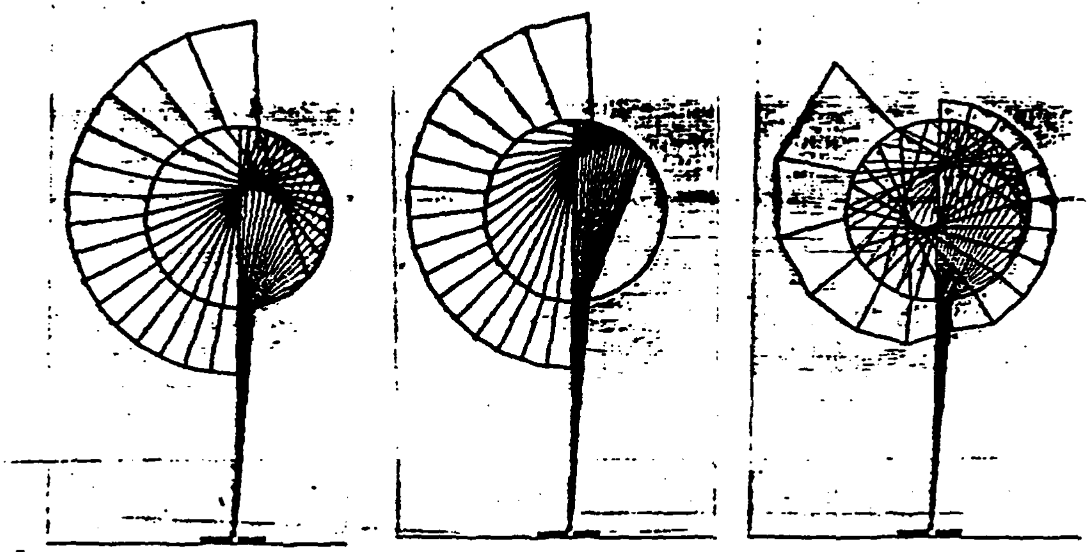

a.) KPSK
t = 80 usecs.

b.) KSPK
t = 80 usecs.

c.) K2PSK
t = 80 usecs.

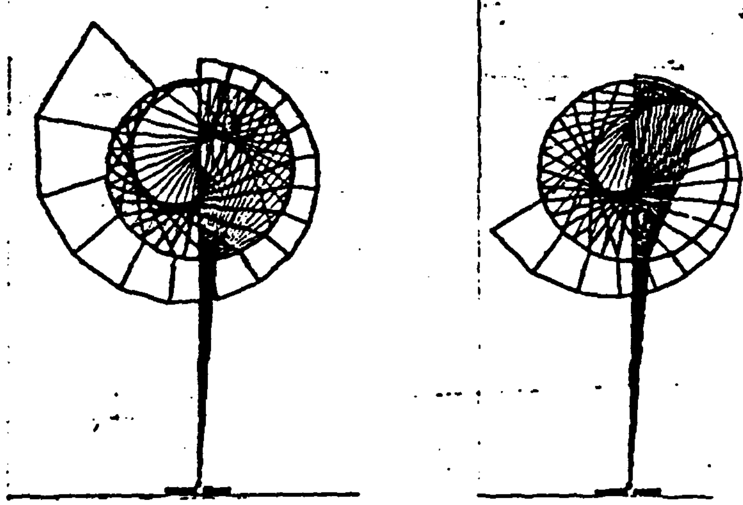

d.) KPSPK
t = 80 usecs.

e.) KSPSK
t = 80 usecs.

Figure 17: Transmitted wavefronts

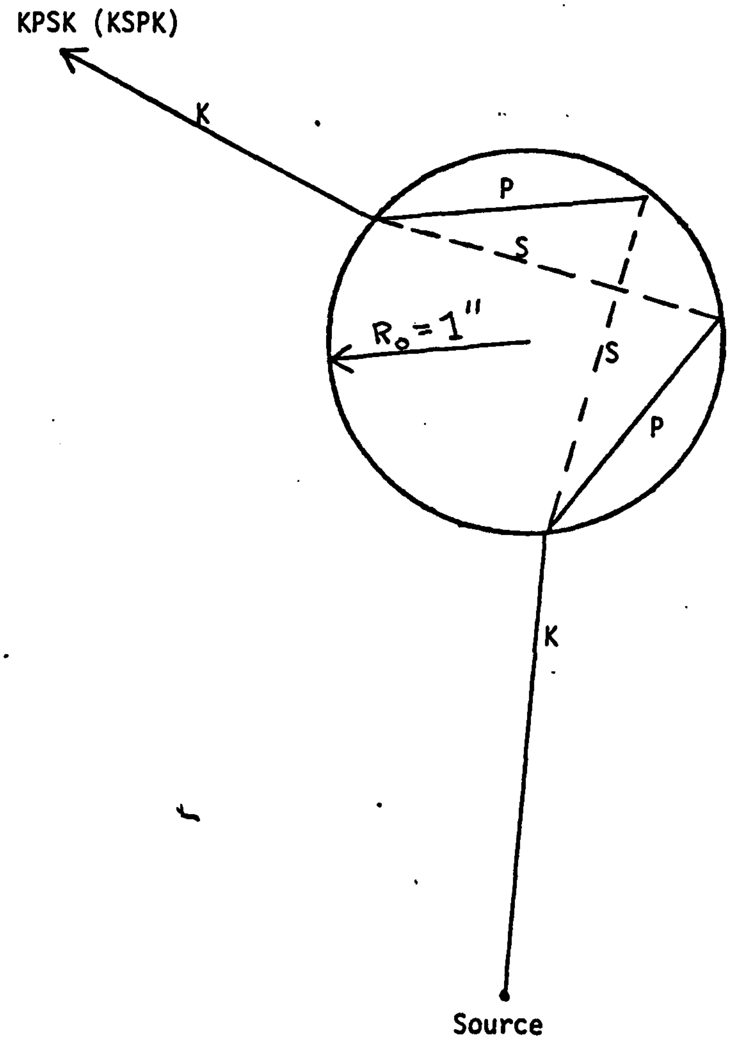

Figure 18: Ray paths showing the simultaneous arrival of KPSK and KSPK

Diffracted Waves

The path of a diffracted wave on the cylindrical acoustic-ealstic interface is a helix, as shown in Figure 19, beginning at the point of excitation. The slope of the helix is defined by the tangent to the cylinder at this excitation point. The slope is given parametrically as:

$$b_{dk} = a^2 \tan\phi / Y_0 \sin\theta_{ck} \tag{34}$$

where $\theta_{ck} = \sin^{-1}(c/c_k)$, $k = 1,2,3$. For $k = 1$ use α, for $k = 2$ use β and for $k = 3$ use v_r. For the KK_dK wave the helix slope is:

$$b_{dk} = a^2 \tan\phi / R_{ic}. \tag{35}$$

The length of the incident acoustic ray path for all of the diffracted waves is:

$$R_{ic} = (Y_0{}^2 - 2aY_0 \sin\theta_c + a^2 \sec^2\phi)^{\frac{1}{2}} \tag{24}$$

where θ_c and ϕ_c satisfy the following equations for the diffracted waves:

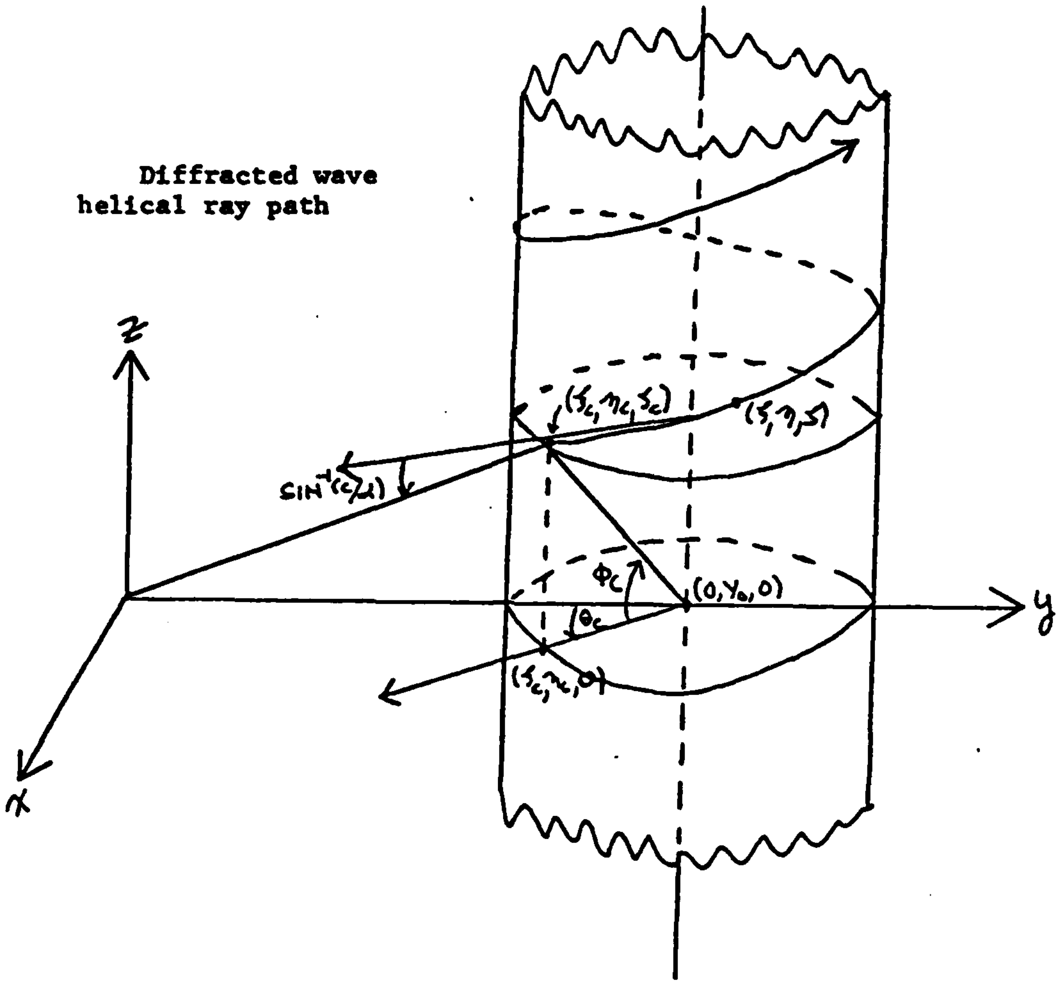

Figure 19: Diffracted wave helical ray path on the cylinder.

For KP_dK:

$$\pi - \cos^{-1}((Y_0^2 - aY_0\cos\theta_c + a^2\sec^2\phi_c)/aR_{ic})) = \sin^{-1}(c/\alpha) \quad (36)$$

For KS_dK:

$$\pi - \cos^{-1}((Y_0^2 - aY_0\cos\theta_c + a^2\sec^2\phi_c)/aR_{ic})) = \sin^{-1}(c/\beta) \quad (37)$$

For KR_dK:

$$\pi - \cos^{-1}((Y_0^2 - aY_0\cos\theta_c + a^2\sec^2\phi_c)/aR_{ic})) = \sin^{-1}(c/v_r) \quad (38)$$

For KK_dK:

$$\cos^{-1}((Y_0^2 - aY_0\cos\theta_c + a^2\sec^2\phi_c)/aR_{ic})) = \pi/2 \quad (39)$$

The parametric equations describing the positions of the secondary source points $Q(\xi,\eta,\zeta)$ on the cylindrical acoustic-elastic interface are given by:

$$\xi = a\sin\theta \tag{40a}$$

$$\eta = Y_0 - a\cos\theta \tag{40b}$$

$$\zeta = a\tan\phi + b_{dk}(\theta - \theta_c). \tag{40c}$$

The expanding radii from the secondary source points for each diffracted wave-type are given by:

$$R(KP_dK) = ct - R_{ic} - sc(\theta - \theta_c)/\alpha \tag{41a}$$

$$R(KS_dK) = ct - R_{ic} - sc(\theta - \theta_c)/\beta \tag{41b}$$

$$R(KR_dK) = ct - R_{ic} - sc(\theta - \theta_c)/v_r \tag{41c}$$

$$R(KK_dK) = ct - R_{ic} - sc(\theta - \theta_c) \tag{41d}$$

where s equals the arc length of the helix for 1° rotation.

$$s = (a^2 + p^2)^{\frac{1}{2}} \tag{41e}$$

Substituting equations (40) and (41) into equations (3) and (4) we obtain the Substitution of equation (26) for p in equation (41e) yields the arc length for a 1° rotation.

$$s = a(Y_0{}^2\sin^2\theta_c + (0.1746)^2\tan^2\phi_c)^{\frac{1}{2}}/Y_0\sin\theta_c \tag{41f}$$

Substituting equations (40) and (41) into equations (3) and (4) we obtain the following wavefront and ray path parametric equations for the diffracted waves:

For KP_dK :

$$x_0 = \xi + A_1\cos\theta \pm \sin\theta(R^2(KP_dK) - (z_o - \zeta)^2 - A_1{}^2)^{\frac{1}{2}} \tag{42a}$$

$$y_0 = \eta + A_1\sin\theta \mp \cos\theta(R^2(KP_dK) - (z_o - \zeta)^2 - A_1{}^2)^{\frac{1}{2}} \tag{42b}$$

$$z_0 = \zeta + R(KP_dK)(\alpha a R_{ic}{}^{-1} Y_0 \tan\phi \sin\theta + \theta - \theta_c)/\alpha(Y_0$$

$$\sin\theta_c + \theta - \theta_c) \tag{42c}$$

$$A_1 = (c/\alpha)R(KP_dK) - (z_0 - \zeta)\tan\phi/Y_0\sin\theta_c \tag{42d}$$

Similarly to obtain the equations necessary to calculate the wavefronts and ray paths for KS_dK, KR_dK and KK_dK we need only to substitute equations (41), along with the correct velocity in place of α, into equations (42).

To obtain the two dimensional equations for the diffracted waves we set $\phi = 0$ in equations (33-42). Doing so we obtain:

$$\xi = a\sin\theta \tag{43a}$$

$$\eta = Y_0 - a\cos\theta \tag{43b}$$

$$\zeta = 0 \tag{43c}$$

$$r_{ic} = (Y_0{}^2 + a^2 - 2aY_0\cos\theta_c)^{\frac{1}{2}} \tag{43d}$$

$$x_0 = \xi + (rc/\alpha)\cos\theta \pm r\sin\theta(1 - c^2/\alpha^2)^{\frac{1}{2}} \quad (44a)$$

$$y_0 = \eta + (rc/\alpha)\sin\theta \mp r\cos\theta(1 - c^2/\alpha^2)^{\frac{1}{2}} \quad (44b)$$

$$z_0 = 0 \quad (44c)$$

$$r = r(KP_dK) = ct - r_{ic} - (ac/\alpha)(\theta - \theta_c) \quad (44d)$$

By substituting the appropriate velocity in place of α in equations (33) they can be transformed into the equations describing the wavefronts and ray paths for the remaining diffracted waves. The diffracted wavefronts for all four diffracted waves are shown in Figure 20 as computed from the above equations at t = 70 μsec..

Analysis

The events labeled in the data, Figures 7, 8, 9 and 10, were picked by calculating the arrival times of the different wavefronts at the receivers using the simple ray theory discussed in equations 1 through 44 of the previous section. Since the velocities of the acoustic and elastic media were known, this information was also used in the interpretation of the arrivals of the diffracted waves. By placing

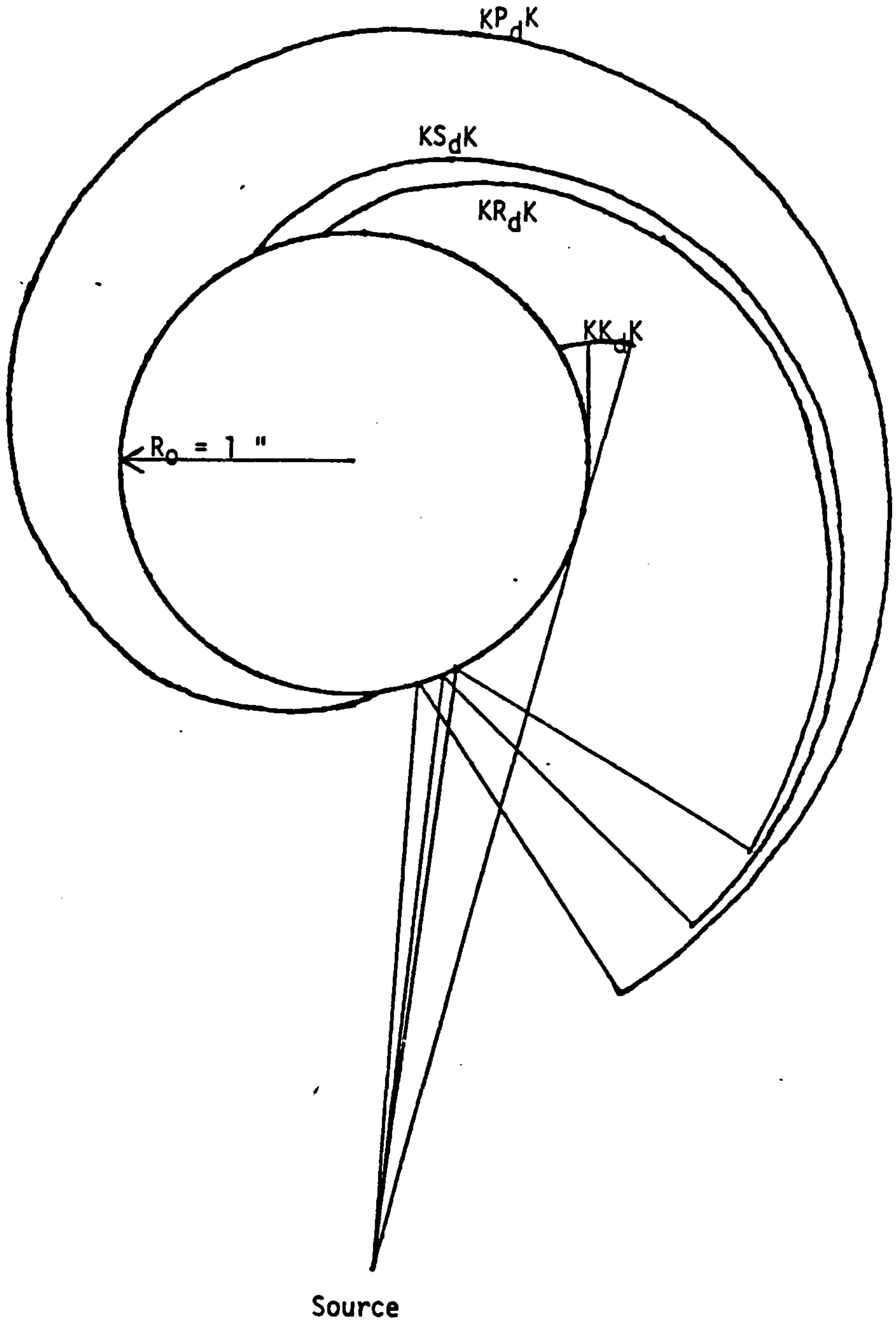

Figure 20: 2D diffracted wavefronts at t = 70 usecs.

AD-A095 919 HENRY KRUMB SCHOOL OF MINES NEW YORK ALDRIDGE LAB OF--ETC F/G 8/11
ELASTIC AND VISCOELASTIC WAVE SCATTERING AND DIFFRACTION.(U)
JAN 81 J T KUO, Y TENG, K CHEN, C E SHEPHERD F49620-77-C-0130

UNCLASSIFIED AFOSR-TR-81-0107 NL

3 OF 3

AD A
095919

the receivers on concentric arcs about the cylinder, the identification of the diffracted waves is simplified because, for a given type of diffracted wave received at two receivers on the same arc, the only part of the ray path that changes is the path on the cylinder. Only this segment of the entire ray path changes because the diffracted wave is always radiated from the cylinder at the same angle. Therefore, the time interval between the arrival of the diffracted wave at two receivers, θ_1 and θ_2, on the same arc can be calculated in the following manner:

$$\Delta T = s(\theta_1 - \theta_2)/V \tag{45}$$

where s is the helical arc on the cylinder and V is the velocity of the diffracted wave on the cylinder. If the arrival times of the diffracted events are plotted as a function of θ, then they will lie on straight lines whose slopes will be proportional to the velocity of the diffracted wave. This phenomenon is most easily seen in Regions I and II as shown in Figures 7 and 8 for both 2D(coplanar) and 3D(non-coplanar) data. For non-symmetric receiver positions these diffracted events split into front and back diffractions propagating in both directions around the cylinder. The time interval between arrival at the same receiver is given by

$$\Delta\delta T = 2s/v, \tag{46}$$

where s is the arc length of the helical path on the cylinder and v is the velocity of the diffraction. Again this phenomenon is best seen in the dats collected in Regions I and II (see Figures 7 and 8).

Interpretation and Discussion

The following events are identified in this Region I:

1.) KPK, the transmitted P wave

2.) KP_dK^b, the back diffracted P wave

3.) KSK, the transmitted S wave

4.) $KS_dK^{f,b}$, the front and back diffracted S waves

5.) $KR_dK^{f,b}$, the front and back diffracted Rayleigh waves

6.) K3PK, the twice internally reflected P wave

7.) $KK_dK^{f,b}$, the front and back diffracted acoustic waves

8.) $KP_dK^{1f,b}$, the first circumnavigated front and back diffracted P waves

9.) K5PK, the four time internally reflected P wave

10.) KPPSK, KPSPK, KSPPK, labeled K2PSK

11.) KPSSK, KSPSK, KSSPK, labeled KPSSK

The data for Region I, the shadow zone, are displayed in Figure 7 For this discussion the coplanar case will referred to as 2D and the non-coplanar case as 3D. Both the 2D and the 3D data exhibit the same phenomena. The KPK event is the first arrival followed closely by the KP_dK event. At the symmetrical receiver position 0° azimuth, the KPK event is clearly identifiable. Since the receivers are placed on a concentric arc about the cylinder the moveout of the diffracted wave is constant(see equation (45)) and the arrivals should appear to lie on a straight line when the arrival time is plotted as a function of azimuth. This is easily observed in both the 2D and the 3D data (see Figure 7). The KP_dK^b(back diffracted P wave)event travels a longer path to arrive at receivers 5° to 30° and , therefore, arrives later as the receiver azimuth increases. The KP_dK^f(front diffracted P wave) event travels an increasingly shorter path to these same receivers. However, due to the magnitude of the KPK event the KP_dK^f event can not be detected. Due to this splitting, the $KP_dK^{f,b}$ events destructively interfere at azimuth 5° for both cases and at 10° for the 2D case. The next strong arrival is the KSK event. This event is very prominent but as the receiver nears the shadow zone boundary, the KSK and the KP_dK^b events begin to interfere. At 25° the KSK event is lost but the diffracted event is identifiable. At 30° both events are identifiable. The front and back traveling diffractions are most observable by tracking $KS_dK^{f,b}$ and $KR_dK^{f,b}$. These events form a V as the receiver azimuth increases. Interference between the KSK and the KS_dK^f events begins to occur when the source configuration is no longer symmetric. It becomes increasingly difficult to detect the correct arrival time of KS_dK^f and at 25° this interference destroys both events creating a data void. K3PK is easily detectable, but as the shadow zone boundary is approached, interference with KR_dK(the back diffracted Rayleigh wave) increases. This interference is so great that it appears that only one event arrives. As the shadow boundary(30° azimuth) is crossed , the KR_dK^f and K3PK, as well as, the KP_dK^b and KSK events cross and become separately identifiable again. The multiply internally reflected mode converted transmitted waves K2PSK are evident in the time interval between K3PK and KK_dK. Again, the diffracted acoustic wave, KK_dK^f, crosses K2PSK at azimuth 20° and it also crosses K3PK and KR_dK^b at 30° azimuth(the shadow zone boundary). Beyond 30° azimuth, KK_dK^f is not detectable until it circum-navigates the cylinder. Diffractions which circum-navigate the cylinder are detectable as evidenced by the arrival of KP_dK^1 following the KK_dK event at 0° azimuth. The later arrivals consist of KP2SK and K5PK. Other K1PmSK, K1PK and KmSK, as well as other circumnavigating diffractions, are extremely difficult to interpret with any confidence so they are not.

The following events are identified in this Region II:

1.) KPK, the transmitted P wave
2.) KP_dK^b, the back diffracted P wave
3.) KSK, the transmitted S wave
4.) $KS_dK^{f,b}$, the front and back diffracted S waves
5.) $KR_dK^{f,b}$, the front and back diffracted Rayleigh waves
6.) K3PK, the twice internally reflected P wave
7.) $KK_dK^{f,b}$, the front and back diffracted acoustic waves
8.) $KP_dK^{1f,b}$, the first circumnavigated front and back diffracted P waves
9.) K5PK, the four time internally reflected P wave
10.) KPPSK, KPSPK, KSPPK, labeled K2PSK
11.) KPSSK, KSPSK, KSSPK, labeled KPSSK

In Region II the first phenomenon noticed is the amplitude decay of KPK and KSK. This is not as noticeable in Region I. Each of the other events which are identified for the shadow zone are also observed and identified in this region. Besides these events, Region II adds KPSK, KSPK and K to this list. The first arrival in Region II is the KPK event. Although these reveivers are in the illuminated zone, diffracted P, S and Rayleigh waves are still received. The KP_dK^f event is not evident since it arrives in the time window of KPK. The KP_dK^b arrival at 35° is superimposed on KSK and remains unseparated from it until azimuth 50°. For receivers between at azimuths 35° and 50°, four different events are superimposed within the time window 98.25 to 103.25 μsecs., making identification of the separate events difficult. These events are KP_dK^b, KSK, KS_dK^f and KR_dK^f. The KS_dK^f event is not visible as a separate event at 35° azimuth but KR_dK^f has an identifiable arrival time but no termination point. Arriving on the tail of KR_dK^f is the mode converted events KPSK. These mode converted arrivals are unidentified in the shadow zone. Another event which is non-existent in the shadow zone , but does exist in the near shadow zone and in the remainder of the illuminated zone, is the direct acoustic wave, K. K arrives at receiver 35° at 112 μsecs. coupled with KR_dK^b. At 40°, the K event arrives coupled with KS_dK^b and K3PK. Since the radiation pattern of the source transducer is narrow(Figure 3), the K event is low in amplitude and shows no evidence of its existence at 45° and 50°. At 55°, the K event arrives coupled with the mode converted events KPSK. Throughout the near shadow region the diffracted events KS_dK^b and KR_dK^b are identified. Mode converted events K2PSK and KP2SK are detected and identified in this region. The KP_dK^{1f} arrival in this region displays a moveout to earlier times as the receiver azimuth increases. It should be noted that back diffracted acoustic waves are present in the illuminated zone, as well as, the diffracted waves $KP_dK^{f,b}$, $KS_dK^{f,b}K$ and $KR_dK^{f,b}$.

The following events are identified in Region III:

1.) K, the direct acoustic wave

2.) KPK, the transmitted P wave

3.) $KP_dK^{f,b}$, the front and back diffracted P waves

4.) K2PK, the first internally reflected P wave

5.) KSK, the transmitted S wave

6.) $KS_dK^{f,b}$, the front and back diffracted S waves

7.) $KR_dK^{f,b}$, the front and back diffracted Rayleigh waves

8.) KK_r, the reflected acoustic wave

9.) K3PK, the second internally reflected P wave

10.) KPSK, KSPK, labeled KPSK

12.) K2SK, the first internally reflected S wave

13.) KP_dK^{1f}, the first circumnavigated diffracted P wave

14.) KPSSK, KSPSK, KSSPK, labeled KPSSK

16.) K3SK, the second internally reflected S wave

17.) KPSSK, KSPSK, KSSPK, labeled KPSSK

18.) KPSSK, the mode converted P to SS wave

19.) KPSSSK, KSPSSK, KSSPSK, KSSSP, labeled KP3SK

In this region certain events are received and identified which are not present in the shadow or the near shadow regions. Since receiver 90° and 105° are within the reflection region, reflected acoustic waves, KK_r, are received and since receiver 75° is outside of this region no KK_r event exists(see Figure 3). Transmitted waves with an even number of P ray paths and S ray paths without any mode conversions are observed at these receivers. K2PK and K2SK are unidentified at receivers in the shadow and near shadow zones but they are observed for receivers at 75°, 90° and 105° azimuth. A splitting effect for K2PK and K2SK is evident in this region caused by internal reflections traveling in both directions around the cylinder. On examination of the transmitted ray diagrams in Figures 16 and 17, this effect is seen if it is remembered that these diagrams plot only one half of the ray path and wavefront. Dual arrivals of K2PK, K2SK and K3PK are identified in Figure 9. Most of the observed events in this region are combinations of events. The first arrival is a combination of K, KPK, KP_dK^f and K2PK at receiver 75°. At 90°, the K event arrives much earlier than the combination KPK, KP_dK^f and K2PK with such a low amplitude that it is unrecorded. At all three receivers, KSK, KS_dK^f and KR_dK^f arrive as overlapping wavelets. From trace to trace the form of the signal changes because each of these events has a different moveout such that they cross each other. At 105°, both diffracted events, KS_dK^f and KR_dK^f, arrive before KSK due to their larger moveouts as the receiver azimuth increases. Between 116 and 120.5 μsecs., the K2PK, the K3PK and the KP_dK^b events arrive very close together. At receiver azimuth 90°, the KP_dK^b event is undetected but is reappears at 105°. K3PK arrives at receiver 90° on the tail of the reflected acoustic, KK_r. K2PK is present on all three traces. Within the time window 123 to 128.5 μsecs. at receiver 75°, the KPSK events arrive simultaneously followed by a second K3PK event due to the splitting of transmitted waves, previously mentioned. At 90°, KPSK and K3PK arrive closer together and at 105° they combine to form a single low amplitude event. K2SK arrives following this group at all three receivers followed by the mode converted events K2PSK. A second K2SK event is identified at receiver 90° at 134.5 μsecs. coupled with the first circumnavigated front diffracted P wave, KP_dK^{1f}. The diffracted S wave, KS_dK^b, appears at all three receivers and it displays its characteristic moveout arriving later as the receiver azimuth increases. The back diffracted Rayleigh wave, KR_dK^b, is unidentifiable at 75°, but it is identified at 90° and 105°. It also displays moveout. Finally, KP2[illegible] events are observed arriving at receiver 75° and KP3SK are observed at 90° arriving simultaneously. In this region, the central part of the illuminated zone, more transmitted waves are observed than in the shadow zone creating a more complicated signal. The diffracted waves are still observed in this region.

Figures 10a and 10b displays the data for Region IV for which the source has been moved to a distance of $6R_0$ from the cylinder and the receivers are placed on a circular arc of the same radius about the cylinder at azimuths 120°, 135°, 150° and 160° as shown in Figure 6. This configuration covers the deep illuminated zone where backscattering predominates. Reflected acoustic waves, KK_rK are the first and most predominant of the received events in this region. The waveform is clipped because its amplitude is much greater than the amplitude of the remainder of the scatterred and diffracted signal. Very little diffracted energy is observed in this region. The front diffracted waves, KP_dK^f, KS_dK^f and KR_dK^f, arrive within the time window of the KK_r event and are therefore undetectable due to the large amplitude of the reflected acoustic wave, KK_r. The back diffracted waves are undetected because they are attenuated rapidly and they arrive in the same time windows as the larger amplitude transmitted waves.

In Figures 10, the following transmitted waves are identified in Region IV:

1.) K2PK
2.) KPSK and KSPK, labeled KPSK
3.) K3PK
4.) KPSPK, KPPSK and KSPPK, labeled K2PSK
5.) KSSK
6.) KPPPSK, KPPSPK, KPSPPK and KSPPPK, labeled K3PSK
7.) K4PK
8.) K3SK
9.) KSPSPK, KPSSPK,KSSPPK,KPPSSK and KSPPSK, labeled K2P2SK
10.) KSSPK, KSPSK and KPSSK, labeled KP2SK

Just as the diffracted waves split into two arrivals propagating in both directions around the cylinder, a similar splitting occurs for the transmitted waves. The K3PK event shows a dual arrival at 160° overlapping each other at 190.5 μsecs.. The mode converted waves K3PK display this phenomenon on all traces with arrivals at 210.8 and 217.6 μsecs. at receiver 120°. These dual arrivals become closer together as the receiver azimuth increases as seen in Figures 10. This backscattered region contains mostly transmitted waves .

The amplitude spectra of the data have many peaks and troughs unlike the source wavelet(see Figure 2b). Modulation of the amplitude spectrum is caused by the multitude of arriving events within the time window analyzed. The peaks are related to the relative arrival times between two events The reciprocals of the peak frequencies are the relative arrival time difference. Having already interpreted the data, comparison of the spectral peaks to the relative arrivals of the data is done. Tables I and II show the correspondence between the spectral peaks and the relative relative arrival times between events for the 2d coplanar case at receivers 0° and 5° in the shadow zone. Figure 29 displays the spectra for receivers 0° and 5° for the data presented in Tables I and II.

CONCLUSIONS

A three dimensional model experiment has been performed to study the acoustic-elastic wave scattering and diffraction of a transient acoustic wave emitted from a point source by an infinite elastic cylinder embedded in a fluid medium. This is the first three dimensional model experiment using multiple receiver positions throughout all of the scattering regions. The data verify the existence of KPK, KSK, K2PK, K2SK, KPSK, KP2SK, K2PSK, K3PK, K3SK, K3PSK, KP3SK, K5PK, K, KK_r, $KP_d{}^{f,b}K$, $KP_d{}^{1f}K$, $KS_d{}^{f,b}K$, $KR_d{}^{f,b}K$, $KK_d{}^{f,b}K$ and those transmitted converted waves which have the same number of P and S wave ray segments interior to the cylinder as those stated here. The verification of the existence of $KP_d{}^{f,b}K$, $KS_d{}^{f,b}K$, $KR_d{}^{f,b}K$, $KK_d{}^{f,b}K$, $KP_d{}^{1f}K$ in three dimensions and of $KP_d{}^{f,b}K$ and $KS_d{}^{f,b}K$ in two dimensions is accomplished for the first time. It is also for the first time that all of the diffractions and all of the transmitted waves have been shown together on the same data trace so that their interaction could be discerned. By establishing the existence of the various transmitted and diffracted waves for a non-coplanar(three dimensional) source-receiver configuration, the verification of the helical path traced on the cylindrical surface by the various as predicted by theory is accomplished. It is also shown that the diffractions due propagate into the shadow zones due to the fact that they propagate in all directions around the the cylinder. Through spectral analysis the spectral maxima are shown to correspond to the relative arrival time separartion between various events. The non-abrupt nature of the acoustical shadow boundary is shown by use of the complex cepstrum. The maximum phase component of the cepstrum becomes greatly changes in the vicinity of the geometrical shadow boundary. If the geometrical shadow zone is being entered then the negative cepstrum becomes more complicated and the terms increase in amplitude. However, upon leaving the geometrical shadow the negative cepstrum decreases in complexity and the amplitude of the terms decrease also. Envelope detection is employed to determine the arrival times and the duration and the duration of the arriving events. From the envelope detection method the contamination of arrivals due to overlapping is readily seen. Homomorphic filtering is used to attempt to remove the wavelet effects and decouple the overlapping events, but it does not perform satisfactorily since the contamination is by more than one or even two events in most instances.

REFERENCES

Barnard, G. R. and McKinney, Scattering of Acoustic Energy by Solid and Air-filled Cylinders in Water, J. Acous. Soc. Am., v. 33, pp.226-238, 1961.

Bertrand, J. C. and Young, J. W., Multiple SCattering Between a Cylinder and a Plane, J. Acous. Soc. Am., v. 60, n. 6, dec., 1976.

Bifulco, F. and Sachse, W., Ultrasonic Pulse Spectroscopy of a Solid Inclusion in an Elastic Solid, Ultrasonics, May, 1975.

Brill, D. W., Acoustic Waves Transmitted through Liquid and Elastic Cylinders, Ph. D. thesis, Catholic Univ., 1970.

Brill, D. W. and Uberall, H., Acoustic Waves Transmitted through Solid Elastic Cylinders, J. Acous. Soc. Am., v. 50, n. 3, pp. 921-939, 1971.

Buhl, P., Stoffa, P. L. and Bryan, G. M., The Application of Homomorphic Deconvolution to Shallow-Water Marine Seismology - Part II: Real Data, Geophysics, v. 39, n. 4, pp. 417-426, 1974.

Bunney, R. E., Goodman, R. R. and Marshall, S. W., Rayleigh and Lamb Waves on Cylinders, J. Acous. Soc. Am., v. 46, n. 5, pp. 1223-1233, 1969.

Buttkus, B., Homomorphic Filtering - Theory and Practice, Geophysical Prospecting, v. 23, pp. 712-748, 1975.

Chen, P. and Pao, Y. H., The Diffraction of Sound Pulses by a Circular Cylinder, J. MAth. Phys., v. 18, n. 12, Dec., 1977.

Clayton, R. W. and Wiggins, R. W., Source Shape Estimation and Deconvolution of Teleseismic Bodywaves, Geophy. J. R. A. Soc., v. 47, pp. 151-177, 1976.

Dickey, J. W., Acoustic High Frequency Scattering by Elastic Cylinders, Ph. D. thesis, Catholic Univ., 1977.

Doolittle, R. D., Frisk, G. V. and Uberall, H., Whispering Gallery Modes on Elastic Cylinders, J. Acous. Soc. Am., v. 43, n. 1, pp. 1-14, 1968.

Faran, J. J., Sound Scattering by Solid Cylinders and Spheres, J. Acous. Soc. Am., v. 23, pp. 405-418, 1951.

Friedlander, F. G., Diffraction of Pulses by a Circular Cylinder, Comm. Pure Appl. Math., v. VII, pp. 705-732, 1954.

Frisk, G. V., Creeping Waves and Lateral Waves in Acoustic Scattering by Large i Elastic Cylinders, Ph. D. thesis, Catholic Univ., 1975.

Frisk, G. V., Dickey, J. W. and Uberall, H., Surface Wave Modes on Elastic Cylinders, J. Acous. Soc. Am., v. 58, n. 5, pp. 996-1000, 1975.

Frisk, G. V., and Uberall, H., Creeping Waves and Lateral Waves in Acoustic Scattering by Large Elastic Cylinders, J. Acous. Soc. Am., v. 59, n. 1, pp. 46-54, 1976.

Gilbert, F., Scattering of Impulsive Elastic Waves by a Smooth Convex Cylin der,J. Acous. Soc. Am., v. 32, n. 7, pp. 841-857, 1960.

Gilbert, F. and Knopoff, L., Scattering of Impulsive Elastic Waves by a Rigid Cylinder, J. Acous. Soc. Am., v. 31, n. 9, pp. 1169-1175, 1959.

Harbold, M. L., and Steinberg, B. H., Direct Experimental Verification of Creeping Waves, J. Acous. Soc. Am., v. 45, n. 3, pp. 592-603, 1969.

Hickling, R., Analysis of Echoes from a Hollow Metallic Sphere in Water, J. Acous. Soc. Am., v. 36, n. 6, pp. 1124-1137, 1964.

Hwang, L. F. and Kuo. J. T., Three Dimensional Elastic Wave Scattering and Diffraction of and Infinitely Long Rigid Cylinder Embedded in an Infinite Elastic Medium With a Point Source Located in the Medium, unpublished.

Keller, J. B., A Geometrical Theory of Diffraction, in Calculus of Variations and its Applications, Proceedings of Symposium in Applied Math.,

v. 8, ed. L. M. Graves, McGraw-Hill, N. Y., 1958.

Keller, J. B., Geometrical Theory of Diffraction, J. Opt. Soc. Am., v. 52 , n. 2, pp. 116-130, Feb., 1962.

Keller, J. B. and Karal, F. C., Geometrical Theory of Elastic Surface Wave Excitation and Propagation, J. Acous. Soc. Am., v. 36, n. 1, pp. 32-40, Jan., 1964.

Kemerait, R. C. and Childers, D. G., Signal Detection and Extraction by Cepstrum Techniques, IEEE Trans. on Information Theory, v. IT-18, n. 6, 1972.

Ko, W. L., Scattering of Stress Waves by a Circular Elastic Cylinder Embedded in an Elastic Medium, J. Appl. Mech., pp. 345-355, June, 1970.

Kouyoumjian, R. G., The Geometrical Theory of Diffraction and its Applications, in Topics in Applied Physics, v. 3, 1975, Numerical and Asymptotic Techniques in Electromagnetics, ed. R. Mitra, Springer-Verlag , N. Y..

Ludwig, D., Geometrical Theory for Surface Waves, SIAM Review, v. 17, n. 1 , Jan., 1975.

McNicholas, J. V., Uberall, H. and Choate, K., Pulse Shapes of Creeping Waves around Soft Cylinders, J. Acous. Soc. Am., v. 44, n. 3, pp. 752-764 , 1968.

Mow, C. C. and Workman, J. W., Dynamic Stresses around a Fluid-filled Cavity , J. Appl. Mech., pp. 793-799, Dec., 1966.

Neubauer, W. G., Experimental Observation of Three Types of Pulsed Circumferential Waves on Solid Aluminum Cylinders, J. Acous. Soc. Am., v. 44 , n. 4, pp. 1150-1152, 1968.

Neubauer, W. G., Pulsed Circumferential Waves on Aluminum Cylinders in Water , J. Acous. Soc. Am., v. 45, n. 5, pp. 1134-1144, 1969.

Neubauer, W. G., Observation of Acoustic Radiation from Plane and Curved Boundaries, in Physical Acoustics X, ed. W. P. Mason and R. N. Thurston, Academic Press, 1973.

Oppenheim, A. V., Schafer, R. W. and Stockhum, T. C., jr., Nonlinear Filter ing of Multiplied and Convolved Signals, Proc. IEEE, v. 56, n. 8, 1968.

Pao, Y. H. and Sachse, W., Interpretation of Time Records and Power Spectra of Scattered Ultrasonic Pulses in Solids, J. Acous. Soc. Am., v. 56, n. 5, pp. 1478-1486, 1974.

Rudgers, A. J. and Uberall, H., Pulses Specularly Reflected by a Soft Cylinder, J. Acous. Soc. Am., v. 48, n. 1, pp. 371-381, 1970.

Sachse, W., Ultrasonic Spectroscopy of a Fluid-filled Cavity in an Elastic Solid, J. Acous. Soc. Am., v. 56, n. 3, pp. 891-896, 1974.

Sachse, W., Density Determination of a Fluid Inclusion in an Elastic Solid from Ultrasonic Spectroscopy Measurements, 1974, Ultrasonics Symposium Proceedings IEEE, cat n. 74.

Sachse, W. and Chian, C., Determination of the Size and Mechanical Properties of a Cylindrical Fluid Inclusion in an Elastic Solid, Presented at the National Fall Conference of the American Society for Non-destructive Testing , Oct. 21-24, 1974, Detroit, Mich..

Schiel, K., Possibilities of Investigation of Subsurface Inhomogenie-ties , unpublished.

Shepherd, c. E., Experimental Model Studies of Three Dimensional Acoustic and Elastic Scattering and Diffraction, Presented at the 47th Annual Meeting of the Soceity of Exploration Geophysicists, Calgary, Alberta, Canada, October, 1977

Stoffa, P. L., Buhl, P. and Bryan, G. M., The Application of Homomorphic Deconvolution to Shallow-Water Marine Seismology - Part I: Models, Geophysics , v. 39, n. 4, pp 401-416, 1974.

Teng, Y. C., Kuo, J. T. and Gong, C., Three Dimensional Acoustic Scattering and Diffraction by an Open-ended Vertical Soft Cylinder in a Half-space, J. Acous. Soc. Am., v. 57, n. 4, pp. 782-790, 1975.

Uberall, H., Surface Waves in Acoustics, in Physical Acoustics X, ed. W. P. Mason and R. N. Thurston, Academic Press, 1973.

Uberall, H., Doolittle, R. D. and McNicholas, J. V., Use of Sound Pulses for a Study of Circumferential Waves, J. Acous. Soc. Am., v. 39, n. 3, pp. 567- 578, 1966.

Uberall, H., Dragonette, L. R. and Flax, L., Relation Between Creeping Waves and Normal Modes of Vibration of a Curved Body, J. Acous. Soc. Am., v. 61, n. 3, pp. 711-715. 1977.

Uberall, H. and Hwang, H., Acoustical Response of Submerged Elastic Structures obtained through Integral Transforms, in Physical Acoustics XII, ed. W. P. Mason and R. N. Thurston, Academic Press, 1976.

Ulrych, T. J., Application of Homomorphic Deconvolution to Seismology, Geophysics, v. 36, n. 4, pp. 650-660, 1971.

Viktorov, I. A., Rayleigh and Lamb Waves, Plenum Press, N. Y., 1967.